SAPIENZA
UNIVERSITÀ DI ROMA

Coherent light sources and optical techniques for Thomson scattering and Laser-Plasma experiments

Scuola di dottorato Vito Volterra

Dottorato di Ricerca in Fisica – XXIX Ciclo

Candidate

Fabrizio Giuseppe Bisesto
ID number 1243715

Thesis Advisors

Prof. Paolo Mataloni
Dr. Andrea Ghigo

A thesis submitted in partial fulfillment of the requirements
for the degree of Doctor of Philosophy in Physics

December 2016

Thesis defended on 16 February 2017
in front of a Board of Examiners composed by:

Prof. Mauro Carfora (chairman)

Prof. Sergio Caracciolo

Dr. Antonello Scardicchio

Coherent light sources and optical techniques for Thomson scattering and Laser-Plasma experiments

Ph.D. thesis. Sapienza – University of Rome

This thesis has been typeset by LaTeX and the Sapthesis class.

Author's email: fabrizio.giuseppe.bisesto@lnf.infn.it

Contents

List of Figures

List of Tables

Introduction

Recent progress in accelerators and lasers technology opens new perspectives in terms of particle-photon colliders luminosity: low cross section processes can be therefore utilized to create specific radiation sources. Indeed, exploiting the inverse Compton scattering or Thomson back-scattering process, the interaction between relativistic electron beams ($\gamma >> 1$) and near-infrared laser pulses ($\lambda \approx 1\mu m$) yields electromagnetic waves in the X-ray and γ-ray range. The energy, the flux and the spectrum of such kind of generated radiation are suitable for many purposes, e.g. dynamical studies and imaging of solid, molecular and biological systems [1, 2, 3, 4].

Nevertheless, the big development in the high power laser field, begun in the '80s thanks to the chirped pulse amplification (CPA) scheme [66], has provided systems to be employed in the study of the laser wakefield acceleration (LWFA). As stated by Tajima and Dawson in 1979 [85], an intense laser pulse, propagating through a plasma, can stimulate plasma waves able to accelerate electrons with accelerating gradients greater than $100GV/m$, i.e. some orders of magnitude more than the conventional RF-based LINAC. Moreover, with TW-class laser systems and intensity more than $10^{18}W/cm^2$, the relativistic regime occurs and electrons can be self-injected into the plasma accelerating structure. This opens the possibility to build much more compact particle accelerators, even though the beam quality, in terms of emittance and energy spread, is not yet comparable to the standard linear accelerator.

In this work, the activity related to Thomson back-scattering and laser-plasma interaction pursued at SPARC_LAB Facility in Frascati (Italy) will be presented. SPARC_LAB (Sources for Plasma Accelerators and Radiation Compton with Lasers and Beams) is a multi-disciplinary facility aiming to test new radiation source (THz, XUV, X-Ray) exploiting different phenomena such Free Electron Laser (FEL), Coherent Transition Radiation (CTR) and Thomson back-scattering, thank to the high brightness electron beam that it can provide. The peculiarity of SPARC_LAB is the presence of $300TW$ FLAME laser together with the high brightness LINAC. This kind of laser represents a powerful tool to study Thomson back-scattering, when combining it with the linear accelerator, as well as the interaction with the matter, mainly to perform experiments related to LWFA, both in self-injection and external-injection regime. Furthermore, a development of a new diagnostics tool able to measure electron beam emittance in a single shot way will be presented. This novel technique seems to be very useful for beam from plasma accelerators, since they suffer shot-by-shot instabilities. Therefore, a statistical measurement would me meaningless while a single shot diagnostics can provide a more useful description of electron beam parameters. Simulations and some preliminary results will be

provided. In addiction, also a research activity on interaction with solid target has been conducted in order to study the possibility to optimize the ion acceleration without increasing the laser energy but opportunely shaping the target itself.

This thesis consists in two parts, for a total of nine chapters.

Part I presents X-Ray source based on Thomson back-scattering. After a brief discussion on the theoretical aspects of the inverse Compton scattering (Chapter 1), the attention is focused on the experimental activity performed at SPARC_LAB in Chapter 2. Here, an overview on this facility, included the sub-PW FLAME laser, and the experimental results of the two commissioning runs will be given. Moreover, in Chapter 3, the STAR Project, aiming to build a new X-Ray factory for applied research, thanks to the experience of SPARC_LAB team, together with other partners (Univ. of Calabria, CNISM and Sincrotrone Trieste), will be presented. An overview of the whole project, with particular regard to the photocathode and interaction laser systems as well as to the optimization of the interaction point geometry.

Part II concerns the particle acceleration in high intensity laser-matter interactions. Chapter 4 introduces the idea of Plasma Acceleration, starting from the concept of plasma and electron plasma oscillations. The use of laser technology in the LWFA scheme is extensively discussed in Chapter 5, and its realization at FLAME facility is illustrated in Chapter 6, paying attention to the optimization of the experimental parameters, the diagnostics used for plasma density and spatial and spectral electron properties measurements. In Chapter 7 the EXIN experiment on external-injection at SPARC_LAB will be presented. In particular, it will be explained the possibility to employee dielectric structures, similar to optical fibers, working as laser waveguide in order to keep it focused over several Rayleigh lengths. Since in this way it can be possible to overcome the problem of laser beam natural diffraction, a study on its applicability to the FLAME laser is presented. In Chapter 8 is shown a novel transverse diagnostics for electron beams working in single shot mode, very useful and promising for plasma accelerated beams. Furthermore, the interaction of an intense laser with a solid target is treated in Chapter 9, showing the results on the measurements, performed at FLAME facility, on the electric field responsible of ion and proton acceleration.

At last the conclusions for both Parts will be discussed.

Part I

Thomson back-scattering X-Ray source

Introduction

Thomson Scattering (TS) of light from relativistic electrons is a well-known and established source of X-ray and γ-ray radiation. It was in the 1960s, after the discovery of the laser, when the first TS x-ray sources were proposed [5, 6, 7] and demonstrated in experiments [8]. Since then, many important results were obtained describing TS sources [9, 10, 11, 12, 13, 14, 15, 16, 17, 18, 19, 20, 21, 22, 23], including the first demonstration of femtosecond X-ray pulses at the Accelerator Test Facility of Lawrence Berkeley National Laboratory (LBNL) [13, 14]. Intense X-ray and γ-ray sources can be used in many areas of science, industry and medicine. Photons with energies above approximately $1MeV$ serve as a probe for nuclear physics [20].

The TS is the electromagnetic process in which each electron absorbs one (linear Thomson scattering) or more (nonlinear Thomson scattering) photons from a laser pulse, emitting one photon. If the electrons are ultra-relativistic the scattered radiation is frequency upshifted and it is emitted forward with respect to the particles motion, with a small aperture cone, proportional to the inverse of the Lorentz relativistic factor. The laser pulse acts in a similar way as the static magnetic wiggler in synchrotron light sources or free electron lasers [25, 26, 27, 28, 29].

Tunable, near monochromatic, high brightness x-rays would he an important tool in research and medical diagnostics. Synchrotron light sources have produced useful x-rays for a large user community. One advantage to this approach is that, because the wavelength of the laser is many orders of magnitude smaller than that of static undulators, an electron beam of much lower energy can be used to generate X-rays of a particular energy. For example, radiation of $0.04nm$ wavelength ($30keV$) X-rays can be generated by a laser with $1\mu m$ wavelength and electron beam energy of $40MeV$.

Thomson scattering sources typically require much higher electron energies than Bremsstrahlung sources to achieve a certain photon energy, increasing the size of the whole system. With the rapid development of accelerator and laser technology in the recent decades it has now become possible to build dedicated TS machines. Generation of MeV-level γ-rays with storage rings or linacs however leads to large accelerator size (approximately 20 to 50 meters) due to limitations in the accelerating gradient [30]. Additionally, the low conversion factor of scattering laser photons into X-ray or γ-ray photons due to the very small cross-section of the process ($\sim 0.7b$) requires large scattering lasers. These challenges limit current TS applications, especially those requiring transportability. Recent advances in laser plasma accelerators (LPA) [31], where stable GeV-level electron beams have been produced in just $3cm$ of acceleration distance [32] allows one to consider compact Thomson sources.

This first Part will introduce the physics of Thomson back-scattering, starting from single particle 4-momentum conservation. From here it is possible to derive the frequency upshifting of the scattered photons. Furthermore, analyzing the interaction between two beams as electrons and photons distributions, the flux and the resulting radiation spectrum can be found. After this theoretical introduction, the X-ray source at SPARC_LAB based on Thomson back-scattering will be presented, with a short overview of all the other activities as well. In particular, the experimental results of the two commissioning runs will be provided. On the basis of the experience of SPARC_LAB, a new project started with the collaboration of other partners (Univ. of Calabria, CNISM, INFN and Sincrotrone Trieste), aiming to build a new Facility for Thomson back-scattering X-ray source. The STAR project (Southern european Thomson source for Applied Research) will be discussed in the last Chapter, with particular attention to the the laser systems and to the optical systems needed to properly shape the transverse spatial profile of the photocathode laser and to achieve a diffraction limited focal spot in the collision point with the interaction laser.

Chapter 1

Basics of Thomson scattering

Thomson scattering, which includes also undulator radiation, is a well studied area of physics [9, 10, 18, 33, 34, 35]. Maximum photon energy is obtained in the case when the laser photon and electron collide head-on and the photon is scattered exactly backwards, i.e. at 180°). In such a situation, assuming that the laser pulse is weak, photon energy is given by the (double) relativistic Doppler shift formula $\hbar\omega = 4\gamma_e^2\omega_L$, where ω is the generated photon frequency, ω_L is the laser frequency and γ_e is the electron relativistic Lorenz factor.

Laser photons scattered under the angle $\theta << 1/\gamma_e$ have the frequency (assuming linearly polarized laser pulse)

$$\omega = \frac{4\gamma_e^2}{1 + \gamma_e^2\theta^2 + a_0^2/2}\omega_L, \tag{1.1}$$

where $a_0 = eA_L/mc^2$ is the normalized vector potential or laser pulse strength parameter (similar to the undulator strength parameter in the free-electron lasers). Here A_L is the laser pulse vector potential amplitude in CGS units.

The source opening angle is roughly $1/\gamma_e$, with a bow-like energy-angular spectrum which is due to the θ term in Eq. 1.1. This leads to a broad integrated spectrum requiring collimation depending on the desired spectral width. In detail, one can see that the frequency of the generated photon depends on four parameters: 1) the angle of propagation of the generated photon θ; 2) the electron energy γ_e; 3) laser pulse amplitude a_0; and 4) laser frequency ω_L. Indeed, realistic electron beams have a non-zero angular divergence and a finite energy spread: electrons propagating under different angles will generate photon spectra peaked in the direction of their respective propagation; electrons in the beam having different energies will generate different photon energies in accordance with the γ_e contribution in formula 1.1. These two electron beam properties lead to integrated spectrum broadening.

On the laser side, the a_0 term in equation 1.1 leads to additional hard photon beam broadening in the case when laser pulse has a non-constant intensity envelope. Indeed, different frequencies will be generated at different times throughout the pulse (assuming no frequency chirp in the laser pulse). In experiments, depending on the desired bandwidth, one needs to keep a_0 as high as possible for maximizing the photon yield, but low enough to meet the bandwidth requirement. The requirements on the photon source hence put conditions on the laser and electron beams that can be used for generation.

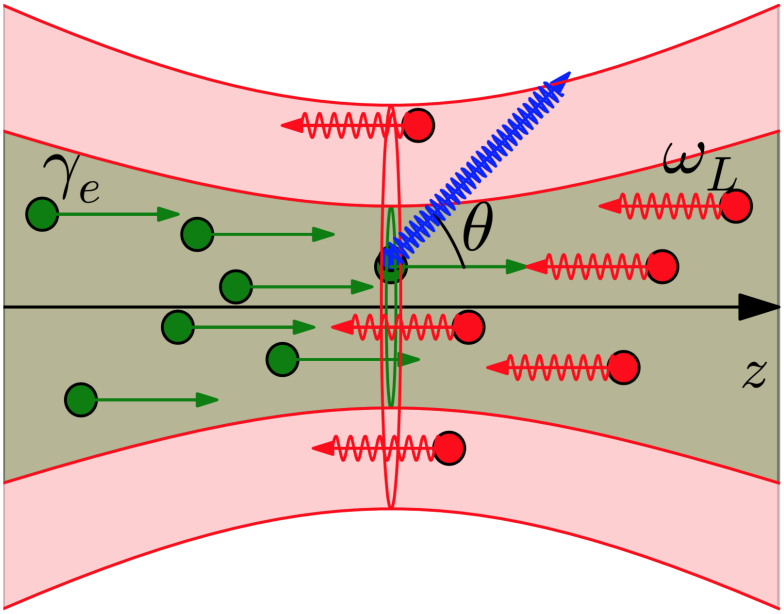

Figure 1.1. Schematic of Thomson back-scattering process [24].

1.1 Relativistic kinematics of the interaction

Let us consider the scattering between an electron and a photon both moving in the laboratory frame (LAB). Without loss of generality, we can consider the incoming electron momentum $\underline{p}_i$ along the z direction as in Fig. 1.3. The incoming photon momentum $\underline{k}_i$ draws the angle α with the electron direction. After the interaction, occurring at the origin of the axis, the photon is scattered with momentum $\underline{k}_f$ and angle θ, while the electron has momentum $\underline{p}_f$.

The incoming and emitted particles are the same, therefore this process is an elastic scattering. In detail, the total 4-momentum conservation reads

$$P_i + K_i = P_f + K_f \tag{1.2}$$

where $P_{i,f} = (E_{i,f}/c, \underline{p}_{i,f}) = (\gamma_{i,f} mc, \gamma_{i,f} \underline{\beta}_{i,f} mc)$, $K_i = (h\nu_L/c, \hbar \underline{k}_i) = (h\nu_L/c, h\nu_i/c \times \underline{e}_i)$ and $K_f = (h\nu/c, \hbar \underline{k}_f) = (h\nu/c, h\nu_f/c \times \underline{n})$.

By squaring both sides of Eq. 1.2, after some manipulations we obtain the frequency of the emitted photon:

$$\nu = \nu_L \frac{1 - \underline{e}_i \times \underline{\beta}_i}{1 - \underline{n} \times \underline{\beta}_i + \frac{h\nu_L}{\gamma_i mc^2}(1 - \underline{e_i} \times \underline{n})} \tag{1.3}$$

This formula describes the frequency-angle correlation, which is a typical feature of this kind of sources, and that permits to rule the bandwidth: the highest frequency of the emitted radiation is at $\theta = 0$ and decreases as in Fig. 1.2. If the electron and

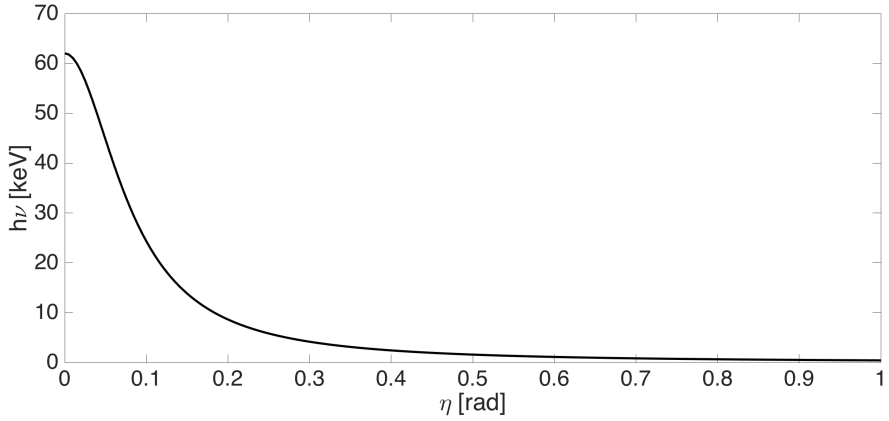

Figure 1.2. Photon energy $h\nu$ in keV units as a function of the angle η in rad for the scattering of an electron with $50MeV$ energy and a laser of $800nm$ wavelength.

the photon are both moving along z in opposite direction, Eq. 1.3 becomes

$$\nu = \nu_L \frac{1 + \beta_i}{1 - \beta_i + \frac{h\nu_L}{\gamma_i mc^2}(1 - cos\eta)} \tag{1.4}$$

which is independent from the azimuthal angle. This means that at a given angle from the axis of propagation of the incoming electron, the energy is the same for every ϕ angle, i.e. the energy decreases in circles around z.

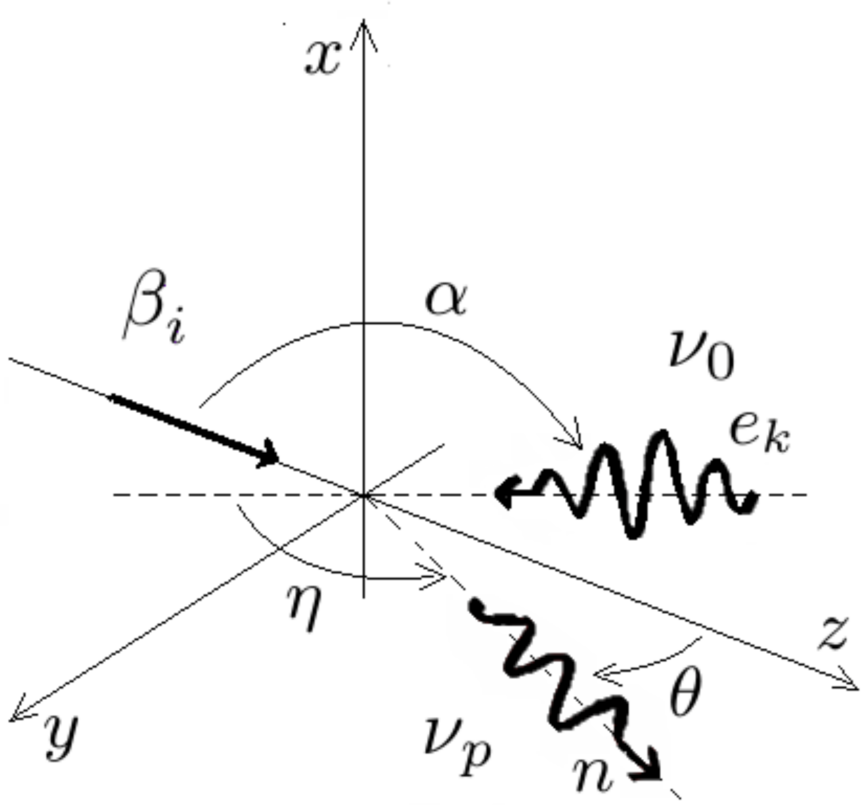

Figure 1.3. Geometry of the electron-photon scattering in the laboratory frame. The incoming electron moves along z while the incoming photon along e_i. α is the angle between their directions. The emitted photon has direction n which draws an angle θ with the z axis and η with e_i .[40]

Let's express Eq. 1.3 in terms of wavelength:

$$\lambda = \lambda_L \frac{1 - \underline{n} \cdot \underline{\beta}_i}{1 - \underline{e}_i \cdot \underline{\beta}_i} + \frac{h}{\gamma_i mc} \frac{1 - \underline{e}_i \cdot \underline{n}}{1 - \underline{e}_i \cdot \underline{\beta}_i}. \tag{1.5}$$

The first term on the right side of Eq. 1.5 represents the classical Thomson effect, while the second part describes the shift due to the electron recoil after the scattering. We can also write it in terms of the angles (see Fig. 1.3) as

$$\lambda = \lambda_L \frac{1 - \beta_i \cos\theta}{1 - \beta_i \cos\alpha} + \frac{h}{\gamma_i mc} \frac{1 - \cos\eta}{1 - \beta_i \cos\alpha}.$$

The wavelength shift λ of the emitted photon is minimum (maximum energy gain) when the incoming electron and photon are perfectly counter-propagating, i.e. $\alpha = \pi$.

1.2 Interaction cross section

Once a certain reaction is observed or predicted by the theory, the major concern is to establish the probability of it to happen given the initial particles energies

and momenta (total cross section) and more into details, the probability that the particles are emitted at specific angles (differential cross section). By integrating over the solid angle the latter one we obtain the total cross section. In the following we resume the results of the [36] method based on Dyson-Feynman diagrams and Mandelstam invariants, which constitutes the theoretical framework of the Monte Carlo code CAIN [37, 38].

The differential cross section for an unpolarized photon by an unpolarized electron, without regard to their polarization after the scattering is given by [36]

$$d\sigma = 8\pi r_e^2 \frac{(mc)^2 dt}{(s-(mc)^2)^2}\Big[\Big(\frac{(mc)^2}{s-(mc)^2}+\frac{(mc)^2}{u-(mc)^2}\Big)^2 + \tag{1.6}$$

$$+\Big(\frac{(mc)^2}{s-(mc)^2}+\frac{(mc)^2}{u-(mc)^2}\Big)-\Big(\frac{u-(mc)^2}{s-(mc)^2}+\frac{s-(mc)^2}{u-(mc)^2}\Big)\Big] \tag{1.7}$$

where s, t, u are the Lorentz invariant quantities called *Mandelstam invariants* defined as

$$\begin{cases} s=(P_i+K_i)^2=(P_f+K_f)^2=(mc)^2+2P_iK_i=(mc)^2+2P_fK_f \\ t=(P_i-P_f)^2=(K_f-Ki)^2=2((mc)^2-P_iP_f)=-2K_iK_f \\ u=(P_i-K_f)^2=(P_f-K_i)=(mc)^2-2P_iK_f=(mc)^2-2P_fK_i \\ s+t+u=2(mc)^2 \end{cases} \tag{1.8}$$

with P_i, K_i, P_f and K_f the 4-momenta satisfying Eq. 1.2. In the laboratory frame in which the electron is at rest (ERF) before the collision, $P_i=(mc,0,0,0)$, the Mandelstam invariants are

$$s-(mc)^2=2mh\nu'_L, \quad u-(mc)^2=-2mh\nu', \quad t=-\frac{2h^2\nu'_L\nu'}{c^2}(1-\cos\theta') \tag{1.9}$$

and Eq. 1.3 gives in this frame ($\underline{\beta}_i=0, \gamma_i=1$)

$$\nu'=\nu'_L\frac{1}{1+\frac{h\nu'_L}{mc^2}(1-\cos\theta')} \tag{1.10}$$

where ν'_L and ν' are the photon frequencies before and after scattering in ERF and θ' the angle between their directions (see Fig. 1.4).

By using Eq. 1.10 we obtain

$$dt=-\frac{2h^2\nu'^2}{c^2}d\cos\theta'=\frac{2h^2\nu'^2}{c^2}\sin\theta' d\theta'$$

If we plug all of these equations in Eq. 1.6 we obtain the Klein-Nishina differential cross section [39]

$$\frac{d\sigma}{d\Omega'}=\frac{r_e^2}{2}\Big(\frac{\nu'}{\nu'_L}\Big)^2\Big(\frac{\nu'_L}{\nu'}+\frac{\nu'}{\nu'_L}-\sin^2\theta'\Big) \tag{1.11}$$

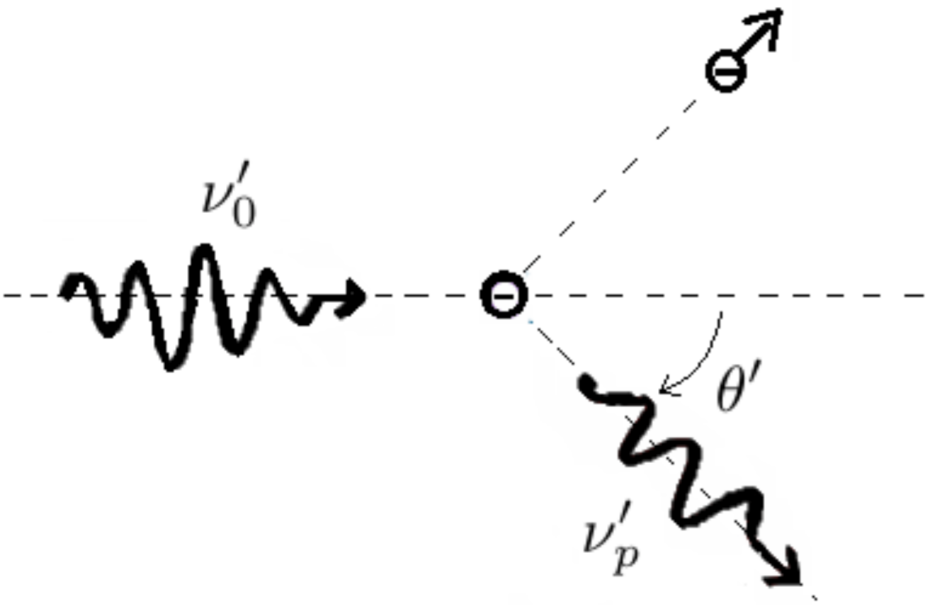

Figure 1.4. Scattering geometry in ERF: the incoming photon of frequency ν'_L hits the electron at rest, the electron is scattered and the emitted photon has frequency ν' and its direction forms an angle θ' with the incoming photon one. [40]

with $d\Omega' = \sin\theta' d\theta' d\phi'$. Since Eq. 1.10 sets a biunivocal correspondence between frequency and angle in ERF, the cross section can be expressed in terms of θ' as

$$\frac{d\sigma}{d\theta' d\phi'} = r_e^2 \Big(\frac{2}{2+\Delta(1-\cos\theta')}\Big)^2 \Big(\frac{1+\cos^2\theta'}{2}\Big)\Big(1+\frac{\Delta^2(1-\cos\theta')^2}{2(1+\cos^2\theta')(2+\Delta(1-\cos\theta'))}\Big)\sin\theta' \tag{1.12}$$

where $\Delta = 2h\nu'_L/mc^2$ is the parameter describing the effect of the recoil of the electron on the emitted radiation frequency value.

Finally, the total cross section can be obtained from Eq. 1.12 by integrating over θ' and ϕ'

$$\sigma_{tot} = w\pi r_e^2 \frac{1}{\Delta}\Big[\Big(1-\frac{4}{\Delta}-\frac{8}{\Delta^2}\Big)\log(1+\Delta)+\frac{1}{2}+\frac{8}{\Delta}-\frac{1}{2(1+\Delta)^2}\Big] \tag{1.13}$$

and

$$\begin{cases} \lim_{\Delta\to 0}\sigma_{tot} = \frac{8\pi r_e^2}{3}(1-\Delta) = \sigma_T(1-\Delta) & \text{non-relativistic case} \\ \lim_{\Delta\to\infty}\sigma_{tot} = \frac{2\pi r_e^2}{\Delta}\Big(log\Delta+\frac{1}{2}\Big) & \text{non-relativistic case.} \end{cases}$$

The limit for $\Delta \to 0$ is meaningful for the standard experimental conditions. For example, the recoil parameter associated with the head-on scattering of an electron with $E_e = 200MeV$ and a photon with $h\nu_0 = 2.4eV$ (typical experimental parameters) is given by

$$\Delta = \frac{4\gamma_i h\nu_0}{mc^2} = 1.5\cdot 10^{-3}.$$

1.2.1 Scattering between two particle distributions

Let us consider an electron beam and a laser pulse, moving in opposite directions in the LAB, identified by two different particle distribution, $f_e(\underline{r},\underline{p},t)$ and $f_L(\underline{r},\underline{k},t)$, respectively. The number of emitted photons per unit time dt and phase space volume $d\underline{p}d\underline{k}dV$ generated in the interaction is defined as

$$dN(\underline{r},\underline{p},\underline{k}) = \sigma_{tot}((\underline{p},\underline{k})\ c(1-\underline{\beta}_i\cdot\underline{e}_k)N_e f_e(\underline{r},\underline{p},t)N_L f_L(\underline{r},\underline{k},t)d\underline{p}d\underline{k}dVdt \tag{1.14}$$

where σ_{tot} is the total Compton cross section Eq. 1.13, N_e and N_L are the total number of electrons and photons involved in the interaction and $c(1-\underline{\beta}_i\cdot\underline{e}_k)$ is the relative velocity of the two beams.

The total number of scattered photons can be obtained by integrating Eq. 1.14. In particular, in the simplest case of an head-on collision occurring at waist of both beams, the total number of photons generated per shot can be approximated by

$$N = \mathcal{L}\sigma_{tot} \simeq \frac{N_e N_L \sigma_{tot}}{2\pi\sqrt{\sigma_x^2+\frac{w_0^2}{4}}\sqrt{\sigma_y^2+\frac{w_0^2}{4}}} \tag{1.15}$$

where $\mathcal{L}$ is the single collision luminosity, σ_x and σ_y are the transverse rms sizes of the electron beam and w_o the laser focal spot radius at $1/e^2$.

Eq. 1.15 is valid whenever we can neglect the diffraction of both the electron and laser beams across the interaction plane. This formula shows in first approximation the main ingredients needed to maximize the number of γ scattered photons: a high density of both electron and laser beams is necessary to compensate the low value of the Compton cross section which is of the order of one barn; it is also essential a precise space overlap and synchronization of the beams, correctly focalized at the interaction point.

Since N represents the total number of scattered photons per shot over the entire solid angle and the entire energy spectrum (from the minimum energy up to the maximum one, at the Compton edge), we should instead consider the beam of photons which is emitted within a small solid angle. It is in fact by selecting the part of the beam close to the emission axis (where the most energetic photons are emitted) that we create a high energy and quasi-monochromatic γ beam. The monochromaticity is measured in terms of relative bandwidth $\frac{\Delta\nu_p}{\nu_p}$, defined as the ratio between the rms and the mean frequency values

$$\frac{\Delta\nu_p}{\nu_p} \simeq \sqrt{\Big(\frac{\psi^2}{\sqrt{12}} + 2\frac{\epsilon_n^2}{\sigma_x^2}\Big)^2 + 4\Big(\frac{\Delta\gamma}{\gamma}\Big)^2 + \Big(\frac{\Delta\nu_0}{\nu_0}\Big)^2 + \Big(\frac{M^2\lambda_0}{2\pi w_0}\Big)^4 + \Big(\frac{a_0^2/3}{1+a_0^2/2}\Big)^2} \quad (1.16)$$

where $\psi = \gamma\theta_{max}$ is the acceptance angle, σ_x, ϵ_n and $\Delta\gamma/\gamma$ are the rms spot size at IP, the normalize projected emittance of the electron beam and the energy spread, respectively; $\Delta\nu_0/\nu_0$ is the laser bandwidth, M^2 the laser beam quality factor, λ_0 the central laser wavelength, w_0 the focal spot radius at $1/e^2$ and $a_0 = 4.3(\lambda_0\sqrt{E_L/\sigma_{z_L}})$ is the dimensionless amplitude of the vector potential associated to the laser electromagnetic wave, with E_L the energy of the laser and σ_{z_L} the rms laser pulse length.

Formula (1.16) holds in small θ angle approximation. The different contributions to the bandwidth increase are summed quadratically. In particular, the link between the bandwidth and the emittance of the electron beam is difficult to define, since the emittance and the acceptance angle are correlated in the contribution to the bandwidth spread. The last term represents the non-linear effects due to the laser intensity: when the laser parameter $a0$ is not much smaller than 1, multi-photon absorption starts being effective and the radiation spectrum is significantly modified in shape and frequency distribution. In order to achieve narrow bandwidth TS it is necessary to minimize these non-linear effects by using laser pulses characterized by small value of a0 (around 0.1).

Chapter 2

X-Ray generation at SPARC_LAB Thomson source

Frascati National Laboratories of INFN has a consolidated experience in electromagnetic radiation sources from inverse Compton scattering. In 1967 Malvano, Mancini and Schaerf [41] pointed out that a polarised beam of γ-rays with an energy and an intensity useful for photonuclear research could be produced by the interaction, in the straight section of a storage ring, of the high electron current circulating in it with the high photon intensity available inside a Laser optical cavity [42]. This was subsequently demonstrated at Frascati on the storage ring Adone where a fully polarised beam of $80MeV$ γ-rays was produced and used for several years for the study of photoreactions [43, 44, 45]. The same people have realized higher energy γ-ray beams at Brookhaven [46] and at ESRF [47].

Thanks to this knowledge of the phenomeno, a new test facility named SPARC_LAB (Sources for Plasma Accelerators and Radiation Compton with Lasers and Beams) has been recently launched at the INFN National Laboratories in Frascati [48]. In this facility a Thomson back-scattering source is presently under commissioning. Indeed, the opportunity has been used to couple the SPARC high brightness photoinjector [49] with the high power FLAME laser system in order to provide a X-ray Thomson source in the range $20 - 500keV$. The SPARC_LAB Thomson source design parameters have been optimized in order to obtain a radiation useful for X-ray imaging of mammographic phantoms with the phase contrast technique [50].

The Thomson back-scattering (TS) X-ray source [51] at SPARC_LAB is foreseen to work in three different operating modes: the high flux moderate monochromaticity mode (HFM2), suitable for medical imaging; the moderate flux monochromatic mode (MFM) suitable to improve the detection/dose performance [52, 53]; the short and monochromatic mode (SM) useful for pump-and-probe experiments, e.g. in physical-chemistry when tens of femtosecond long monochromatic pulses are needed.

2.1 The SPARC_LAB Facility

The facility (Fig. 2.1) is now operating, hosting a $150MeV$ high brightness electron beam injector [77], able to operate also in the velocity bunching configuration [78], which feeds a $12m$ long undulator. Observations of FEL radiation in the SASE [54],

Figure 2.1. SPARC_LAB layout. From bottom: the electron-gun (1) followed by the three TW accelerating sections (2). A THz station (3), that will host PWFA experiments, is located before the three quadrupoles and a RFD (4) for diagnostics and matching; these are then followed by the first dipole (5). Four beamlines follows the dipole, devoted to FEL physics (6) both in SASE and seeded (6b) schemes, beam diagnostics (7) based on EOS and THz radiation, plasma acceleration by LWFA (8), and X-rays production in the Thomson interaction chamber (9) by colliding the electron beam with the FLAME laser (10). The EOS laser comes from the photo-cathode laser room (11) and is delivered to the EOS station by using the EOS transfer line (12). [60]

Seeded [55] and HHG [56] modes have been performed from $500nm$ down to $40nm$ wavelength. A second beam line has been also installed and is now hosting a narrow band THz radiation source [57]. In addiction, INFN decided to host a sub-PW laser system, FLAME, that will be linked to the LINAC and devoted to explore laser-matter interaction, with particular attention to laser-plasma acceleration of electrons [58] in the self injection and external injection modes. The facility will be also used for particle driven plasma acceleration experiments, the COMB [59] experiment. A Thomson back-scattering experiment coupling the electron bunch to the high-power laser to generate a quasi coherent, monochromatic X-ray radiation is also in the commissioning phase.

2.1.1 SPARC_LAB accelerating structure

The SPARC_LAB photo-injector is composed by a 1.6 cell BNL/UCLA/SLAC type gun, operating at S-band (2.856 GHz) with high peak field (120 MV/m) on the incorporated metallic photocathode (Cu), generating a 5.6 MeV electron beam with a quantum efficiency in typical conditions of about few 10^{-5}. The gun is

then followed by three S-band travelling wave (TW) sections (hereinafter called S1, S2 and S3) whose accelerating gradient boosts the beam energy up to 180 MeV. The first one is also used as RF compressor (velocity bunching regime) by varying the beam injection phase. Solenoid coils embedding the first two sections can be powered to provide additional magnetic focusing to better control the beam envelope and the emittance oscillations under RF compression. A diagnostics transfer line allows to fully characterize the accelerated beam by measuring transverse emittance [61], longitudinal profile, and slice emittance through a Radio-Frequency Deflector (RFD) [62]. The current layout follows a detailed theoretical study of the emittance compensation process in a photoinjector [76]. It has been demonstrated that the best optimization is achieved by propagating the beam through the device so that emittance oscillations produced by space charge collective forces are damped while the beam is accelerating [63]; the basic point in the design of a photo-injector is therefore the properly match of the beam from the injector to the accelerating sections. In fact, being the brightness a figure of merit defined as [64]

$$B = \frac{2I}{\pi^2 \epsilon_x \epsilon_y} \tag{2.1}$$

where I is the beam current and $\epsilon_{x,y}$ is the normalized emittance, to increase the brightness high current and small emittance beams are required. It has been predicted [65] and then measured [77] that the proper tuning of the emittance oscillation can be achieved by injecting the beam into the linac when the emittance reaches its relative maximum. By using the SPARC_LAB gun, located at a distance of $1.5m$, the second emittance minimum is moved to the linac output, allowing to obtain high brightness and low emittance beams. This working point is called *Ferrario's working point* and it is widely used in photo-injectors.

2.1.2 Thomson beamline

The installation of the Thomson beamline has been completed in the 2013 with a transfer line for the electron beam together with a photon beamline that brings the laser pulse from the FLAME bunker to the interaction with the electron beam. In this configuration the electron beam energy can range from $28MeV$ to 150 MeV, and the electron beam transport is meant to preserve the high brightness coming from the LINAC and to ensure a very tight focusing and a longitudinal phase space optimization for the whole energy span. The general layout is showed in Fig. 2.1, where the electron transfer line departs from a three way vacuum chamber inside the first dipole downstream the RF deflector used for the six-dimensional phase space analysis of the electron beam. This dipole is also part of the 14° dogleg that brings the electron beam up to the SPARC THz source. The electron beamline continues in a $30m$ double dogleg starting, as mentioned, downstream the SPARC photoinjector; they ends in a two branch beam delivery line that provides two separate interaction regions with the possibility to host two different experiments at the same time: the Thomson source and the external injection in a plasma accelerator experiment. The total beam deflection is about 6 m from the photoinjector and undulator axes. A total of six rectangular dipoles and 19 quadrupoles are needed to drive the electron beam up to the two interaction points.

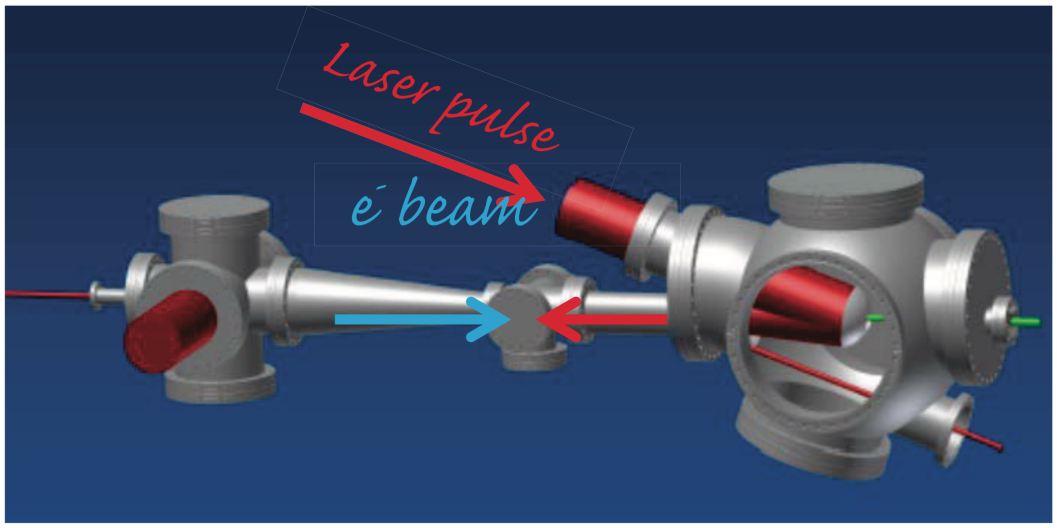

Figure 2.2. Thomson interaction geometry layout. The FLAME laser is focused by means of an off axis parabolic mirror with $f = 750mm$. On the other hand, the electron beam, counter-propagating with respect to the laser, is focused with a solenoid placed before the IP chamber. [48]

The Thomson interaction vacuum chamber, see Fig. 2.2, consists in two mirror stations that will determine the in and out trajectory of photon beam, plus an interaction chamber in the middle that hosts the diagnostic for both electron and photon beams. The parabolic mirror located downstream the interaction point will focus the photon beam at the interaction point down to a $10\mu m$ spot size, its spatial adjustment is obtained with its x-y movable support that can be also remotely controlled. The interaction chamber is a tee-vacuum chamber where a double screen movement will be mounted to get the imaging of both electron and photon beams at the interaction point. The laser beam transfer line to the interaction region is composed by a series of high reflectivity mirrors inserted in a $50m$ long vacuum pipe. The mirrors, 8 inches diameter, are supported by motorized Gimbal mounts in order to assure the alignment up to the off-axis parabola that focus the laser pulse on the electron beam. The vacuum of the photon beam line is about $10^{-6}Torr$.

2.1.3 Synchronization system

The Thomson scattering experiment needs an extremely precise synchronization between electron bunch and laser pulse. The relative time of arrival jitter of two beams is fundamental to obtain a repeatable and efficient interaction. The electrons and photons have to be synchronized with a relative jitter $< 500fs$.

In order to achieve specified performances for the next future experiments at SPARC_LAB, a very demanding synchronization between the subsystems is required. In particular, two laser systems (SPARC photocathode and FLAME) have to be synchronized with a relative time jitter of $< 500fs$ r.m.s. and $< 30fs$ r.m.s. for the Thomson X- ray source and Plasma acceleration experiments, respectively. The synchronization reference is presently distributed through coaxial cables along the facility. The measured performances fully meet the Thomson

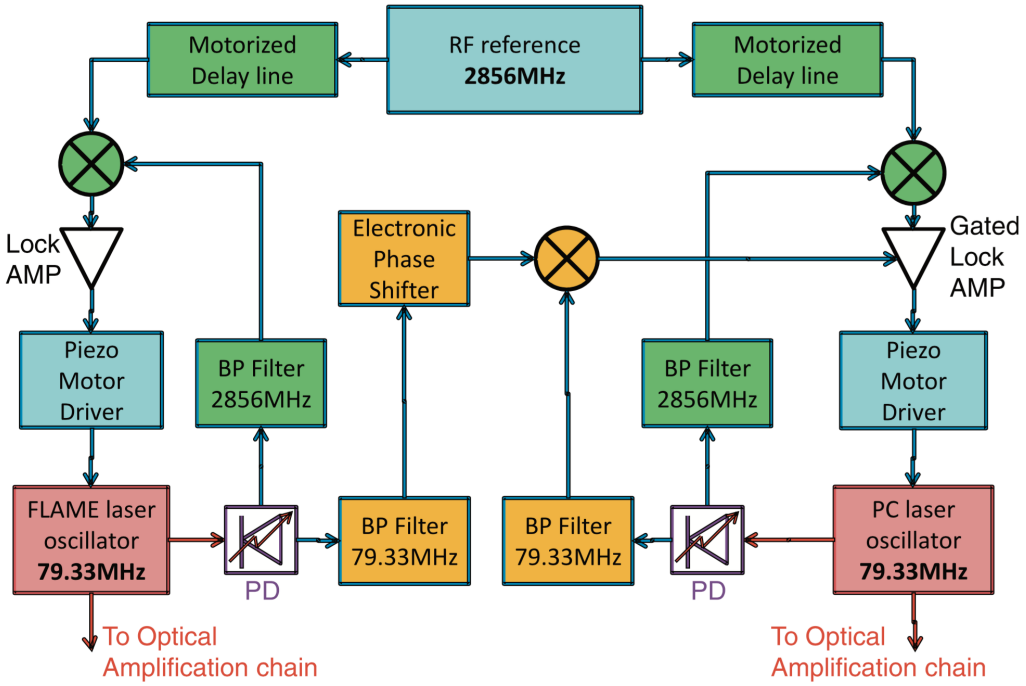

Figure 2.3. Sketch of the lasers synchronization scheme used in the Thomson scattering experiment. [48]

experiment requirements.

Fig. 2.3 shows the schematics of the hardware configuration that synchronizes the two laser oscillators (and consequently the electron bunch and the FLAME amplified pulse at 10 Hz rep. rate). Two Phase Locked Loops working at 2856 MHz (the SPARC linac frequency, equal to the $36th$ harmonics of the rep rate of the lasers) represented by the green boxes are used to independently synchronize two laser oscillators to the RF reference with a time jitter $< 100fs$ r.m.s. . The harmonic loop could lock the two lasers at any of 36 different relative time separations within one period of the laser rep rate $T_{Las} = 12.6ns$. To select only one lock position and reject the others we added an ancillary PLL working at the laser fundamental frequency (orange boxes). This acts on the error amplifier of one harmonic loop opening a time window whose duration is only 1/36 of T_{Las}. A 360° electronic phase shifter in the fundamental loop allows moving the gating window along an entire laser period for a coarse control of the relative position of the pulses, while the fine positioning is obtained by moving the motorized delay lines transporting the reference signal to the harmonic loops.

To achieve better performances, especially in the phase detection process, we need to migrate towards optical reference signal distribution architecture. We have already purchased and installed an Optical Master Oscillator (OMO), which is presently under test. Also we have partially installed the fiber links to bring the signal to the clients (laser oscillators, RF power station, diagnostics). Next step is to characterize the high resolution optical phase detectors (cross-correlators) that will guarantee a minimal time jitter resolution of the order of $1fs$.

To guarantee a stable operation in both electrical and optical reference signal distribution, we are designing the system including a link stabilization apparatus. The optical stabilized links are nowadays available on the market, providing residual drifts of the order of $10fs$ r.m.s. in point-to-point reference distribution. Concerning the coaxial cable distribution, we are developing a link monitor that can diagnose the drifts of the signal path length. We will use this information to close a pulse-to-pulse feedback loop, compensating the drift using the motorized delay lines.

2.1.4 The sub-PW FLAME Laser

The custom-made FLAME Amplitude Technologies laser is a Ti:Sa system based on CPA scheme [66] that can deliver, after the optical compressor, up to $300TW$ peak power ($6J$, $20fs$ Full Width Half Maximum (FWHM)) ultrashort laser pulses at $800nm$ with a $10Hz$ repetition rate.

A general layout of the FLAME laser is shown in Figure 2.4. The seed of the whole system is generated by a mode-locked oscillator, with a $80nm$ bandwidth centered at $800nm$ and a repetition rate equals to $79.333MHz$. The system features a front-end part with pulse contrast enhancement (booster) and regenerative amplifier, yielding pulses with $0.7mJ$ in $80nm$ bandwidth at $10Hz$. This bandwidth is controlled thanks to two acousto-optic devices, Fastlite Dazzler, performing simultaneous and independent spectral phase and amplitude programming of ultrafast laser pulses, and Mazzler, a programmable intra-cavity gain filter allowing fine control of regenerative amplifiers' spectral gain. At the exit of this first stage, including also a stretcher, in order to elongate the laser pulses up to hundreds of picoseconds, they are further amplified by the first amplifier up to the $25mJ$ level while the second amplifier brings the energy up to $600mJ$. The third cryogenic amplifier is based on a $5cm\ x\ 5cm\ x\ 5cm$ Ti:Sa crystal pumped by 10 Propulse+, frequency doubled Nd:YAG lasers, for a total of up to $20J$ of energy per pulse. The extraction energy is as high as 35%, leading to a final energy in the stretched pulses up to $7J$, with a good r.m.s. stability less than 1%. Pulses are then transported in air to the vacuum compressor placed in the underground target area. Once compressed, the laser beam is transported under vacuum ($10^{-6}mbar$) to the target chamber through remotely controlled beam steering mirrors.

2.2 Experimental results

2.2.1 First commissioning run

For the first commissioning phase, the beams described in Tab. 2.1 have been chosen to collide at the Thomson IP. The detected signal has been measured both with a 20GHz BW oscilloscope, for a fast response, and a multichannel analyser, to acquire an integral measurement over various interactions. The 20 Ghz BW oscilloscope has been mainly useful to synchronise the electron beam and FLAME pulse and allows to measure the 150 fs relative temporal jitter between them. The multichannel analyser provided the evaluation of average energy of X-ray and of the number of photons produced in the interaction. The detected signal, integrated over 1200 pulses, is shown in Fig. 2.5 on the left.

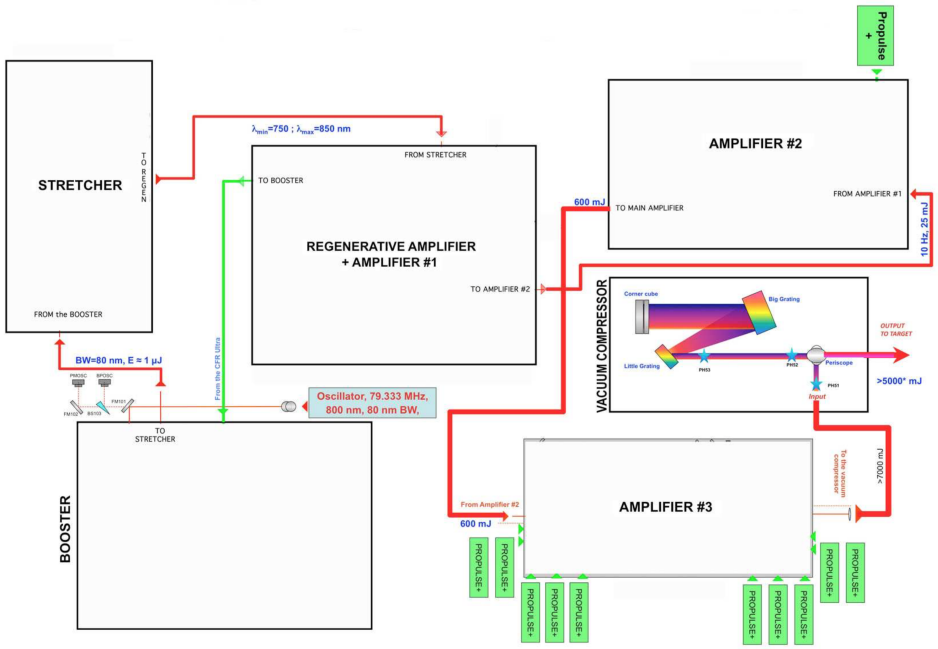

Figure 2.4. Schematic layout of FLAME laser. The 80MHz beam provided by the oscillator is sent to the Booster amplifier, where the repetition rate is fixed at 10Hz by means of a Pockels cell. As the CPA scheme works, the pulses are stretched and sent to the whole amplifier chain: regenerative amplifier, first, second and third multipass. At last, each pulse is shorten by an optical compressor, consisting in four diffraction gratings, providing an opposite chirp with respect to the one of the stretcher. From here, the beam can follow two different paths: to SPARC bunker for Thomson backscattering experiments or to FLAME bunker for plasma-based experiments.

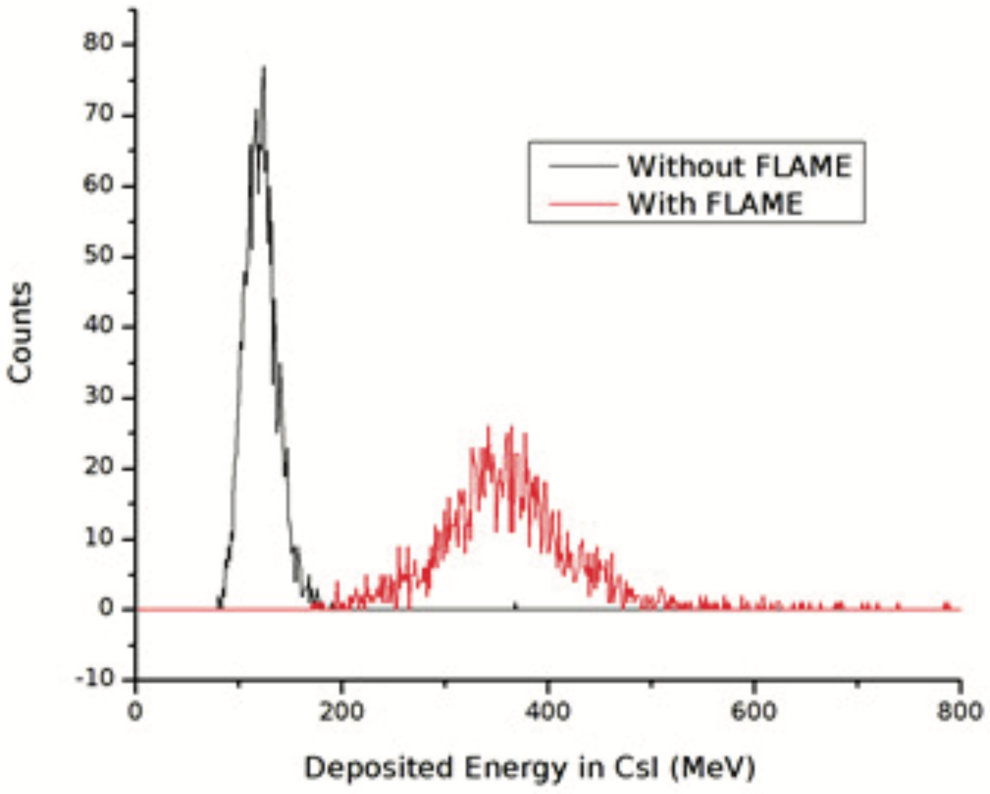

Figure 2.5. Experimental results of the first Thomson based X-ray source commissioning run @ SPARC_LAB. The horizontal axis represents the energy deposited by the electron inside the CsI(Tl) crystal, properly calibrated by means of well known radioactive source in ordet to relate it to the photon energy. The black line represents the background signal, without the laser on IP, due to the electrons hitting the interaction chamber and producing Bremstralung. The red line is revealed when there are both the electron beam and the laser. [67]

Electron Beam	Energy	MeV	50
	Energy Spread	%	< 0.1
	Charge	pC	200
	Pulse length	ps	3.1 ± 0.2
	Spot size	μm	90 ± 3
	Emittance	mm mrad	$1.5 - 2.2 \pm 0.2$
Laser Beam	Pulse energy	J	0.5
	Pulse length	ps	6
	Spot size	μm	10 ± 3
	Rep. rate	Hz	10
	Wavelength	nm	800
X-Ray Beam	Photon energy	KeV	60
	Photon number per shot		6.7×10^3
	Bandwidth	%	19

Table 2.1. SPARC_LAB Thomson source experimental parameters for first commissioning run.[50]

Here, the red signal is due to the Thomson X-rays, instead the black one is due to the background noise in case of FLAME pulse switched off. The background is synchronous with Thomson X-rays and it is mainly due to radiation produced in the electron beam dumping section located downstream the vacuum chamber hosting the parabolic mirror focusing the laser beam, being it too much close to the X-rays radiation extraction. The average energy of Thomson X-rays, released in the crystal by each pulse, is of about $235MeV$. By CAIN simulation of the interaction it has been possible to evaluate that the average energy of the photons reaching the detector was $60keV$ with, in average, 6.7×10^3 photons per each pulse interacting with the detector sensitive area. This result has been confirmed by simulations made with a code based on the classical theory [68]: in case of a $50MeV$ electron beam with 200 pC charge, 5 mm mrad of emittance and $150\mu m$ spot size rms head-on colliding with a $500mJ$ energy laser pulse and a $30\mu m$ beam waist, should be produced a X-ray signal of 2×10^5 photons per pulse in a bandwidth of about 19%. The predicted photon energy edge is of 63keV given by $E_p \sim 4E_L\gamma^2$. The result is reported in Fig. 2.5 on the right. Poor overlap conditions due to some misalignment of the interaction vacuum chamber can explain the difference between the measured number of photons for each pulse and the one expected from the theory.

2.2.2 Second commissioning run

The second commissioning shift has taken place during the 2015 summer [69] with more relaxed parameters (Tab. 2.2). To verify the collision alignment and synchronization the X-ray detection is a fundamental diagnostic tool. In the commissioning phase a detector that allows to measure the X-ray yield is required to possess a high sensitivity and a wide dynamic range to detect the potentially weak signal generated in the first non-optimised collisions. The detector we selected is a scintillator crystal

Electron Beam	Energy	MeV	30
	Energy Spread	%	< 0.1
	Charge	pC	$100 - 800$
	Pulse length	ps	3.1 ± 0.2
	Spot size	μm	$60 - 80$
	Emittance	mm mrad	$1 - 3 \pm 0.2$
Laser Beam	Pulse energy	J	$1 - 5$
	Pulse length	ps	6
	Spot size	μm	10 ± 3
	Rep. rate	Hz	10
	Wavelength	nm	800
X-Ray Beam	Photon energy	KeV	$20 - 22$
	Photon number per shot		10^9
	Bandwidth	%	$10 - 20$

Table 2.2. SPARC_LAB Thomson source design parameters for second commissioning run.[69]

coupled with a photomultiplier tube (PMT) located at 450 cm downstream the Thomson IP. The crystal used is a CsI(Tl) of size (20 x 20 x 2) mm^3, coupled with a light-guide to a PMT (Hamamatsu, mod. R329-02). The signal is acquired using both an oscilloscope and a multichannel analyser (MCA-8000, Amptek, US) connected to a PC. Due to the high intensity and short duration of the pulse, it is not possible to distinguish the signal produced by the interaction of each single photon , as in traditional spectroscopic application, but the signal is proportional to the entire energy released in the scintillator by each pulse. Therefore, an information on the energy distribution is required to evaluate the number of photons in each pulse. To calibrate the detector response, the signal produced by two radioactive sources 241 Am (59.54 keV) and 137 Cs (662 keV) was performed as a function of the HV applied and the amplificator gain; adjusting the HV and gain it is possible to detect signals in a wide range. In addition to the PMT described, the beamline is equipped with a set of Si PIN diode detectors, previously calibrated with monochromatic synchrotron light, located at 200 and 300 cm from IP respectively, that, together with an X-ray imager and techniques specifically developed [71, 70], allow a full characterization of the X-ray source in terms of flux, energy distribution, spatial distribution and beam stability.

For the selected working point with 200 pC and 30 MeV electron beam at the Linac exit the measured normalized transverse emittance was $\epsilon_{x-y} = 1.2 - 2.2 \pm 0.2 \mu rad$, with an energy spread $\sigma_\delta = 0.1 \pm 0.03\%$, and a r.m.s. length $\sigma_z = 2.2 - 0.2 ps$. The minimum electron beam size reached was $\sigma_{x-y} = 60 - 80 \pm 10 \mu m$. Due to background problems on the X-ray detectors, placed relatively close to the electron beam dumper, we should limit the IP electron spot size to $\sigma_{x,y} = 110 \pm 10 \mu m$. In fact, due to a residual misalignment of the electron beam with respect to the dumper vacuum pipe (enhanced by the strong focusing field of the last solenoid), the background increased when the beam divergence was higher as a consequence

of a stronger focusing at IP. This misalignment was also detected by the imager recorded data that are shown in Fig. 2.7 where the Thomson radiation image is clearly cut by the Perspex CF 40 window profile. To measure the radiation energy two k-edge filters, Nb and Zr, were also used, resulting in a roughly estimated value of 13 keV, confirming the cut of the most energetic part of the produced radiation due to the tilted electron trajectory. In fact, with our commissioning set-up the expected number of photons in the 20% bandwidth is [72]

$$N_\gamma = \frac{U_L[J]Q[pC]\delta_\phi}{h\nu[eV](\sigma_x^2[\mu m] + \frac{w_0^2[\mu m]}{4})} \sim 1.4 \times 10^6 photons/shot$$

with $U_L = 2J$,$Q = 200pC$,$\delta_\phi = 0.2$,$h\nu = 1.55eV$,$\sigma_{x,y} \sim 110\mu m$ and $w_0 = 150\mu m$, while our measured photon flux is $N_\gamma \sim 10^4 photons/pulse$.

Another contribution to the reduction of the obtained photon flux can also come from the jitter sensitivity of our 30 MeV working point, deeply off crest in the S-band accelerating sections, as coming out from the simulation results shown in Fig. 2.6, where the Thomson radiation spectrum is shown as calculated with CAIN code starting from the measured parameters for the electron and photon beams (Fig. 2.6 above) and its sensitivity to the jitter of electron beam horizontal centroid is shown in terms of photon flux reduction (Fig. 2.6 below).

2.3 Future outlook

As reported in the previous section, in the second commissioning run, a $30MeV$ electron beam energy working point, delivering a maximum X-ray energy of $20keV$, has been addressed as foreseen for the first planned imaging experiment. With the available hardware (only phase shifters on the 3 S-band sections) the applied acceleration/deceleration scheme worked well enough to produce a low energy spread electron beam at $30MeV$, even though resulting in a strong sensitivity for the electron beam to the machine imperfections/stability. The measured flux was almost the same of the previous run ($\approx 10^4$) and was two orders of magnitude less than the theoretical one as well. This time has been possible to install a X-ray CCD and make an image of the interaction chamber exit window and a clear misalignment has been detected.

Following the experimental results of the two runs, the optimization plan foresees a better control of the electron trajectory at the IP to avoid unrecoverable off-axis emission of the Thomson radiation and too high background contribution to the X-ray detectors signal. An interaction setup upgrade is also under study, coming to a non-zero angle collision in order to make it easier the electron and laser pulse trajectory control removing the on axis counter propagation that limit the room availability for both beams diagnostic.

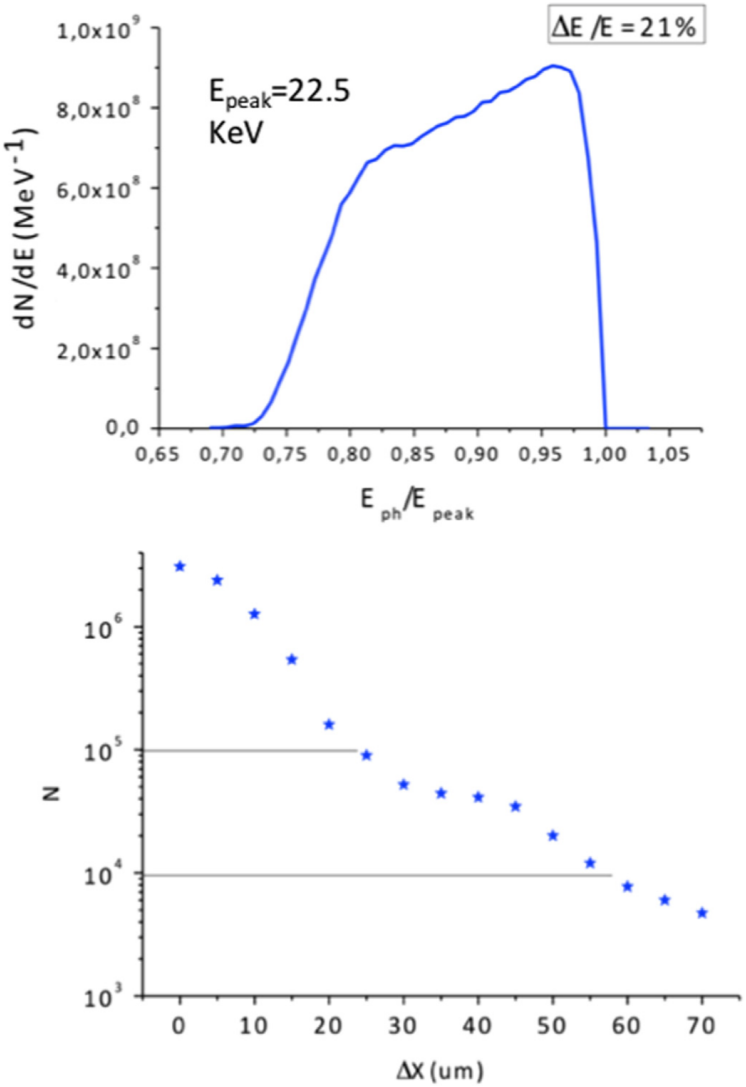

Figure 2.6. Thomson X-radiation spectral distribution calculated from the measured electron and laser beam parameters for the second commissioning shift (top) and the relative photon flux reduction estimation coming from the jitter in the transverse electron beam centroid (bottom).[69]

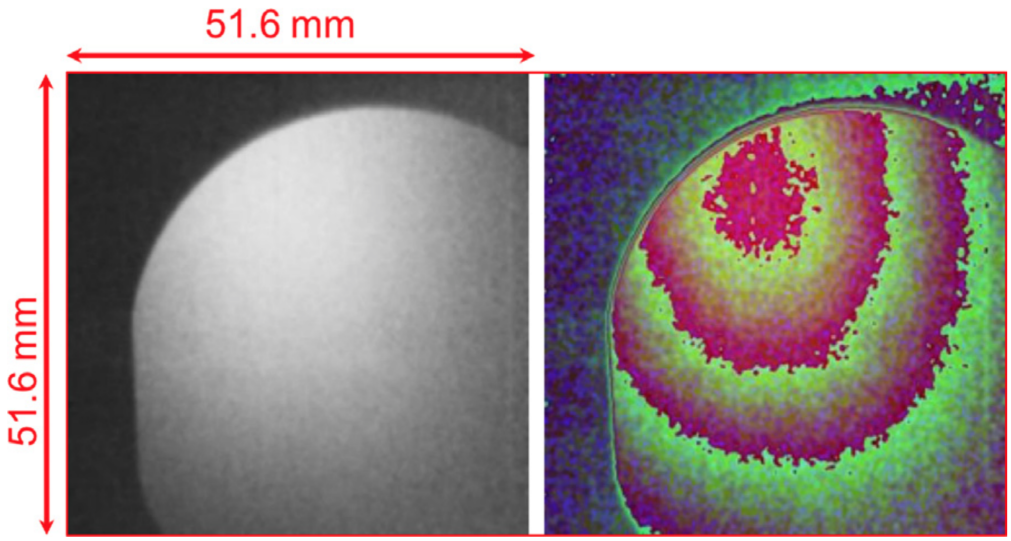

Figure 2.7. Thomson X-radiation image collected with Hamamatsu imager Flat Panel C9728DK-10, located at 300 cm from the IP, with 1 s exposure time and averaged over 100 images. [69]

Chapter 3

The S.T.A.R. Project: Southern european Thomson source for Applied Research

The STAR project (Southern european Thomson source for Applied Research), in progress at the Univ. of Calabria (Italy), aims at the construction of an advanced Thomson source of monochromatic tunable, ps-long, polarized X-ray beams, ranging from 20 to 140 keV [73, 74]. The project is pursued in collaboration among different partners: Univ. of Calabria, CNISM, INFN and Sincrotrone Trieste. The X-rays will be devoted to experiments of matter science, cultural heritage, advanced radiological imaging with micro-tomography capabilities. One S-band RF Gun at $100Hz$ will produce electron bunches boosted up to $60MeV$ by a $3m$ long S-band TW cavity. A dogleg will bring the beam on a parallel line, shielding the X-ray line from the background radiation due to Linac dark current. The peculiarity of the machine is the ability to produce high quality electron beams, with low emittance and high stability, allowing to reach spot sizes around $15 - 20\mu m$ r.m.s., with a pointing jitter of the order of a few microns. The collision laser will be based on a Yb:Yag $100Hz$ high quality laser system, synchronized to an external photocathode laser and to the RF system to better than $1ps$ time jitter.

In the following chapter, after a brief introduction about this project, the main task of my work, concerning the commissioning, design of transverse shaping system and the transport line of both laser beams, will be shown.

3.1 Project overview

The STAR facility site is located in the Univ. of Calabria campus, in Rende (CS, Italy). The STAR source will be located in a new building expressly designed to host it in its present layout (Fig. 3.1). The building is a $50 \times 25 \times 6.7(h)$ m hangar in which the bunker ($37 \times 12 \times 3.5(h)$ m), the laser clean room and the X-ray site for users are sited. Three satellite structures are connected to the Hangar to host the control room and the electrical and conditioning systems. The radiation shielding were designed for electron energies up to $350MeV$, thinking to future upgrades, while several passive seismic monitoring experiments at different conditions were

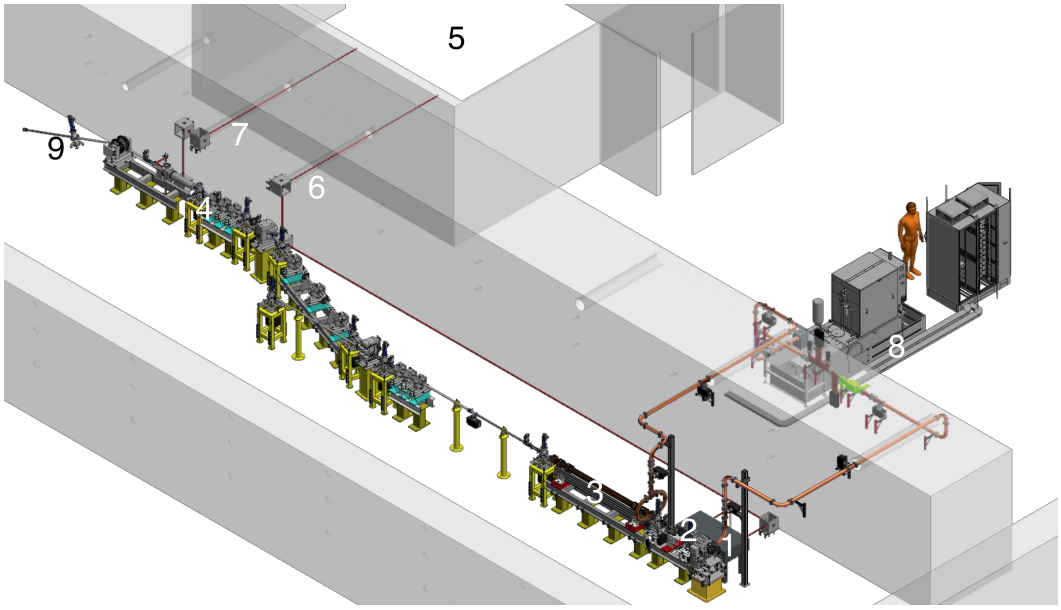

Figure 3.1. Schematic layout of STAR machine: 1) photoinjector, 2) solenoid for emittance correction, 3) S-band Traveling Wave accelerating cavity, 4) Interactio Point (IP), 5) laser clean room, 6) Photocathode laser transport line, 7) Interaction laser transport line, 8) Klystron and modulator area, 9) electron beam dump.

carried out allowing us to exhaustively characterize the seismic noise in terms of the power and space-time variability, both in frequency and wavelength [75].

The STAR LINAC (Fig. 3.1) is based on a S-band 1.6 Cell RF Gun, with a Cu photocathode, followed by one S-band SLAC-type $3m$ long Traveling Wave (TW) accelerating cavity. After the Gun, where the beam is charge dominated and laminar, a solenoid, coupled with a TW cavity (placed in ad hoc position) performs the emittance correction [76]. This schema, studied and tested at SPARC_LAB [77, 78], is directly passed to the STAR project by the same people, involved in both the projects. The good beam quality provided at the LINAC exit (emittance $\epsilon_{x,y,z} = 0.9\mu m$, energy spread $\Delta\gamma/\gamma = 0.2\%$) for the quite high bunch charge of $Q_b = 500pC$, will permit to pass through the dogleg and to reach the Interaction Point (IP) with a very narrow final spot of $15\mu m$ (or even smaller) r.m.s. in the transverse plane.

3.2 STAR laser systems

The STAR Facility features two laser systems: one is devoted to the electron production, exploiting the photoemission impinging on a Cu cathode; the other will provide the IR photons for the interaction. Both the systems, custom-made by Amplitude Systèmes, will be located in a dedicated Clean Room that will provide the required thermal stability ($\pm 0.1°C$) to minimize the laser energy fluctuations.

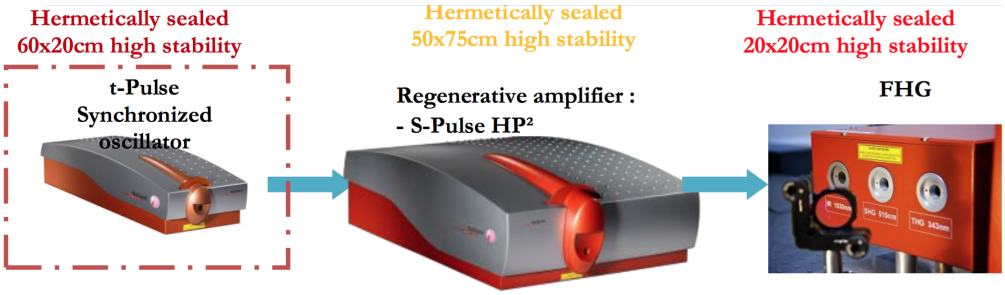

Figure 3.2. Schematic layout of STAR photocathode laser chain.

3.2.1 Photocathode laser

The laser set-up is a high energy, high stability femtosecond amplified laser with a frequency conversion module. It consists of a femtosecond oscillator synchronized to an external triggering signal, a pulse stretcher, a regenerative amplifier, a compact pulse compressor and a fourth harmonic frequency converter. The laser takes full advantage of direct diode-pumping technology, leading to a more compact, reliable and user-friendly system. Moreover, the laser takes full advantage of an Ytterbium gain material, able to operate identically from single pulse to $100Hz$ repetition rate, with a high short-term and long-term stability.

The oscillator is a standard product from Amplitude Systèmes, from the t-Pulse series, a diode-pumped ultrafast oscillator delivering $1W$ average power at $1030nm$, with $200fs$ pulse duration, at a repetition rate of $50MHz$. The repetition rate is adjusted with a precision of 100Hz and a tunability of $\pm 2kHz$, to compensate for potential drift of the reference signal frequency. The laser cavity is actively stabilized and synchronized to an external reference : an electronic feedback loop activates a piezoelectric actuator in the cavity for fast (kHZ) feedback and an additional translation stage for slow feedback. This active stabilization allows to achieve a timing jitter lower than $500fs$ integrated on $10Hz$ to $1MHz$ frequency range. The cavity is compact and sealed, ensuring stability and environmental isolation.

The amplifier laser head, corresponding to the s-Pulse HP2 model, a standard industrial product of Amplitude Systèmes, consists in a compact stretcher, a regenerative amplifier, an adjustable compressor, as well as various diagnostics and monitors. Those elements are integrated in a hermetical housing, which is temperature stabilized at a constant temperature. slightly above the ambient This compact integration allows is allowing for a high compactness and stability. The laser heads are integrated in a hermetical housing and can be used in an industrial environment. To maintain long term stability, the laser housing is set at a constant temperature.

The laser amplifier is pumped by high power, highly reliable telecom-class laser diodes. A small, telecom-class laser diode pumps the oscillator. The pumping diodes are operated significantly below their maximum rated currents in order to enhance their lifetime together with the system long term stability. The stretcher is based on high efficiency gratings, used in a compact setup, designed to stretch the pulses delivered by the femtosecond oscillator to a duration of approximately $300ps$. The gratings are gold-free, and therefore can be cleaned like standard optics

Output energy	mJ	2
Energy stability r.m.s.	%	<1
Central wavelength	nm	1028
Spectral bandwidth FWHM	nm	4
Pulse duration FWHM	ps	5
Rep. rate	Hz	1-100
Spatial profile (M^2)		<1.3

Table 3.1. STAR photocatode laser parameters at the optical compressor exit.

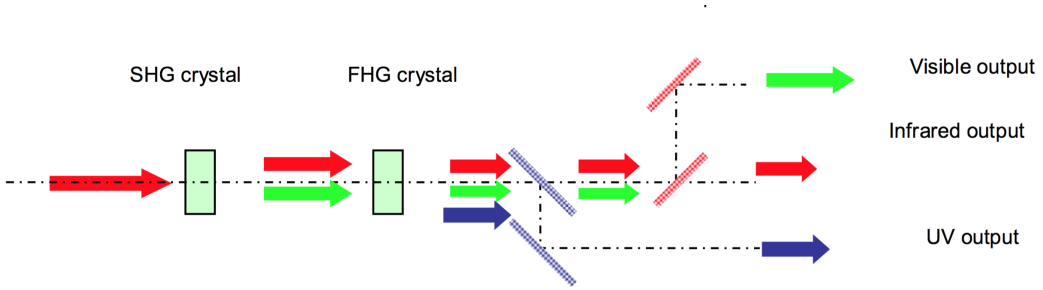

Figure 3.3. Set-up of the frequency converter for UV generation.

if necessary, which highly improve the long term performance of the pulse stretcher. The regenerative amplifier is based on Yb:KYW material, delivering up to $2,5mJ$ of energy at $100Hz$. The output spectrum is $4nm$ wide. A high pulse-to-pulse stability and pointing stability is ensured by the integration of the regenerative cavity in a highly rigid metallic, sealed structure. The compressor is composed of highly efficient diffractive gratings, based on multilayer dielectric mirrors, allowing for recompressing the pulses up to $5ps$ pulse duration with an overall efficiency of 60%. At this level of peak power, the nonlinear effects in the air are still negligible in the compressor. Therefore the compressor does not require to be placed in a vacuum chamber. The laser parameters at the optical compressor exit are resumed in Tab. 3.1.

The frequency converter consists in two nonlinear conversion stages, in order to convert a part of the infrared beam at $1030nm$, into a high beam quality ultraviolet beam at $258nm$. The first stage is a second harmonic generation stage, designed to convert the fundamental wavelength of 1030nm into $515nm$ wavelength radiation. The setup consists in a BBO crystal used in type I configuration. The conversion efficiency is adjusted to 50%, in order to keep the excellent beam quality. The second stage is a second harmonic generation designed to convert the 515nm beam into $258nm$ wavelength radiation. The setup consists in a BBO crystal used in type I configuration. The conversion efficiency from green to UV is designed to achieve $> 40\%$, together with an excellent beam quality. The overall conversion efficiency from IR to UV is then $> 15\%$. Dielectric filters are then used to isolate the UV beams by spatially separating the IR, green and UV radiation.

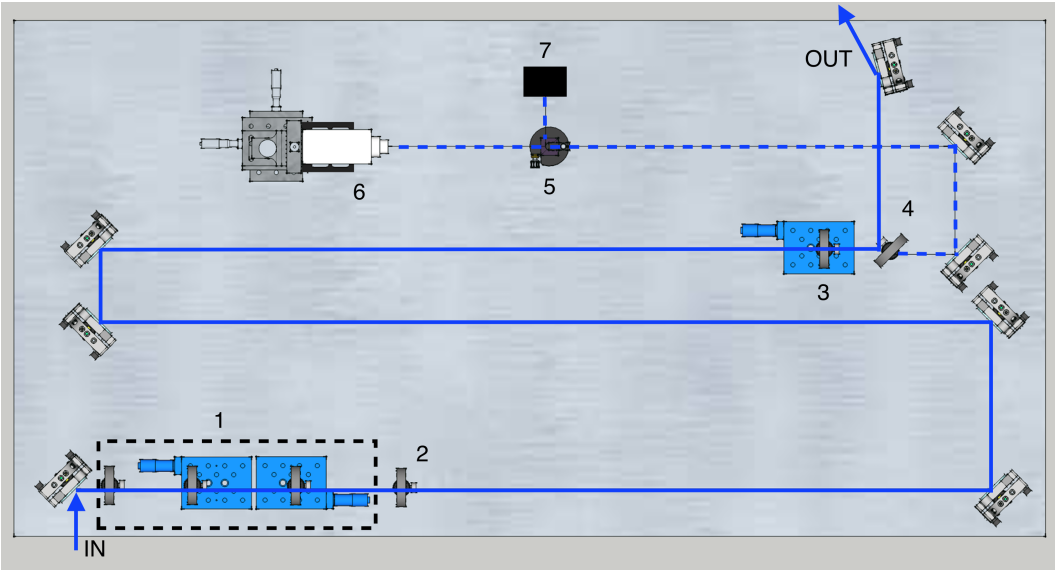

Figure 3.4. Layout of the optical table hosting the laser beam transverse spatial profile shaping. 1) variable zoom lens system constituted by two convex and one concave lenses , 2) motorized iris to opportunely cut the wings of gaussian distribution , 3) lens for final imaging of iris plane on the cathode, 4) and 5) Beam Splitters, 6) CCD camera for beam profiling (Thorlabs BP-106UV), 7) energy meter. The solid line represents the principal laser beam, the dashed line is the diagnostic beam for energy and profile measurements.

Photocathode laser transverse profile shaping

In order to achieve the best electron beam at the exit of the gun, it is crucial to properly optimize the photocathode laser parameters. Particular attention has been given to the laser transverse profile shaping, aiming to generate the lowest emittance beam at the photoinjector. In detail, for a given smooth-Gaussian laser temporal profile, a recent work [79] shows that a truncated-Gaussian laser spatial profile produces an electron beam with smaller emittance.

In order to apply this result to the STAR machine, a dedicated optical station close to the photoinjector has been designed. In Fig. 3.4 the layout of the specified set-up is shown. Three lenses placed on two motorized linear stages work as a variable telescope in order to set the laser spot size hitting a remotely controlled iris to properly cut the gaussian profile. Then, another lens make an image of the iris plane on the cathode. The lens focal lengths and the distances among them has been optimized by simulating the set-up with Zemax, a lens design software.

The optical station will be equipped also with Thorlabs BC106N-UV beam profiler, installed on an ancillary line, to check the imaging and, by using a specific algorithm, the energy level and stability. For this online measurements, a small fraction of the principal laser beam will be splitted and sent to a secondary path (see Fig. 3.4).

3.2.2 Interaction laser

The interaction laser architecture is similar to the photocathode laser system, but with a higher maximum energy achievable. It consists in a chirped pulse amplification system composed of an oscillator, a fiber-based stretcher, a regenerative amplifier, a multi-pass amplifier and a compressor.

The oscillator is a replica of the photocathode laser one, delivering $1W$ average power at $1030nm$, with $200fs$ pulse duration, at a repetition rate of $50MHz$, adjusted with a precision of $100Hz$ and a tunability of $\pm 2kHz$, to compensate for potential drift of the reference signal frequency.

A particular feature of this system concerns the stretcher. Indeed, it is a compact system based on chirped fiber Bragg grating technology. Due to a precise control of the Bragg grating density along the fiber, this technology gives access to a customized spectral phase profile, allowing to adjust second order and third order of dispersion to compensate exactly for the dispersion of the compressor to be used. The typical dispersion of such a component is about $150ps/nm$ per piece, on a bandwidth of $6nm$. The overall efficiency is about 30%.

The regenerative amplifier is based on thin disk Yb:YAG, delivering up to $30mJ$ energy at $100Hz$. The output spectrum is $1nm$ due to gain narrowing. A high pulse-to-pulse stability and pointing stability is ensured by the integration of the regenerative cavity in a highly rigid metallic, sealed structure.

Thanks to the second amplifier, the interaction laser will provide, after compression, $5ps$ FWHM pulses at $100Hz$ of repetition rate and an energy level up to $130mJ$. The expected r.m.s. laser energy stability is around 3% (over 1000 shots) with a long term peak-to-peak fluctuation below 5%.

3.3 Optimization of Interaction Point geometry

The IP region, in the TS sources, is clearly of main importance. At STAR two different interaction schemes have been considered, both with an angle between laser and electron beams at the IP. In Fig. 3.5 is shown the effect of this angle on the source photon flux, as simulated by the code CAIN [80]. The head-on scattering, which is possible by using an on-axis holed focusing parabola and which should ensure a higher flux, has been considered unfavourable by previous experiences done at SPARC_LAB, mainly concerning background radiation issues. A scheme with all the laser optics out of the electron beam line seems advantaged from alignment and operation point of view.

The first IP scheme was based on the most advanced state of the art, for the Beam Position Monitors (BPM), by using "cavity" BPMs ($< 1\mu m$ resolution) [81] and, for the focusing channel point of view, by using a movable high gradient Permanent Magnet Quadrupoles (PMQ) system, capable to focus the electron beam at $10\mu m$ r.m.s.. Further, a second identical focusing system has been designed to capture the beam, after the IP, and leads it through the dumper path to avoid background radiation from pipe-beam scattering (halo beam). The cavity BPM and the permanent quadrupoles focusing system are nowadays commercially available, but because of the forefront technology and the outstanding performances, the cost of these devices has a considerable impact on a STAR like machine. Then the short

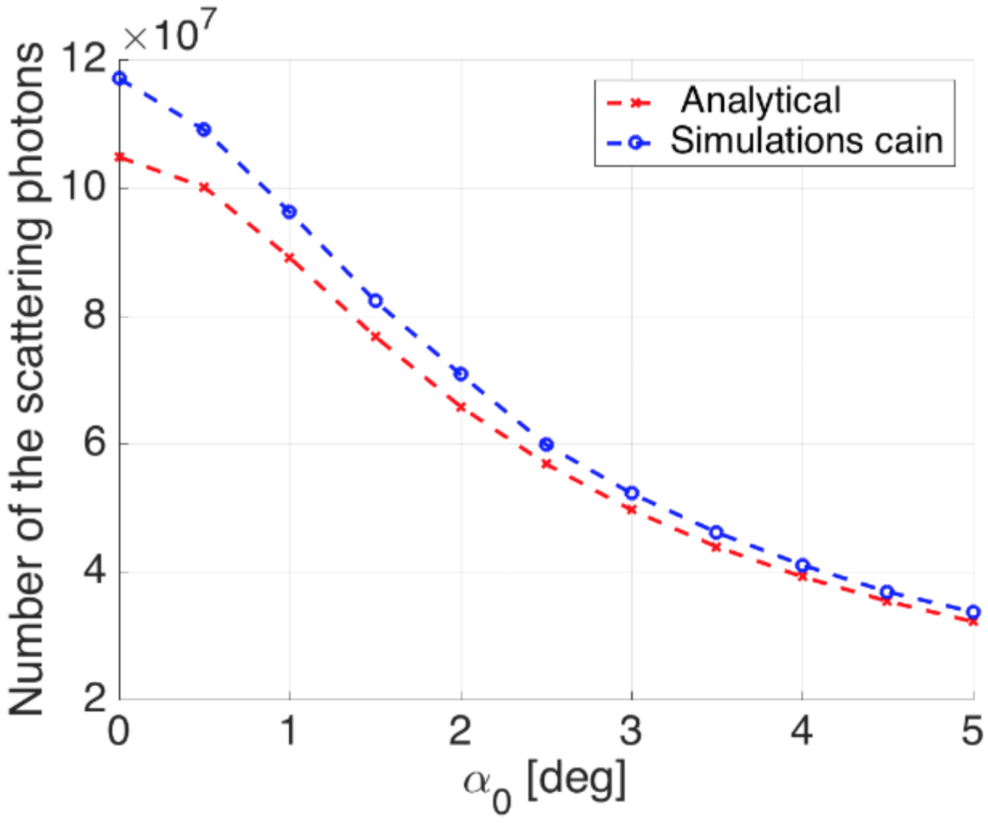

Figure 3.5. X-ray full photons flux by analytical formulas (dashed red line) and by a CAIN code simulation (dashed blue line).[74]

focusing length of the system, few centimetres, makes it necessary to embed the two PMQ focusing channels, and the laser focusing system, into a relative big vacuum chamber, together with the movements.

The second interaction scheme, that is now the frozen solution, is born together with a new injection scheme for the STAR photocathode laser. After an analysis of different laser cathode injection schemes, based on the SPARC team experience, on the solution adopted at Fermi [82] and also on the solution defined for the ELI-NP facility, we have chosen to inject the laser, on the cathode, by using an ad hoc vacuum chamber (relatively small), with a dedicated entrance laser window (Fig. 3.6). In this way the laser reaches the cathode with a small angle of 2.5°. In a similar way, the interaction laser can reach the IP entering from a small vacuum chamber, similar to the one in the gun region to let the photocathode laser hit the cathode. This solution is compatible with an angle, between the laser and the electron beam, of about 2.3°, downgrading the X-ray flux around the 50%. This drawback is acceptable if one considers all the strong benefits: the laser and electron optics are out of the vacuum chambers, which give the possibility to moved and to optimized, them, without any complications; further there are not complex laser optics (as the holed parabolic mirror) on the electron beam path.

All these are clearly great benefits not only from the laser point of view, but also for the electron beam line point of view. In order to fully optimize the final electron

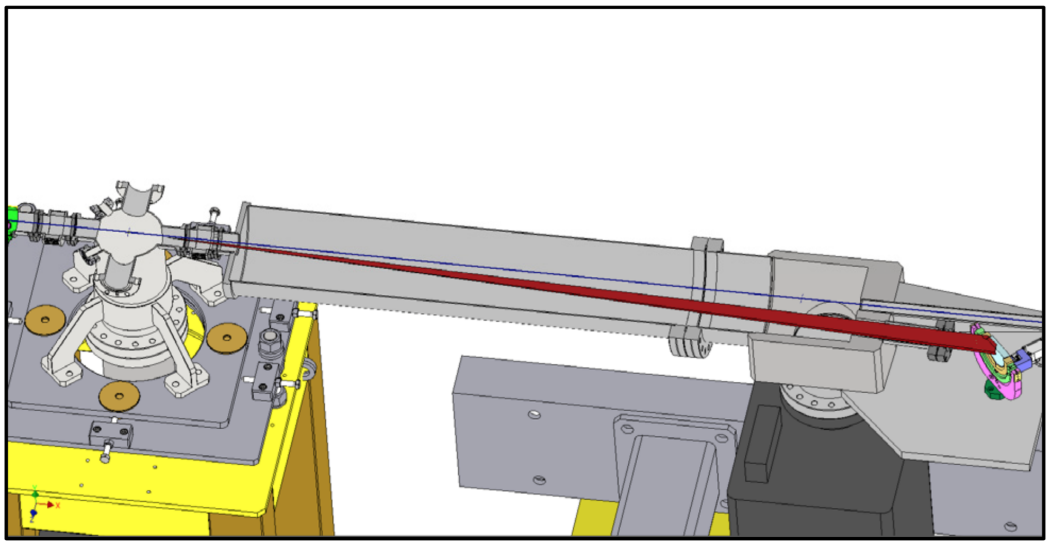

Figure 3.6. On the right the injection laser chamber, with the narrow electron beam pipe to accommodate the laser entrance windows. In red line is shown the laser envelope from the last mirror up to the IP, passing through the window. On the left the section of a typical diagnostic chamber, in this case used as the IP chamber. [74]

spot, an accurate adjustments, in term of positions of the final focus channel, which is an electromagnetic quadrupoles triplet, will be needed. The small dimensions, about 20 cm between the entrance and exit flanges, permit to move the last quadrupole, of the final focusing triplet, very close to the IP (corresponding to the middle of the chamber), shortening the triplet focal length and giving the capability to reach the same performances, or very similar ones, to the permanent quadrupoles system previously discussed.

The small bandwidth ($1nm$) and the picosecond temporal duration allow to use refractive optics to deal with the laser beam without incurring in non-linear destructive effects. In particular, the final focus on interaction point will be provided by a BK7 aspherical lens, 2J diameter aperture, with $1500mm$ of focal length, placed out of the IP chamber. The set-up optimization has been studied by performing physical optics simulations with Zemax software. In detail, taking into account diffraction effects due to any aperture (e.g. chamber optical viewport) the $F_{\#}$ has been found in order to avoid energy loss and the desired focal spot ($20\mu m$ rms). Moreover, since the laser beam goes through a window, its focusing has been evaluated as well. In Fig. 3.7 the simulated focal spot at the IP is shown, demonstrating the possibility to obtain the desired beam waist and transverse quality with this configuration.

3.4 Future outlook

The project is in an advanced phase and first electron-photon collisions are foreseen within the end of 2017. The generated X-ray beam will be provided to the UNICAL user for tomography experiment, whose setup has been already installed in the

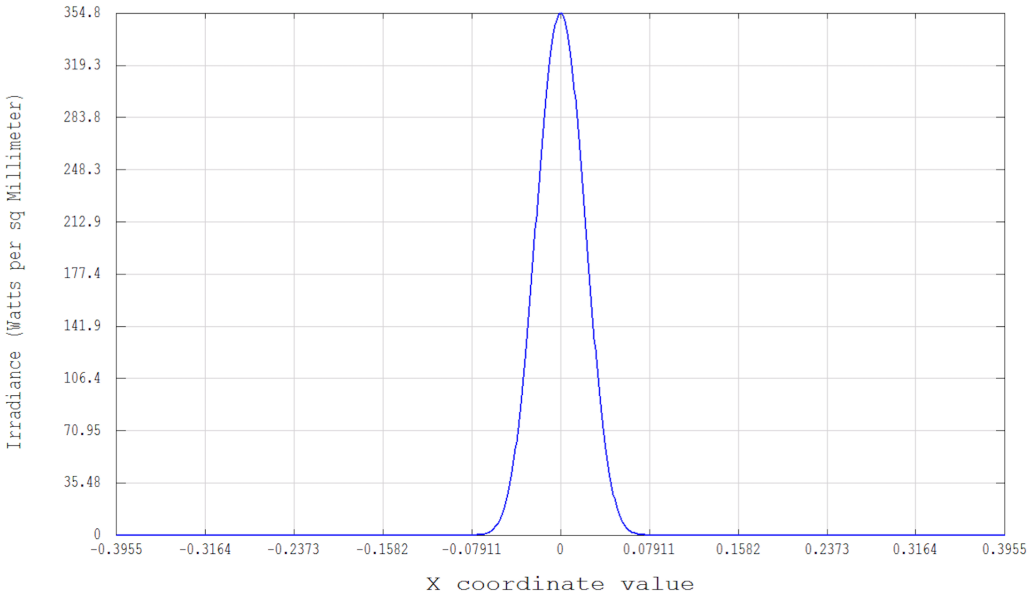

Figure 3.7. Simulation of the laser spot in the final focus at the IP.

STAR bunker.

The installation of the remaining parts is still on going. The LINAC components (gun, S-band accelarating structure, quadrupoles and electron beam pipes) have been positioned and optically aligned with high precision by the mechanical division of LNF. In particular, the gun is ready to be tested once its klystron will be commissioned by the providing company together with the INFN staff collaborating to this project.

Concerning the laser systems, although the interaction laser delivery has been postponed by Amplitude Systemes because of issues in the production line, the system providing the pulses for the electron extraction from a copper cathode has been installed and commissioned. The transverse beam shaping of the photocathode laser will be provided by a flexible optical system (see Fig. 3.4, with a dedicated diagnostics line, as described previously. The optical design has been fixed, but its experimental realization has been stopped since the laser transport line has not been positioned yet as well as for the interaction laser.

In the far future, a possible LINAC upgrade providing electrons up to $350 Mev$ is under study, in order to explore a more wide range of X-ray region.

Part II

Particle acceleration in high intensity laser - plasma interaction

Introduction

Particle accelerators have became a fundamental tool in many fields of science, from the high energy physics to medical and industrial applications. Originally, particles were accelerated in a variety of machines that relied on very large electrostatic fields. Then, with the advent of radio-frequency (RF) systems, it became possible to accelerate particles at energies beyond $10MeV$. Nevertheless, starting from the Lawrence's first cyclotron in 1932 (13 cm long machine reaching 80 keV energy), the price, complexity and size of the particle accelerators increased with the energy. Conversely, the progressively growing demand in terms of energy (and thus accelerating gradients) on a large scale required more compactness and more affordable costs in the development of accelerators. In this sense the new technique which seems to attract the main efforts is *plasma acceleration*.

Plasma-based accelerators are of great interest because they are able to sustain extremely large acceleration gradients. The accelerating gradients in conventional radio frequency linear accelerators (RF linacs) are limited to about $100MV/m$, mainly due to breakdown which occurs on the walls of the structure. Ionized plasmas, however, can provide electron plasma waves with electric fields on the order of the non-relativistic wavebreaking field [83, 84], $E_0 = cm_e\omega_p/e$, where $\omega_p = (4\pi n_0 e^2/m_e)^{1/2}$ is the plasma frequency, with n_0 the electron density, or

$$E_0[V/cm] \simeq 0.96 n_0^{1/2}[cm^{-3}].$$

Therefore, for example, $n_0 = 10^{18}cm^{-3}$ gives $E_0 \simeq 100GV/m$, that is three orders of magnitude greater than that obtained in conventional RF linacs.

This general method of using plasmas to accelerate particles has been presented firstly by John M. Dawson in 1979 [85]; it took more than a decade before experiments demonstrated electrons surfing plasma waves and gaining energy [85, 86, 87, 88]. All the different plasma acceleration schemes can be classified in two main categories, the laser and particle beam driven layouts: in the first case a laser pulse is required to form an electron plasma wave, while in the second one the electron plasma wave is formed by an electron bunch. Therefore, in the latter, plasma accelerators cannot replace existing accelerators but can only extend them to higher energies; in this sense, plasma accelerators are essentially an energy transformer: they do not provide energy because they may only transfer the energy of an existing driver to a trailing beam, that, in the best case, can double its own energy [89]. On the other hand, the recent development in the field of high power laser can give a significant boost in the realization of a reliable laser driven plasma accelerators in the next future. The possibilities offered by plasma acceleration are developing also at SPARC_LAB,

both in the laser driven and particle driven scheme [48]. In addiction, is under study also a hybrid scheme where electrons, accelerated by the RF linac, are injected in a plasma wakefield, generated by the FLAME laser, in a linear regime [90].

In this second Part, the discussion will be addressed toward the laser wakefield accelerators which exploit the high power lasers systems that are recently growing up in energy and intensity, able to reach even $10^{24} W/cm^2$. In detail, after a theoretical introduction about plasma physics and laser-based acceleration, the experimental data collected at FLAME will be presented. Moreover, the developments of a new project concerning a new LWFA scheme based on external injection of electrons, a novel transverse diagnostics tool for one shot emittance measurements will be shown. At last, the results concerning the temporal profile measurements of electric field carried by fast electrons emitted during laser-solid matter interaction, responsible of ion and proton acceleration, will be discussed.

Chapter 4

Overview on plasma wakefield acceleration

4.1 Plasma definition

Plasmas are often described as the fourth state of matter, together with gases, liquids and solids. On the other hand, a plasma can exhibit behaviour characteristic of all three of the more familiar states of matter, depending on its density and temperature. A simple definition of a plasma would be [91]: a quasi-neutral gas of charged particles showing collective behaviour. The terms of 'quasi-neutrality' and 'collectivity' require further explanation. The first of these, 'quasi-neutrality', is actually just a mathematical way of saying that even though the particles making up a plasma consist of free electrons and ions, their overall charge densities cancel each other in equilibrium. Indeed, if n_e and n_i are, respectively, the densities of electrons and ions, then inside a plasma these are locally balanced, i.e.

$$n_e = Zn_i \tag{4.1}$$

The collective behavior arises because of the long-range nature of the $1/r$ Coulomb potential: local disturbances in equilibrium can have a strong influence on remote regions of the plasma. Equivalently, macroscopic fields usually dominate over short-lived microscopic fluctuations, and a net charge imbalance $\rho = e(Zn_i - n_e)$ will immediately give rise to an electrostatic field according to Gauss's law $\nabla \times \mathbf{E} = \rho/\epsilon_0$. Likewise, the same set of charges moving with velocities v_e and v_i will give rise to a current density $J = e(Zn_i v_i - n_e v_e)$. This, in turn, induces a magnetic field according to Ampere's law, $\nabla \times \mathbf{B} = \mu_0 \mathbf{J}$. It is these internally driven electric and magnetic fields that largely determine the dynamics of the plasma, including its response to externally applied fields through particle or laser beams as, for example, in the case of plasma-based accelerator schemes.

Plasmas are created via ionization, which can occur in several ways: through collisions of fast particles with atoms, through photoionization by electromagnetic radiation or via electrical breakdown in strong electric fields. The latter two are examples of *field ionization*, which is the mechanism most relevant to the plasma accelerator context. To get some idea of when field ionization occurs, let's calculate

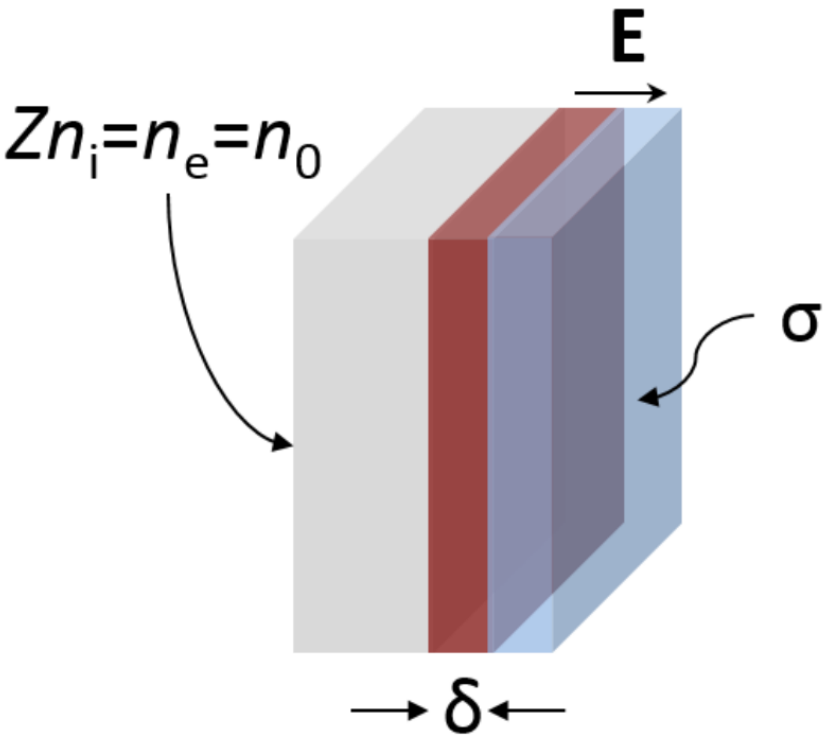

Figure 4.1. Capacitor model for electron plasma oscillations.[91]

the typical field strength required to strip electrons away from an atom. At the Bohr radius a_B, the atomic electric field strength is

$$E_a = \frac{e}{4\pi\epsilon_0 a_B^2} \simeq 5.1 \times 10^9 V/m. \tag{4.2}$$

From Eq. 4.2 follows that the threshold intensity for field ionization, *atomic intensity*, is

$$I_a = \frac{\epsilon_0 c E_a^2}{2} \simeq 3.51 \times 10^{16} W/cm^2 \tag{4.3}$$

Therefore, a laser intensity such that $I_L > I_a$ will guarantee ionization for any materials, even though it can occur below this threshold, around $10^{14} W/cm^2$, due to multiphoton effects.

4.2 Plasma oscillations

We can also ask how fast the plasma will respond to an external disturbance, which could be due to electromagnetic waves (e.g. a laser pulse) or particle beams. Consider a quasi-neutral plasma slab in which an electron layer is displaced from its initial position by a distance δ (see Fig. 4.1). This creates two 'capacitor' plates with

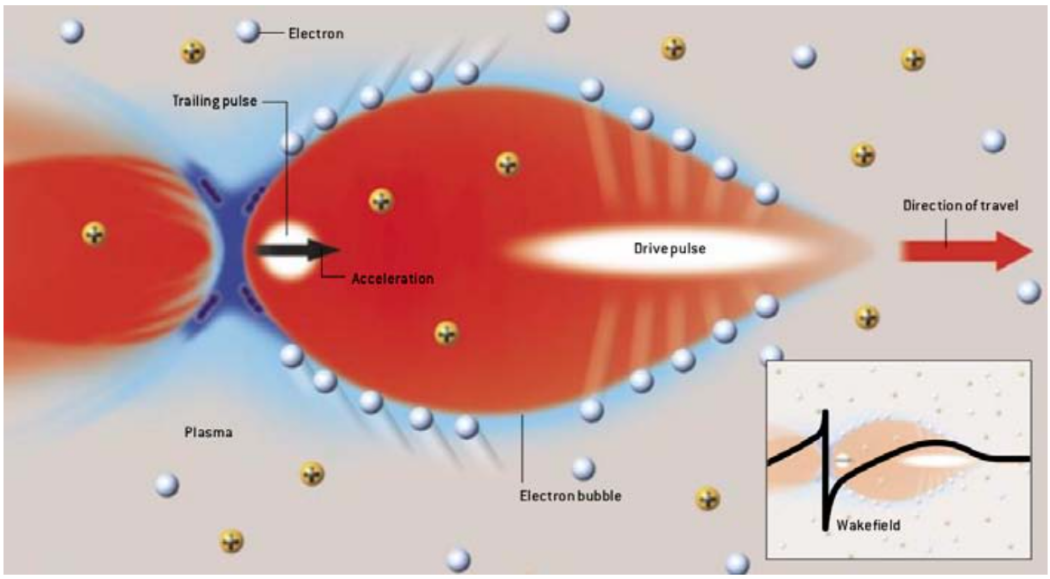

Figure 4.2. Plasma accelerator relies on a charge disturbance known as wakefield to provide the driving force. The drive pulse, a short pulse of either a laser or an electron beam, blows the electrons (blue) in an ionized gas, or plasma, outward leaving behind a region of positive charge (red). The positive charge pulls the negatively charged electrons back in behind the drive pulse, forming an electron bubble around the positive region. Along the axis of propagation, the electric field (in the right corner on the bottom) resembles a very steep ocean wave about to break. This field generates a trailing pulse of electrons caught near the rear of the bubble to feel a very strong forward acceleration.[60]

surface charge $\sigma = \pm e n_e \delta$, resulting in an electric field $E = \sigma/\epsilon_0 = (e n_e \delta)/\epsilon_0$. The electron layer is accelerated back towards the slab by this restoring force according to

$$m_e \frac{dv}{dt} = -m_e \frac{d^2\delta}{dt^2} = -eE = \frac{e^2 n_e \delta}{\epsilon_0} \Rightarrow \frac{d^2\delta}{dt^2} + \omega_p^2 \delta = 0 \tag{4.4}$$

where $\omega_p \equiv [(e^2 n_e)/(\epsilon_0 m_e)]^{1/2}$ is the electron plasma frequency. If the plasma response time is shorter than the period of a external electromagnetic field (such as a laser), then this radiation will be shielded out.

4.3 Plasma wakefield acceleration

At first sight, lasers and charged particle beams do not seem well suited for particle acceleration. They have very strong electric fields, but the fields are mostly perpendicular to the direction of propagation. To be effective, the electric field in an accelerator has to point in the direction of the travelling particle, so a longitudinal field is needed. Fortunately, when a laser or charged particle beam is sent through a plasma, interaction with the plasma can create such electric field (see Fig. 4.2).

The basic idea of a plasma wakefield accelerator is relatively straightforward and has been first proposed by Fainberg in 1956 [8]. He suggested that if relativistic

plasma waves ($v_{ph} \sim c$) were generated, electric fields generated inside the plasma could accelerate charged particles.

A plasma is globally electrically neutral, containing equal amount of negative and positive charges, respectively electrons and ions. On the other hand, a pulse from an intense laser or particle beam traveling inside creates a disturbance in the plasma, pushing the lighter electrons away from the heavier positive ions (that can be assumed fixed) creating two regions of positive and negative charge excesses (see Fig. 4.2). From that, a wave appears and starts traveling through the plasma at about the speed of light. As a consequence, a high electric field points from the positive to the negative region and accelerates any charged particles that come under its influence.

In order to estimate the plasma accelerating electric field **E** it is enough to start from the Gauss' law:

$$\nabla \cdot \mathbf{E} = \frac{\rho}{\epsilon_0} = \frac{e(n_i - n_e)}{\epsilon_0} \tag{4.5}$$

where e is the electron charge, ρ is the charge density, n_e and n_i are the electrons and ions densities, respectively. Let's assume the largest wakes, occurring for $n_e = 0$ and $n_i = n_0$, where n_0 is the plasma density: in this case, all the electrons are blown out. For a one-dimensional plane wave perturbation of the charge density, $\nabla = \hat{z}\frac{\partial}{\partial z}$ and $n_0(z)n_0 \exp(ik_p z)$, with $k_p = \omega_p/c$ and

$$\omega_p = \sqrt{\frac{e^2 n_0}{\epsilon_0 m_e}} \tag{4.6}$$

is the plasma frequency, where e, m_e and ϵ_0 are the electron charge, its rest mass and the dielectric constant, respectively. In the non-relativistic approximation, $E = E_0 \exp(ik_p z)$ and Eq.4.5 can be written as

$$|\nabla \cdot \mathbf{E}| = |-ik_p E_0| \simeq \frac{\omega_p}{c} E_0 = \frac{e}{\epsilon_0} n_0 \tag{4.7}$$

so the electric field amplitude is given by

$$E_0\Big[\frac{V}{m}\Big] = \frac{m_e c}{e}\omega_p = c\sqrt{\frac{m_e}{\epsilon_0} n_0} \simeq 96\sqrt{n_0(cm^{-3})} \tag{4.8}$$

where the ions have been assumed fixed since their plasma frequency is much lower than the electron one. The field in Eq.4.8 can be quite large, several orders of magnitude greater than the maximum accelerating gradient currently achievable by the conventional RF LINAC ($\approx 100 MV/m$). For example, assuming a plasma density equals to $10^{18} cm^{-3}$ a wave with a peak electric field of $100 GV/m$ can be generated. On the other side, the plasma wavelength is $\lambda_p = 2\pi c/\omega_p \simeq 3.3 \times 10^{10} (n_0(cm^{-3}))^{-1/2}$, that gives $\lambda_p = 33 \mu m$ for such a plasma density. Therefore, placing a bunch of electrons inside this plasma structure is much more difficult than the RF one, where the typical microwave wavelength is about $10 cm$.

Chapter 5

Laser-based plasma acceleration

Tajima and Dawson firstly in their paper [85] proposed two different laser-based schemes for particle acceleration in a plasma: a) one by using a high intense ($10^{18} W/cm^2$) laser pulse to form a plasma wave and another b) combining two different laser beams with a precise frequency difference ($\Delta\omega_L = \omega_p$). Today we call the first one Laser Wakefield Acceleration (LWFA) and the second one Beat Wave Acceleration (BWA).

By indicating with ω_L the pulse frequency of the laser propagating in a plasma, the dielectric constant of the latter is

$$\epsilon = 1 - \Big(\frac{\omega_p}{\omega_L}\Big). \tag{5.1}$$

Since $\omega_p \propto \sqrt{n_0}$, from Eq. 5.1 an under-dense plasma, where $\epsilon > 0$, is needed to be transparent to a laser beam. Therefore, in order to use it as particle accelerator, $\omega_L > \omega_p$. In detail, since the laser phase velocity reads as $v_p = c/n = c/\sqrt{\epsilon}$, Eq. 5.1 becomes:

$$\omega_L^2 = k^2 c^2 + \omega_p^2. \tag{5.2}$$

This expression, which determines the laser frequency for the medium, is called *dispersion relation*. From Eq. 5.2 is possible to determine the expression for the laser phase velocity:

$$v_p^{laser} = \frac{c}{\sqrt{1 - \frac{\omega_p^2}{\omega_L^2}}} \approx \frac{c}{2}\Big(1 + \frac{\omega_p^2}{\omega_L^2}\Big) \tag{5.3}$$

that is greater than c. On the other hand, the laser group velocity, i.e. the velocity of the laser propagating in the plasma, is:

$$v_g^{laser} = \nu_p - \lambda_L \frac{\partial \nu_p}{\partial \lambda_L} \approx \frac{c}{2}\Big(1 - \frac{\omega_p^2}{\omega_L^2}\Big) \tag{5.4}$$

which is smaller than c. Since the plasma oscillation is driven by the laser pulse, the phase velocity of the plasma wave is equal to the group velocity of the laser pulse. Therefore, from Eq. 5.4 and considering relativistic accelerated electrons, so that the speed difference between the plasma wave and the particles is $\Delta v = c - v_g^{laser}$,

the latters outruns the wave, i.e. they reach the bottom of the potential well at $\lambda_p/2$, in a distance

$$l_d = c\Delta t = \frac{\lambda_p}{2}\frac{c}{\Delta v} = \frac{\lambda_p}{2}\frac{c}{c - v_g} \approx \frac{\omega_L^2}{\omega_p^2}\lambda_p \tag{5.5}$$

that is called *dephasing length*. The resulting energy gain is $W_{max} \approx eE_0 l_d$, where E_0 is given by Eq. 4.8. For example, for $1\mu m$ laser with an intensity of $10^{18} W/cm^2$ in a $10^{18} cm^{-3}$ plasma density, the electron energy gain is equal to $1GeV$ over the distance of $1cm$.

5.1 Laser Wakefield Acceleration (LWFA)

In the laser wakefield acceleration (LWFA) [94], a short laser pulse with $\omega > \omega_p$ can excite a wake of plasma oscillations thanks to the ponderomotive force. Indeed, as the laser pulse, whose strength is given by $a_0 \equiv eE_0/(m_e\omega_0 c)$, propagates through an underdense plasma, the ponderomotive force F_p expels electrons from the region of the laser pulse and excites electron plasma waves. These waves are generated as a result of being displaced by the leading edge of the laser pulse. If the pulse length is comparable with the plasma wavelength, $c\tau_L \approx \lambda_p$, the ponderomotive force excites plasma waves with a phase velocity equals to the laser group velocity. With the development of high-brightness lasers, the LWFA idea, firstly introduced by Tajima and Dawson [85] in 1979, has been experimentally realized. Despite the successes, it is still necessary to improve beam quality, mainly in terms of energy spread and emittance.

5.1.1 Electron motion in a laser field

The motion of a single electron with charge $-e$ and mass me in the laser fields E and B is described by the Lorentz equation [92],

$$\frac{d\mathbf{p}}{dt} = -e(\mathbf{E} + \mathbf{v} \times \mathbf{B}), \tag{5.6}$$

where $\mathbf{p} = \gamma m_e \mathbf{v}$ is the electron momentum, $\gamma = (1 - \beta^2)^{-1/2}$ is the relativistic factor, with $\beta = v/c$. In the laser plane wave approximation, the electric field is given by $\mathbf{E}(z) = E_L cos(k_0 z - \omega_0 t)\mathbf{e}_x$, moving along the z axis and polarized along x. In the non-relativistic regime ($\beta << 1$), Eq. 5.6 becomes

$$\frac{d\mathbf{p}}{dt} = -e\mathbf{E} = e\frac{\partial \mathbf{A}}{\partial t}, \tag{5.7}$$

using the vector potential $\mathbf{A}(z) = A_0 sin(k_0 z - \omega_0 t)\mathbf{e}_x$, with $A_0 = E_L/\omega_0$. Therefore, an electron, initially at rest at $z = 0$, starts oscillating in the direction of the electric field with a velocity

$$\beta = -\frac{eA_0}{mc} sin(\omega_0 t) \equiv -a_0 sin(\omega_0 t) \tag{5.8}$$

From Eq. 5.8, an electron initially at rest will simply oscillate in the laser field without gaining energy.

For $a_0 > 1$, the electron velocity approaches c and the $\mathbf{v} \times \mathbf{B}$ term in Eq. 5.6 is not negligible anymore. In detail, in the frame co-moving with the laser pulse, $\mathbf{a}(z) = a_0 sin(k_0\xi)\mathbf{e}_x$, where $\xi = z - ct$ is the coordinate in this reference system. The normalized momentum of the electron can be written as

$$u_x = \gamma\beta_x = \frac{dx}{d\xi} = a_0 sin(k_0\xi),$$
$$u_z = \gamma\beta_z = \frac{dz}{d\xi} = a_0^2 sin^2(k_0\xi). \tag{5.9}$$

The electron velocity is always positive in the z direction, so that the $\mathbf{v} \times \mathbf{B}$ force pushes the electron forward. By integrating Eqs. 5.9, it is possible to calculate the electron coordinates:

$$x = \frac{a_0}{k_0} cos(k_0\xi),$$
$$z = \frac{a_0^2}{8k_0}[2k_0\xi - sin(2k_0\xi)]. \tag{5.10}$$

Eqs. 5.10 indicate that the electron not only moves forward but also oscillates at twice the laser frequency in the longitudinal z direction. The longitudinal momentum scales with the square of the laser strength as a_0^2, while the transverse one linearly depends on the laser strength by a_0 (see Fig. 5.1). Hence, for $a_0 >> 1$, the longitudinal motion of the electron dominates the transverse oscillation.

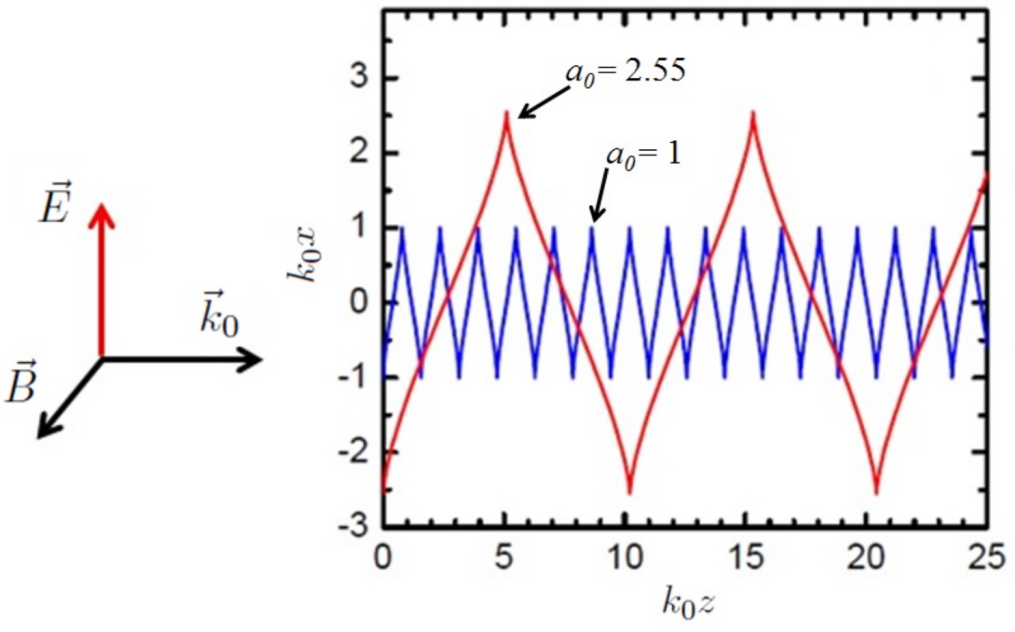

Figure 5.1. Trajectory of an electron in the laser transverse field in the laboratory frame for two values of the laser strength. The longitudinal momentum scales with the square of the laser strength as a_0^2, while the transverse one linearly depends on the laser strength by a_0. [92]

5.2 The role of ponderomotive force

In the relativistic regime, from the second term on the right of Eq. 5.6 a *ponderomotive force* appears. In detail, exploiting the rotor identity $\mathbf{a} \times (\nabla \times \mathbf{a}) = \nabla \mathbf{a}^2 - (\mathbf{a} \otimes \nabla)\mathbf{a}$, it results

$$\begin{aligned} \mathbf{F}_p &= -e\mathbf{v} \times \mathbf{B} \\ &= -\frac{e^2}{m_e c^2}\mathbf{A} \times (\nabla \times \mathbf{A}) \\ &= -m_e c^2 \mathbf{a} \times (\nabla \times \mathbf{a}) \\ &= -m_e c^2 \nabla \frac{\mathbf{a}^2}{2}. \end{aligned} \tag{5.11}$$

From Eq. 5.11, F_p is proportional to the negative gradient of $\mathbf{a}^2$ (and $\mathbf{E}^2$). Therefore, the ponderomotive force depends on the laser envelope, not on the values of the E, B fields (whose effect in a cycle is exactly equal to zero): by varying the E, B peak values, F_p does not vanish completely and a net effect is achieved. For this reason, in laser-plasma accelerators the action of the ponderomotive force leads to the excitation of a plasma wave.

The ponderomotive force can be viewed as the radiation pressure of laser intensity. This force expels charged particles out of the region of high laser intensity, and does not depend on the sign of the charged particle. Furthermore, it is inversely proportional to particle mass $F_p \propto 1/m$. Hence, under the same laser field, the acceleration exerted on a proton is only 10^{-6} times that exerted on an electron, so that ion motion can be neglected for sufficiently low laser strength.

The ponderomotive force varies as the laser energy gradient and creates a density distribution in the longitudinal and transverse directions. The associated transverse and longitudinal fields can be controlled independently by adjusting the focal spot transverse size and the pulse duration. The accelerating structure is shaped as a sine wave with wavelength λ_p, typically in the range $10 - 100\mu m$, tunable with the plasma electron density. The accelerating field is typically in the range $1 - 10 GV/m$, this value is limited to the *wavebreaking* field for a non-relativistic cold plasma of the order of $96 GV/m$ for $n_e = 10^{18} cm^{-3}$. Wavebreaking is characterized by the fact that electron oscillations become so large that the electrons can escape the collective motion. This may be at the origin of electron injection in the non-linear regime ($a_0 > 1$). On the other hand, in the linear regime ($a_0 < 1$), wavebreaking does not take place, and relativistic electrons have to be produced by an external source and injected into the linear plasma wave to be accelerated. The two different regimes are illustrated in Fig. 5.2.

In LWFA the plasma essentially receives a single kick from the short laser pulse, therefore the total amount of energy required for a full stage of the accelerator must be contained in a single pulse shorter than a plasma period. For example, for a $10^{16} cm^{-3}$ plasma density, a laser pulse shorter than $1 ps$ is needed. Moreover, the electric force of the plasma wave can never exceed the ponderomotive force of the laser. In detail, for LWFA in the nonlinear regime the maximum wakefield amplitude is

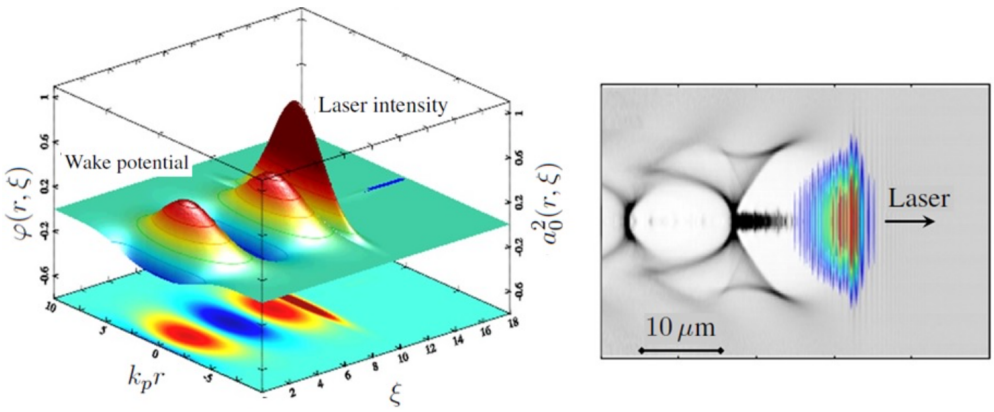

Figure 5.2. Illustration of the two regimes of the laser wakefield. Left: Excitation of a plasma wave in the linear regime; 3D view and projection in the horizontal plane of the normalized laser intensity, a_0, and wake potential, ϕ. Right: Excitation of a plasma wave in the non-linear regime; map of density in the horizontal plane (grey scale, white is zero) and superposition of laser amplitude (colour scale, red is a maximum). [92]

$$\frac{E_{max}}{E_0} = \frac{a_0^2}{\sqrt{1+a_0^2}}. \tag{5.12}$$

As an example, for a $100TW$ laser system ($5.5J$ in $55fs$) focused in $18\mu m$ the resulting accelerating gradient is about $150GV/m$, for a plasma density equals to $n_e = 10^{18}cm^{-3}$.

5.3 Electron self-injection in the blow-off regime

When an intense laser propagates through a plasma it radially expels electrons away (see Fig. 5.3) [93]. If the laser intensity is sufficiently high, the driver expels nearly all plasma electrons away from the region in which the driver propagates. Electron trajectories cross and accumulate in a high-density electron layer surrounding an electron void. On the other hand, ions remain stationary and push plasma electrons back to the axis after the driver has propagated a distance close to λ_p. At the back of the plasma wave, the shape of the thin electron layer looks like a bubble. At its back, there are electron accelerating fields which can be sufficiently strong to capture a fraction of the background plasma electrons into the bubble (self-injection). These electrons can then be focused and accelerate to high energies by the plasma bubble structure. In the laser wakefield accelerator, reaching these strongly non-linear regimes requires normalized laser vector potentials close to $a_0 \geq 2$ for spot-sizes of a few skin-depths [93].

The dynamics of an electron in the presence of a plasma wave and a laser pulse are determined by the Hamiltonian in the co-moving frame [96]:

$$H = \sqrt{\gamma^2 + p^2} - \beta_p p - \phi, \tag{5.13}$$

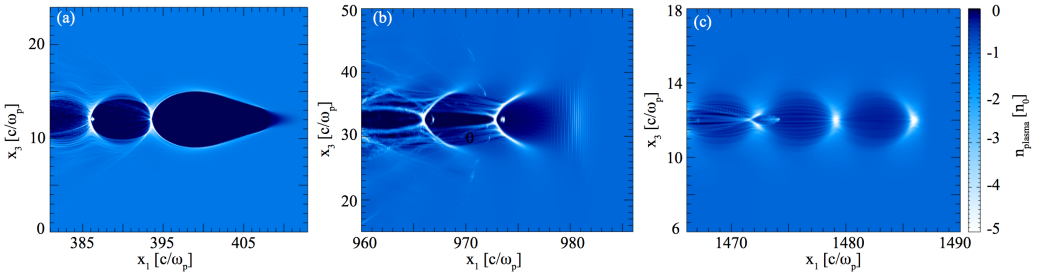

Figure 5.3. OSIRIS simulation results illustrating the generation of strongly non-linear plasma waves by different kind of drivers. The colours are proportional to the electron plasma density. The driver moves from left to right: wakefields driven by a) an ultra-relativistic particle beam driver, b) an intense laser beams and c) a positron bunch driver.[93]

where $\phi \propto \cos[k_p(z - v_p t)]$ and γ is the relativistic factor. For an electron with initial momentum p_t, Eq.**??** becomes

$$H = \sqrt{\gamma^2 + p_t^2} - \beta_p p_t - \phi = H_t. \tag{5.14}$$

Self-injection will occur when the orbit given by H_t coincides with a trapped orbit defined within the separatrix orbit (Fig. 5.13), defined by H_s when $H_t \leq H_s$. From $H_t = H_s$ it follows that the minimum initial electron momentum for trapping in the plasma wave [96] is given by:

$$p_t = \gamma_p \beta_p (\gamma_\perp - \gamma_p \phi_{min}) - \gamma_p \sqrt{(\gamma_\perp - \gamma_p \phi_{min})^2 - 1} \tag{5.15}$$

where ϕ_{min} is the minima of the plasma wave potential. The threshold momentum required for self-injection decreases for larger plasma wave amplitude and for lower plasma wave velocity [96].

5.4 Limitations to the effective acceleration length

In the laser-based schemes, there are some effects limiting the acceleration process. The first one is the *laser diffraction*. Indeed, a laser gaussian beam propagating along the z axis is chacterized by a transverse spot size

$$w(z) = w_0 \sqrt{1 + (\frac{z}{z_R})^2} \tag{5.16}$$

where $z_R = \pi w_0^2 / \lambda$ is the so-called Rayleigh length and w_0 is beam waist, i.e. the radius at $1/e^2$ of the laser intensity in the focal plane. The quantity z_R is equal to the distance at which the intensity is reduced by a factor of two, giving a measure of the longitudinal extension of the focus. For example, considering a laser with $\lambda = 1\mu m$ and $w_0 = 10\mu m$, the Rayleigh length is $z_R = 1mm$. Therefore, in order to extend it, a bigger spot would be needed, resulting in a lower intensity. Moreover, increasing the laser spot results in a weak acceleration gradient.

A second issue is represented by the *phase slippage*, due to the laser group velocity given by Eq. 5.4, that is smaller than the electron velocity $v_e \approx c$. Due to the

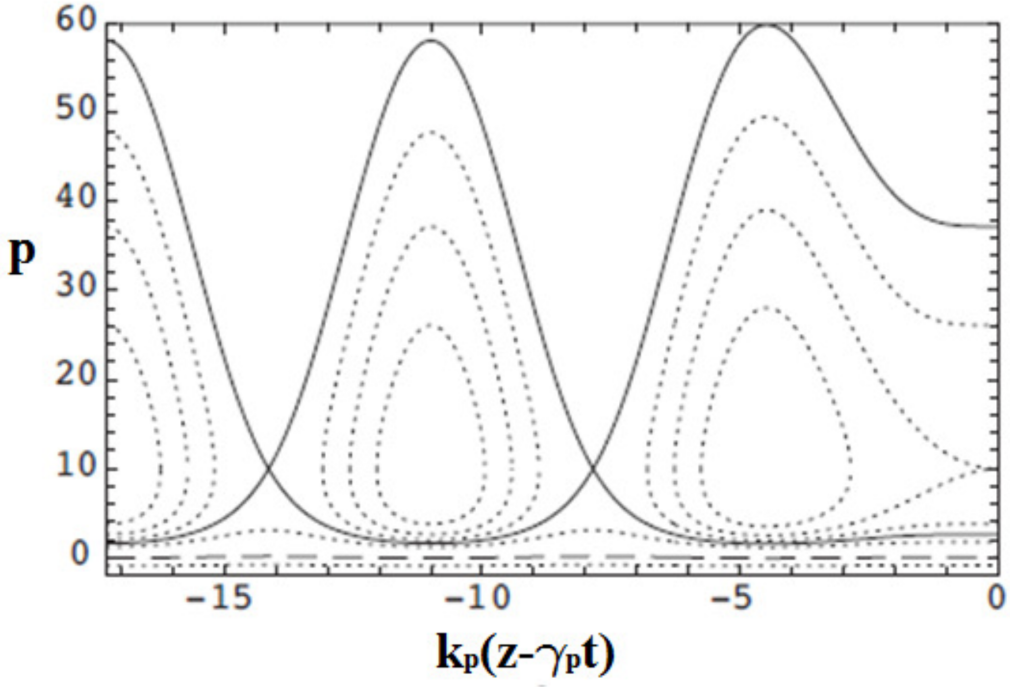

Figure 5.4. Single particle orbits in phase space for an electron in a small amplitude sinusoidal plasma wave. Dashed curve is the cold fluid orbit. Solid curve is separatrix. [96]

slippage, the electrons can reach a decelerating region in the wave; this process is called dephasing and limits the acceleration distance to the dephasing length given by [60]

$$L_d \approx \frac{\lambda_p^3}{2\lambda_L^2} \times \begin{cases} 1, & \text{if } a_0 << 1, \\ (\sqrt{2}/\pi) a_0/N_p, & \text{if } a_0 >> 1 \end{cases}$$

where N_p is the number of plasma periods behind the driver laser pulse.

The third effect is the *pump depletion length* in which the laser loses its power. One expression of this length is [60]

$$L_{pd} \approx \frac{\lambda_p^3}{\lambda_L^2} \times \begin{cases} 2/a_0^2, & \text{if } a_0 << 1, \\ (\sqrt{2}/\pi) a_0, & \text{if } a_0 >> 1. \end{cases}$$

The previous three characteristic lengths fix the maximum achievable acceleration distance. As an example, consider the linear regime with the parameters $a_0 = 0.3$, $\lambda = 0.8\mu m$ and $\lambda_p = 33\mu m$ ($P = 3.3TW$ and $n_0 = 10^{18} cm^{-3}$). The relevant propagation lengths are $z_R = 0.43cm$, $L_d \approx 2.8cm$ and $L_{pd} \approx 1.2m$, i.e. $z_R << L_d << L_{pd}$ so during the years major effort has been aimed at exceeding the limit of the diffraction.

A possibility to overcome the limit due to the Rayleigh length can be found in the *relativistic self-focusing*. Indeed, at relativistic velocities the plasma wave is nonlinear and its frequency becomes dependent on its amplitude through the relativistic mass increase

$$\omega_p^2 \to \omega_p^2/\gamma \tag{5.17}$$

where γ is the relativistic factor. This happens because in the relativistic regime the mass of the electron is γm_e. On the other hand, the plasma refractive index is given by

$$\eta = \sqrt{1 - (\frac{\omega_p}{\omega_L})^2} \tag{5.18}$$

thus in a region of lower ω_p the refractive index is higher and vice versa. In this way, the plasma channel acts as a lens, focusing the laser beam and balancing the natural divergence. In detail, if the power of the laser pulse is greater than the *critical power*, $P \simeq P_c[GW] = 17(\frac{\omega_L}{\omega_p})^2$, relativistic self-focusing occurs. For example, for $\lambda_L = 0.8\mu m$ and $n_e = 7 \times 10^{18} cm^{-3}$, $P_c = 4.25TW$.

Chapter 6

LWFA experiments at FLAME Facility

Introduction

The FLAME Facility consists in a two levels building: the ground floor is devoted to host the laser clean room, the control room and all the power supplies; at the underground level there is the FLAME bunker (see Fig. 6.1). Here, the

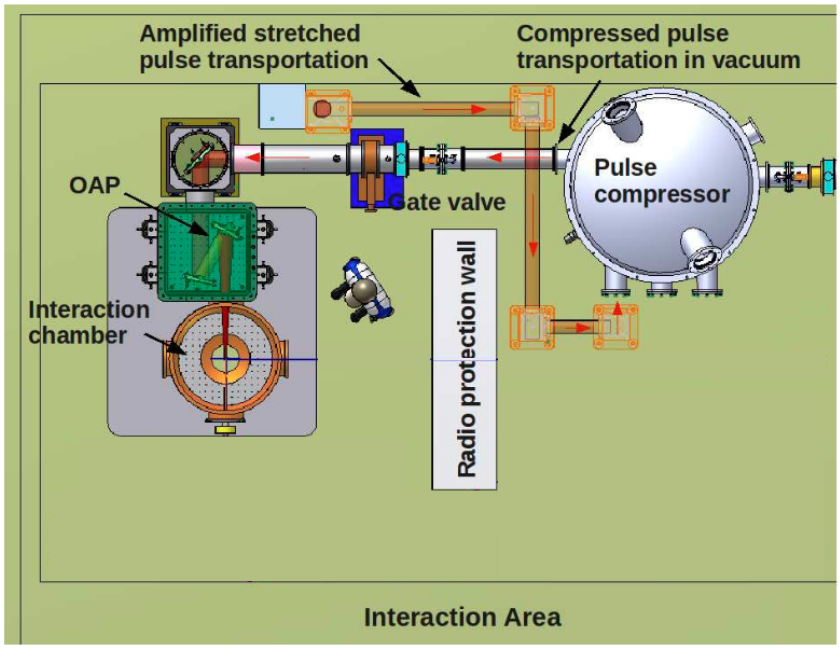

Figure 6.1. Top view of the underground FLAME bunker. Laser coming from the clean room, located at the ground floor, goes into the optical compressor chamber for temporal shortening after the CPA chain. The pulse compressed reaches the OAP mirror and it is focused in the middle of interaction chamber on a specific target (gas or solid).

optical compressor is installed in a vacuum chamber, in order to reach fs-scale laser pulse duration, exploiting the wide spectrum coming from the Ti:Sa-based CPA

amplification chain. After that, the beam goes to the FLAME target area through a dedicated laser transport line up to the off axis parabolic (OAP) mirror (focal length $f = 1m$), able to provide a focal spot with a diameter of $20\mu m$ at $1/e^2$. The FLAME target area (see Fig. 6.2) is employed for studies on laser-plasma interactions, occurring in a dedicated chamber after the OAP mirror such that the beam is focused in the middle.

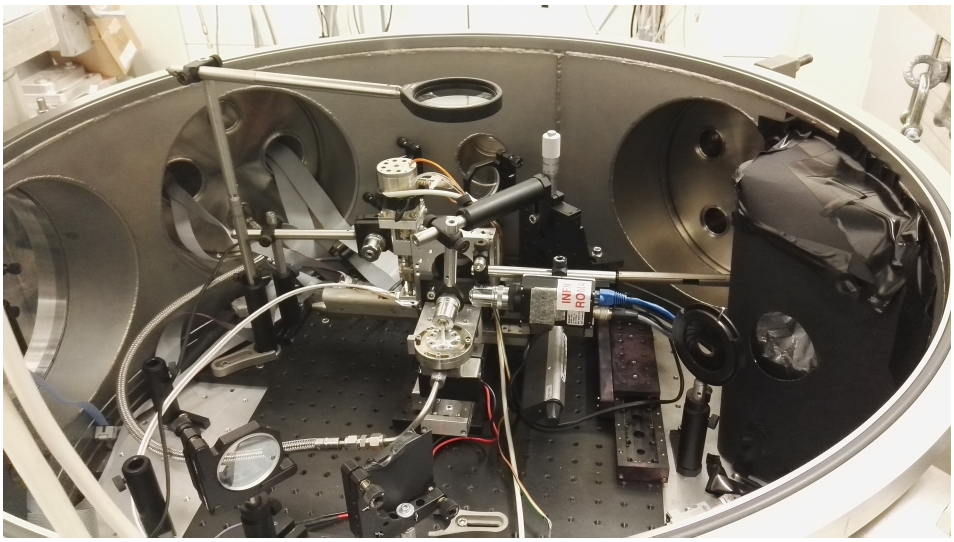

Figure 6.2. A real picture showing a part of the experimental setup.

This chapter concerns the experiments performed at SPARC_LAB by means of Sub-PW FLAME laser system to accelerate electron exploiting the LWFA process (laser-gas interaction) and study the ion acceleration mechanism occurring during the interaction with solid targets. Moreover, a new diagnostics tool for one shot emittance measurements, useful for plasma accelerated electron beams, will be presented.

6.1 Experimental methods

In Fig. 6.3 a sketch of the experimental setup layout is shown. The FLAME main laser, coming from the right, is focused by a $F_{\#} = 10$ OAP mirror on the top of the gas-jet with a beam waist $w_0 = 10\mu m$. From it, gas is expelled with variable pressure $(0 - 50bar)$ by means of a specific knob placed on the gas bottle. The non-linear plasma wakefield, stimulated by the high intense $(1 \times 10^{19} W/cm^2)$ laser beam, creates an electron bunch with the same propagation direction of the laser. After shielding the rest of experimental chamber from the laser beam by reflecting it with a thin aluminum foil and blocking it on an absorber, a series of electron beam diagnostics have been installed. Moreover, a Mach-Zehnder interferometer has been used in order to measure the plasma density as well as an imaging system looking at the 90° Thomson scattering to check the quality of plasma channel.

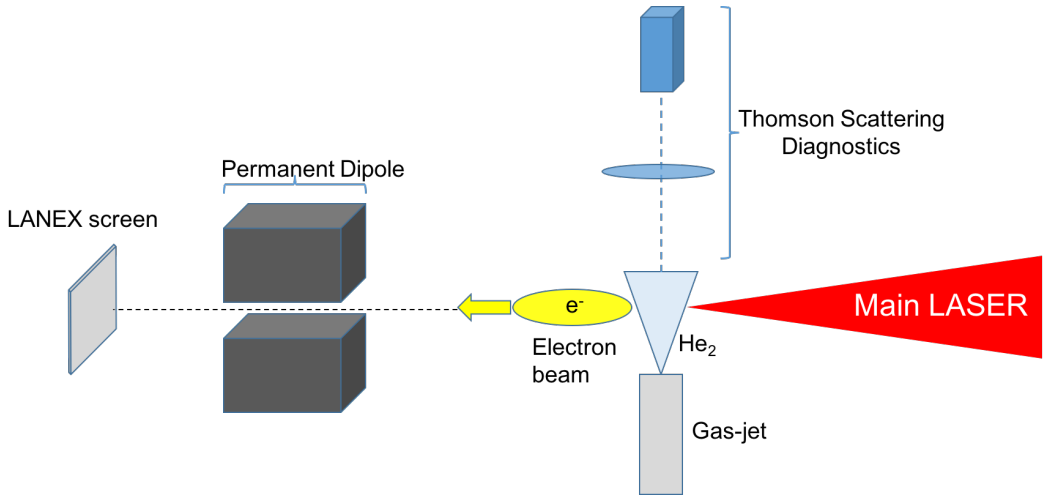

Figure 6.3. Sketch of experimental setup. The FLAME main laser is focused by a $F_{\#} = 10$ OAP mirror with a beam waist $w_0 = 10\mu m$ in correspondence of the gas-jet position. This latter can expel He gas with variable pressure $(0-50bar)$ by means of a specific knob placed on the gas bottle. The electron beam, accelerated by the non-linear plasma wave, follows the laser propagation direction and can be detected by a magnetic spectrometer or by a LANEX screen to measure the energy and the transverse spot size, respectively. In order to check the electron plasma density, a Mach-Zehnder interferometer has been used (not in figure). In additction, an imaging system collecting the Thomson scattering at 90° has been utilized to check the plasma channel length.

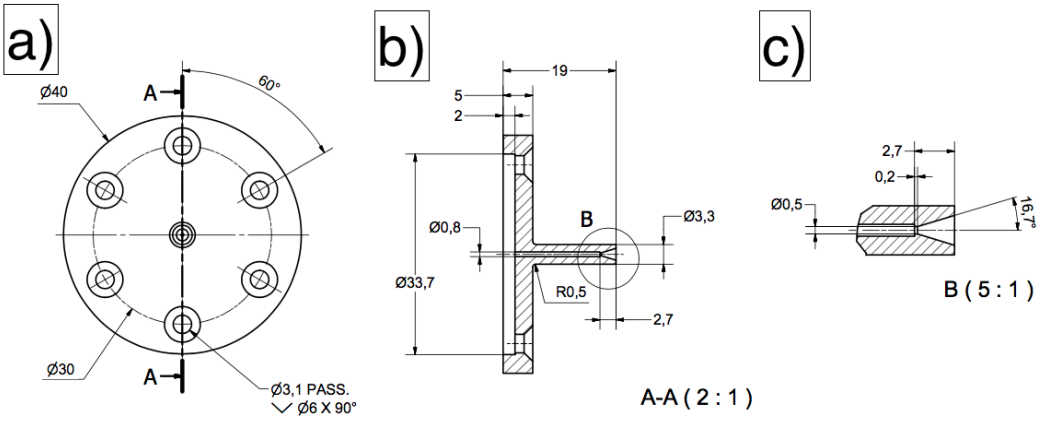

Figure 6.4. a) Top-view, b) side-view of the gas-jet nozzle and c) detail of gas-jet. Length units are in mm.

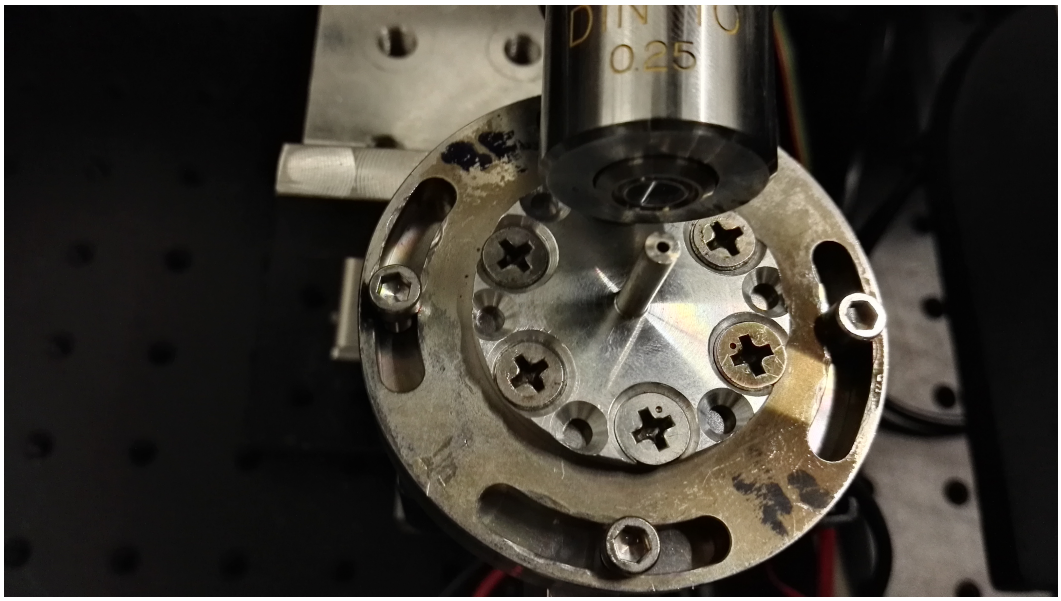

Figure 6.5. A real picture of the gas-jet taken from the experimental setup.

6.1.1 Gas-jet design

The geometry of the gas jet nozzle is shown in fig. 6.4. It has been designed in order to provide a supersonic gas profile for a sharp boundary with the vacuum. Indeed, a column of gas which has turbulence inside is generally not ideal for acceleration because it creates strong plasma density variation along the laser path [95]. The laser beam is focused at the beginning of the gas column for self-ionisation and plasma wave formation. In Fig. 6.5 a picture of the gas-jet taken from the experimental setup is shown.

In order to minimize and optimize the flow of gas onto the vacuum ($10^{-6} mbar$), a solenoid valve (normally closed) is used: it is opened just before the laser arrival, and the aperture time is remotely tunable. Mounted on the top of the solenoid valve is the a gas jet nozzle, specially designed to have a sharp edge of the gas column. The opening angle of the nozzle defines the maximum acceleration length achievable, depending on the distance between the gas jet and the laser beam.

6.1.2 Plasma density interferometric measurements

For measuring electron densities of a laser-created plasma using an interferometric method, the plasma formed should be placed in one of the arms of the interferometer. The plasma may consist of ions, atoms and molecules in addition to free electrons. Therefore, the probe laser wavelength should be well away from any absorption resonances so that contributions to the refractive index from bound electrons is negligible compared to that of free electrons in the plasma. In this condition, the refractive index can be expressed as [99]

$$\mu = \sqrt{1 - \frac{n_e}{n_c}} \tag{6.1}$$

where n_e is the electron number density and n_c is the critical electron density for the specific probe laser wavelength λ ($n_c = 10^{21}\lambda^{-2}cm^{-3}$, where λ is in microns). The probe laser radiation penetrates the plasma only to the point where the electron density reaches the critical density, at which point the reflection occurs. The ratio of the fringe shift to the fringe spacing (Δ) can be related to the line integral of electron density along the probe beam [107] path by

$$\Delta = (2\lambda n_c)^{-1} \int n_e(l)dl \tag{6.2}$$

where l is the optical path length through the plume. A 2-D mapping of the density can be obtained by using the Abel inversion technique [99].

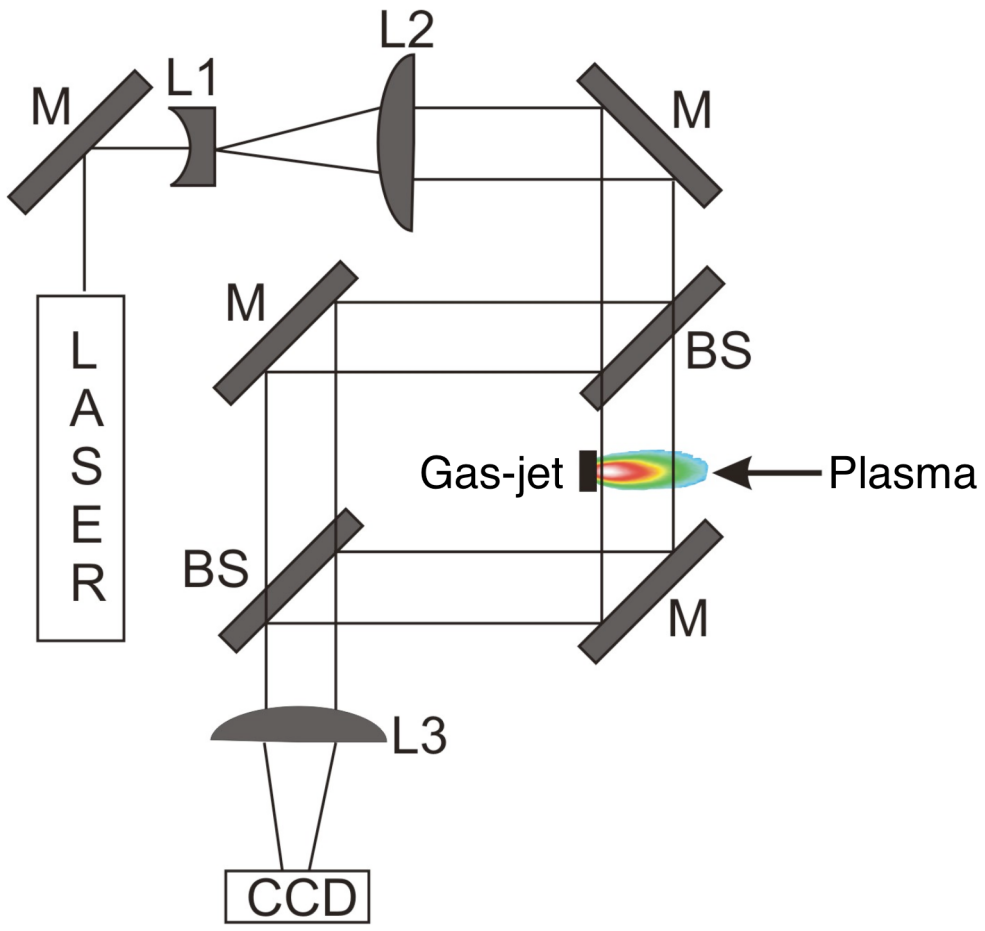

Figure 6.6. Mach-Zehnder interferometer typical set-up for plasma density measurement. **BS**: Beam Splitter, **M**: Mirror, **L**: Lens.[107]

For our experiment, a Mach-Zehnder interferometer has been built as plasma density diagnostics tool. A probe laser beam, splitting a small fraction of the main pulse before compression, has been used. In the Mach-Zehnder interferometer the probe beams follow different pathways before interfering. This simplifies the interpretation of the observed fringes by passing light through the test area only

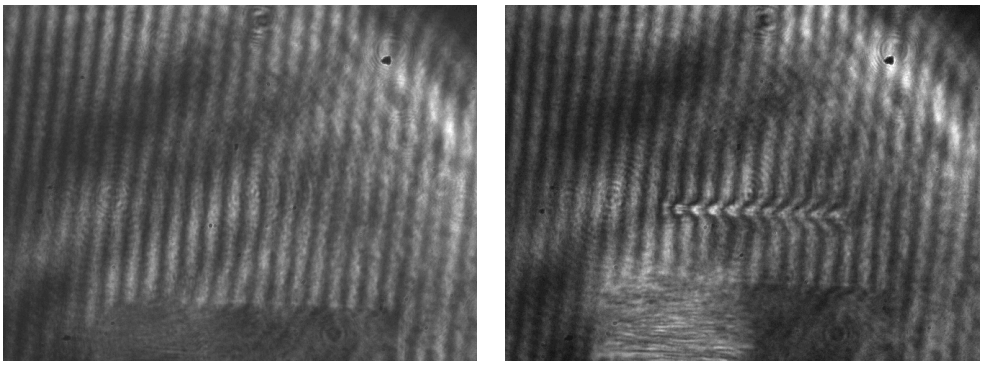

(a) *Interferogram in absence of plasma.* **(b)** *Interferogram in presence of plasma.*

Figure 6.7. Typical measurements with our Mach-Zehnder interferometer.

once. A typical Mach-Zehnder interferometer set-up for plasma density measurement is given in Fig. 6.6. In Fig. 6.7 a typical measurement is reported. Moreover, a shadowgram can be recorded instead of an interferogram, when the reference path of the interferometer is blocked.

6.1.3 Thomson scattering for plasma channel imaging

90° Thomson scattering is used to image the plasma channel. The images has been recorded using Thomson scattering of the source, due to electron-photon collisions during the laser-plasma interaction. Thomson scattering diagnostic provides a useful support for monitoring the laser pulse propagation during its interaction with the gas medium. It gives an on-line information of the interaction length between the laser pulse and plasma and thus can be used to optimize the best conditions for electron acceleration.

The imaging system in our setup is constituted by two optical elements, a $35mm$ objective and a $200mm$ focal length lens, in order to get a magnified image of the laser-plasma interaction region on the CCD camera (Basler scA1600-14gc). In detail, each pixel corresponds to $47\mu m$, calibrated from a typical picture as Fig. 6.8. Typical values of the plasma channel from our measurements are about $2.6mm$, corresponding to the acceleration length.

6.1.4 Electron beam profile measurement

To measure the beam profile, a Lanex screen has been used. A Lanex screen is a scintillator screen which employs a $Gd_2O_2S : Tb$ inorganic scintillator with high conversion efficiency of both X-ray and electron detection [97]. It has been reported to give similar energy absorption per electron for electron energies from 10 MeV to 500 MeV so it is a good candidate for LWFA electron imaging [98]. Lanex emits in the blue-green spectral region with a strong component at 548 nm, which is a good wavelength for imaging with standard silicon CCD cameras. The knowledge of the beam profile is very important because it can give a lot of information about the beam quality, mainly regarding its divergence. In our case, a Lanex foil has

Figure 6.8. Typical picture taken from 90° our Thomson scattering diagnostics. By dividing the length of gas-jet diameter by the number of pixels constituting it in the image, it is possible to retrieve the CCD camera calibration. The plasma channel created by the laser propagation in the gas is visible as well.

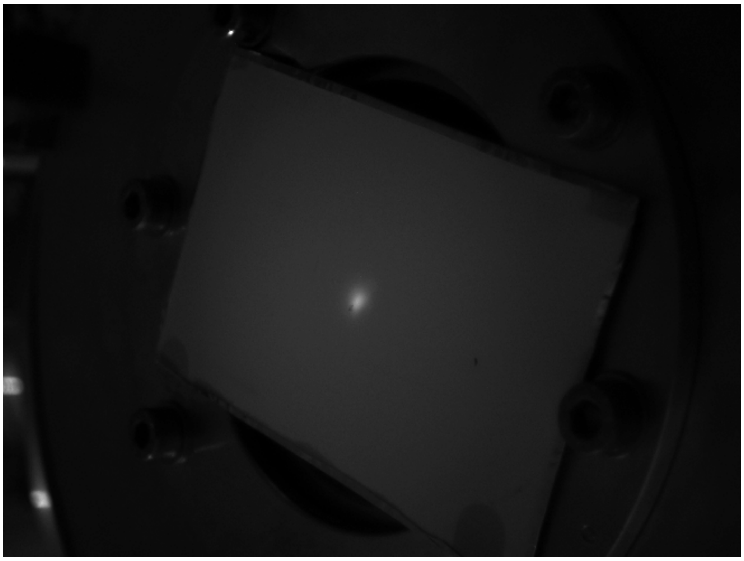

Figure 6.9. Example of beam profile measurement with our setup.

been installed at 45° with respect to the electron direction, placed before the energy spectrometer and imaged by a CCD camera (Basler scA640-70gm) looking at the screen directly. In Fig. 6.9 a typical electron beam profile is shown.

6.1.5 Electron energy measurement

The energy spectrum of the electrons has been measured using a magnetic spectrometer, composed of a $1T$ permanent dipole $10cm$ long and a LANEX screen placed at 60° with respect to the propagation direction of the beam. The setup has

been optimized by means of simulations made with General Particle Tracer (GPT) software shown in Fig. 6.10. This setup aims to obtain a better resolution for low energy ($< 300MeV$) electrons, with a $\Delta E \approx 0.5MeV$.

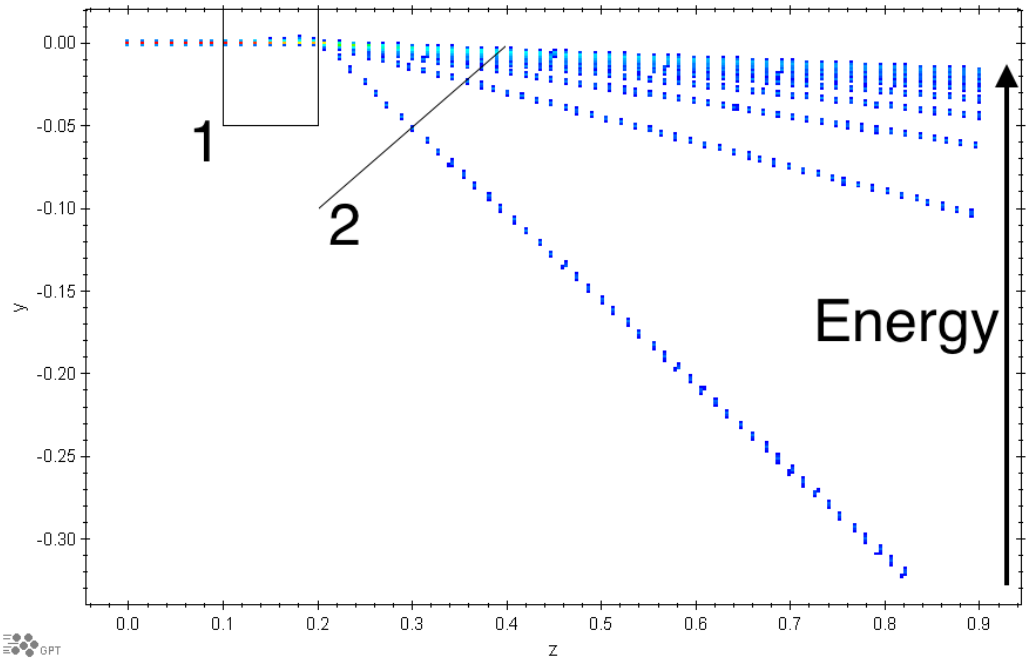

Figure 6.10. General Particle Tracer (GPT) simulations for electron energy spectrometer design. The electrons with lower energy are much more bent than the more energetic ones. In the plot are shown 1) the $1T$ permanent dipole and 2) the LANEX screen intercepting the bent electrons. Both axis units are in m.

In order to analyze the measurements performed with such a system, some calculations have been done to find the correspondence between electron energy and deflection from the axis. The path of the electrons within the magnetic field B follows this equation

$$evB = \frac{\gamma m_e v^2}{R}. \tag{6.3}$$

In particular, $R = p/(eB)$ represents the radius of the the Larmor orbit for an electron with momentum p. By a simple geometrical construction, the electron position on the diagnostics screen can be calculated (see Fig. 6.11).

In order to find the right correlation between electron energy and screen position, dedicated GPT simulations have been performed see Fig. 6.12). Finally, the screen position has been calibrated with respect to the CCD camera pixel.

In Fig. 6.13 a typical energy measurement is shown.

6.1.6 Electron charge measurement

Measurement of the absolute beam charge has been conducted using Fuji BAS imaging plates. An imaging plate (IP) [96] is a two-dimensional detector of ionising radiation (X-rays, energetic particles etc) consisting of a thin layer of barium fluorohalogenite doped with europium 2+ ions on a polyester substrate. Electrons excited

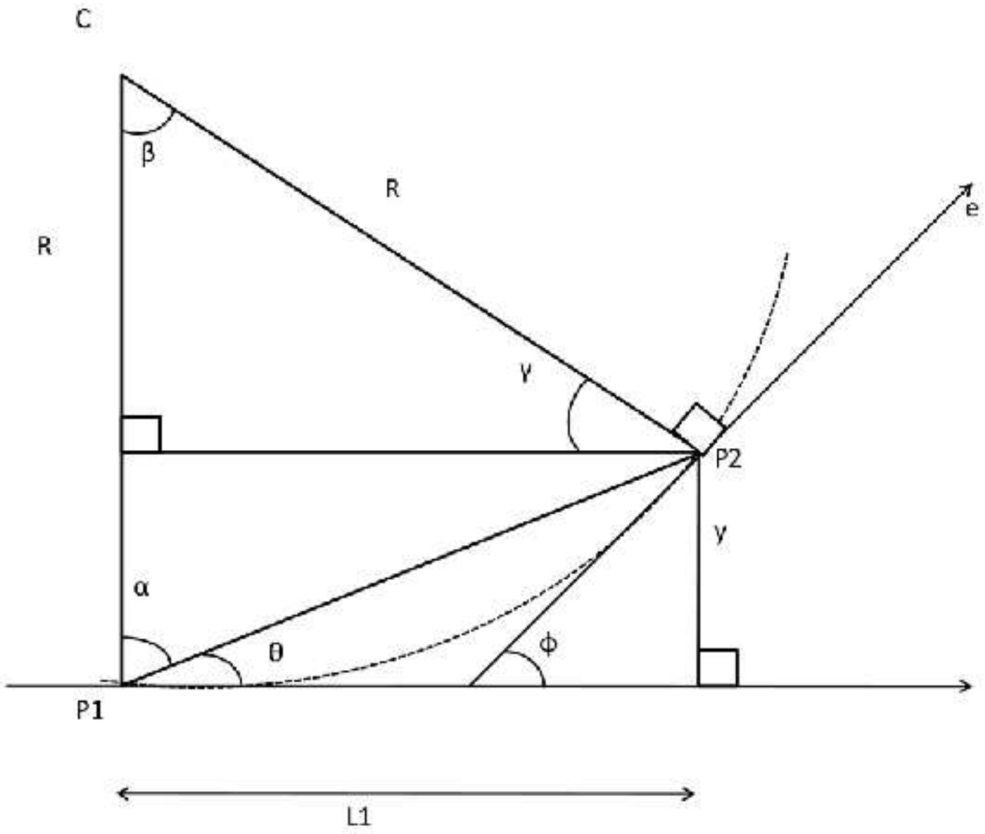

Figure 6.11. Trajectory of an electron passing through a magnetic spectrograph. The dotted curve represents the Larmor orbit of the electron in the magnetic field. It can be seen that the position of the electron on the screen placed at a distance d from the dipole is given by $y = 2R\sin^2(\beta/2) + d\sin\beta/\cos\beta$, where $\sin\beta = L_1/R$.

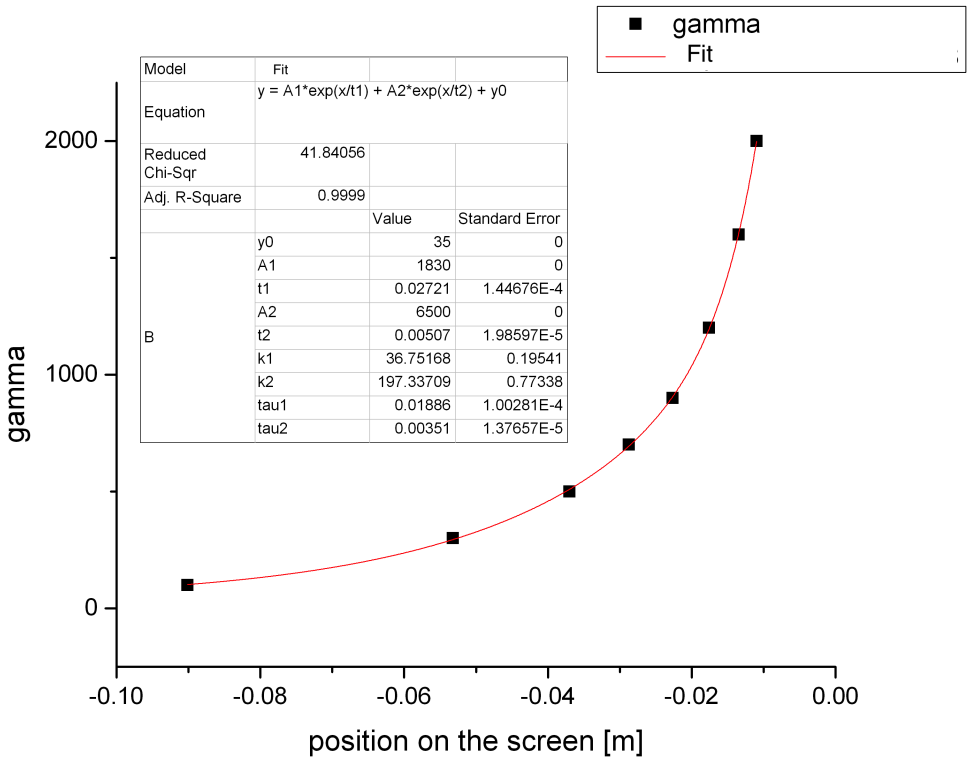

Figure 6.12. Calibration of electron energy as a function of the LANEX screen of the energy spectrometer. Simulations performed by means of GPT software.

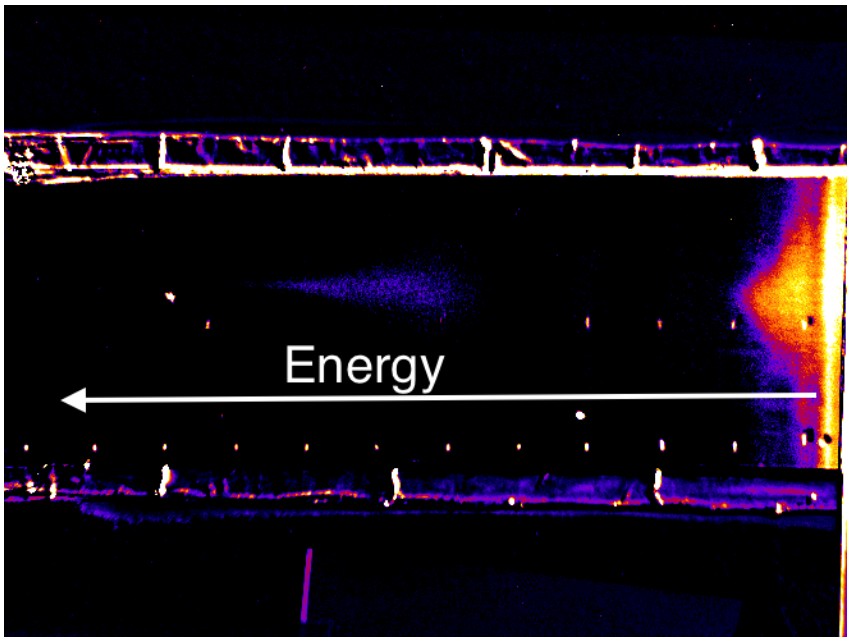

Figure 6.13. Typical measurement of electron energy spectrum from our setup. In the middle of LANEX screen the most energetic electrons are located ($\approx 240 MeV$ central energy).

from EU 2+ ions by incident ionising radiation are trapped in a metastable state and the trapped states can decay if de-excited by light at 632.8 nm, which is how IPs are read out in a scanning system to extract their stored data. As the metastable state decays, blue light at 400 nm is emitted in a process known as photo-stimulated luminescence (PSL). The number of these emitted photons in the read-out process is proportional to the total absorbed radiation energy. The measured pixel data by means of IP scanner have to be converted from this value, or gray level (GL), to a linear PSL scale [100]:

$$PSL(GL) = 0.0004 \times GL - 0.0024. \tag{6.4}$$

The IP used during the experiment was covered with an aluminium foil to ensure that it was not exposed to laser light. After irradiation the stored information was read out with a reader/scanner, giving the two dimensional scanned map. An example of electron charge measurement is provided in Fig. 6.14. Typically, for our setup, a charge of $10pC$ of electron charge has been measured.

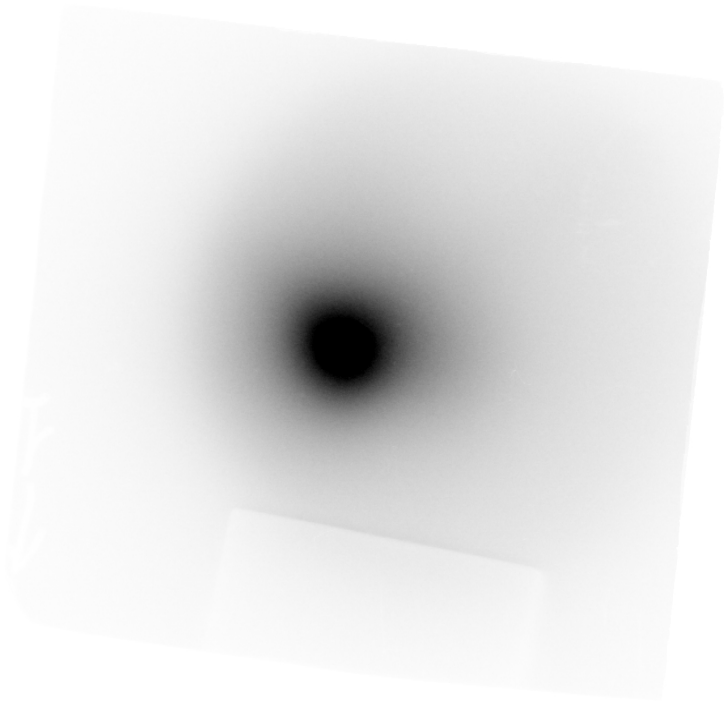

Figure 6.14. Typical electron charge measurement by means of imaging plates in our setup. From Eq. 6.4 is possible to correlate the gray level to the charge value.

6.2 Experimental results

In this section, the main experimental results, concerning the laser parameters and the electron properties, will be shown. In Tab. 6.1 the main laser parameters have been reported.

In Fig. 6.15 a typical FLAME focal spot is shown. A Bassler Scout scA640-70gm CCD camera with a 20X DIN Achromactic Finite Intl Standard Objective

Energy (on focus)	J	1
Spectral width (FWHM)	nm	60
Focal spot (diameter $1/e^2$)	μm	20
Pulse temporal length (FWHM)	fs	40

Table 6.1. FLAME laser parameters for LWFA experiment.

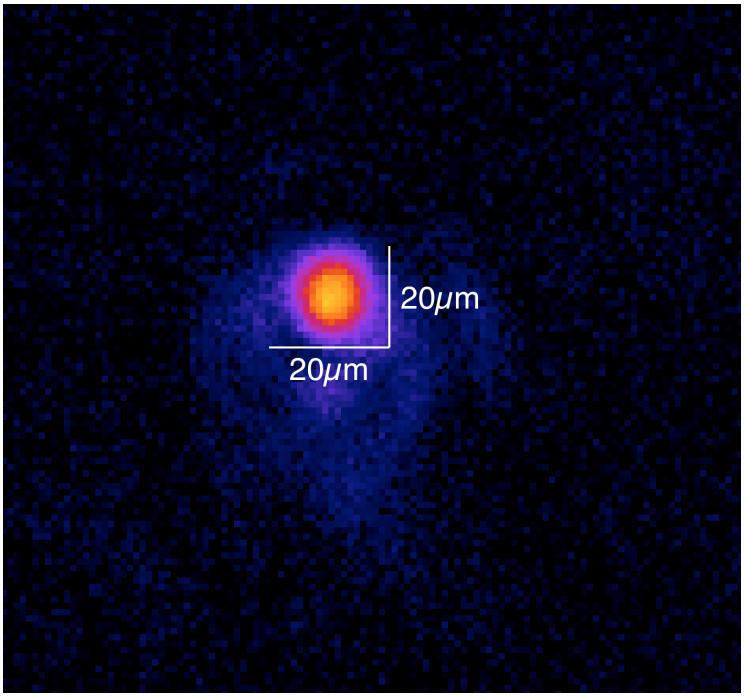

Figure 6.15. Laser focal spot measured in vacuum at the gas-jet position with a Bassler Scout scA640-70gm CCD camera with a microscope objective. The diameter at $1/e^2$ is $20\mu m$. The beam has been opportunely attenuated to avoid any CCD damage.

microscope objective has been used in order to get a high resolution ($1.1\mu m/pixel$). A fine alignment of optical compressor gratings has been made in order to remove any residual spatial chirp. In this sense, a useful simulation with Zemax has been performed aiming to understand which grating was misaligned. Moreover, also the off axis parabolic mirror alignment has been checked to get the diffraction limit spot size ($20\mu m$ $1/e^2$ diameter), studying the optical geometry with Zemax as well.

In order to reach a relativistic plasma wakefield regime ($a_0 > 1$), also the laser temporal length plays an important role. Indeed, a value less than $100fs$ is needed in order to stimulate the blow-off regime and exploit the relativistic self-focusing to keep the laser focused inside the plasma channel as much as possible. In particular, in our case, the longitudinal laser profile is $40fs$ FWHM (see Fig. 6.16). By using an energy of $1J$ on focus, we reach a peak power of $25TW$ and an intensity of $1.6 \times 10^{19} W/cm^2$. The reduction in terms of peak power with respect of nominal parameters is due to a temporary fault in the last amplifier, working with only 4 pump lasers. Moreover, only the 50% of energy was in the first lobe of the focal spot.

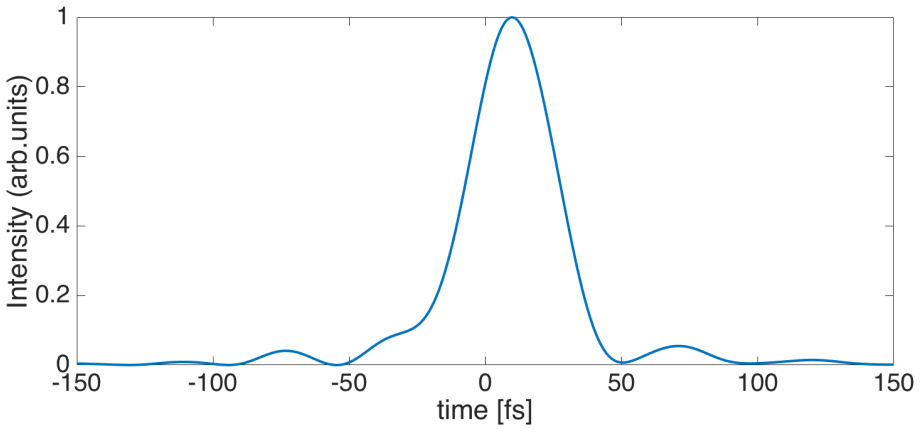

Figure 6.16. Laser temporal length measurement by means of a APE SPIDER [101]. The FWHM is equal to $40fs$.

As starting point, after setup parameters optimization, we measured the electron plasma density due to laser ionization by means of a Mach-Zehnder interferometer. In Fig. 6.17 an experimental result is shown, together with the data analysis made with a specific tool developed in Matlab code [102]. The value of $1 \times 10^{19} cm^{-3}$ has been measured. In this way, the plasma wavelength and the dephasing length has been found: $\lambda_p = 10.6\mu m$ and $l_d = 1.9mm$, with a He gas pressure of $20bar$ (measured at gas bottle exit).

In Fig. 6.18 some measurements concerning electron energy measurements are shown. The results, summarized in Tab. 6.2, seem to be very reproducible without changing the experimental parameters. Nevertheless, the energy spread seem to be quite high: one of the problem could be the fact that the dephasing length is shorter than the acceleration length, estimated around $2.6mm$ from both the interferometric measurements and the Thomson diagnostics. Indeed, the slippage between the electron bunch and the accelerating plasma wave is such that the first is not extracted on the crest of the wave but after. Therefore, since the different part of the beam experiences different accelerating field, the energy spread is higher.

The results that have been given concern only the high energy part of the whole spectrum. Indeed, most electrons have a lower energy ($< 50MeV$), as it has been seen in all the LWFA experiments. At the moment, the experimental setup is not equipped yet with an energy selector in order to keep only the energetic core of the total electron charge exiting from the plasma channel.

In Fig. 6.19 are presented some measurements regarding the transverse spatial profile of electron beams accelerated through LWFA at FLAME. The measurements have been taken by means of a LANEX screen, placed outside the experimental chamber, and a CCD camera Basler Scout scA640-70gm with a $35mm$ objective. It has to be noticed that the measure is affected by the presence of a 1" thick glass optical window, installed at the end of the chamber, where the screen is placed.

In Tab. 6.3 some results of spot size dimension measurements are shown. The data have been compared with a gaussian distribution whose σ has been retrived in the range $1 - 3mm$. Since the distance between the source and the screen was

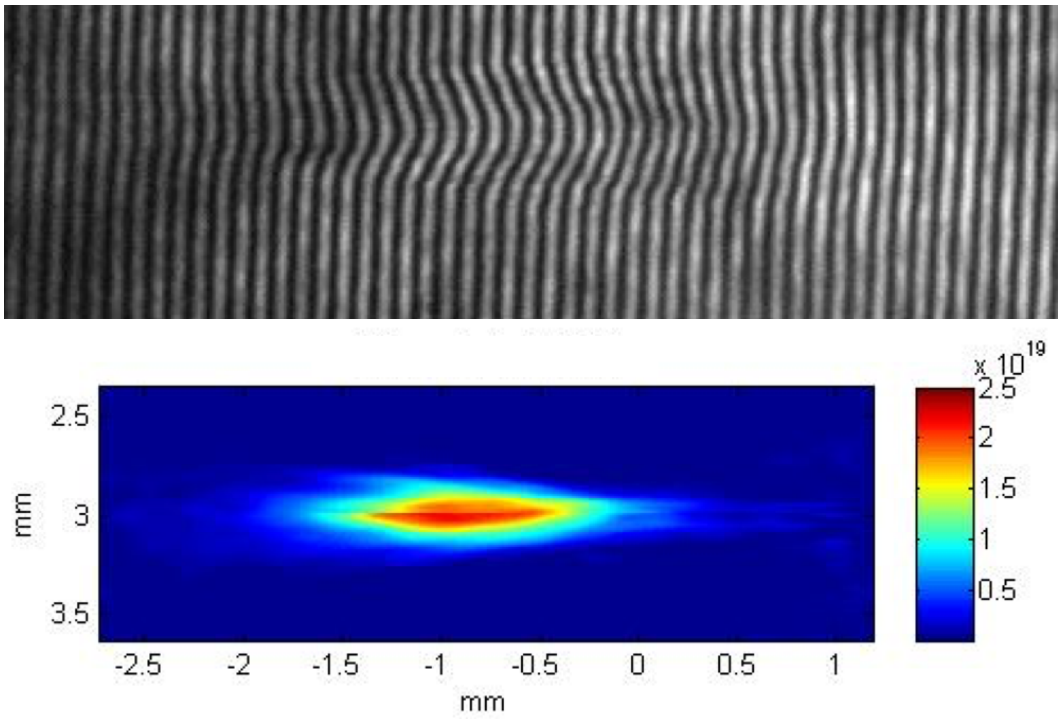

Figure 6.17. Interferometry result for plasma density measurements. In working conditions, a value of $n_0 \approx 1 \times 10^{19} cm^{-3}$ for the electron plasma density has been found.

	Energy [MeV]	Energy Spread
1	187	17%
2	185	18%
3	192	25%
4	196	13%
5	214	12%
6	194	22%

Table 6.2. Electron energy measurement results related to Fig. 6.18.

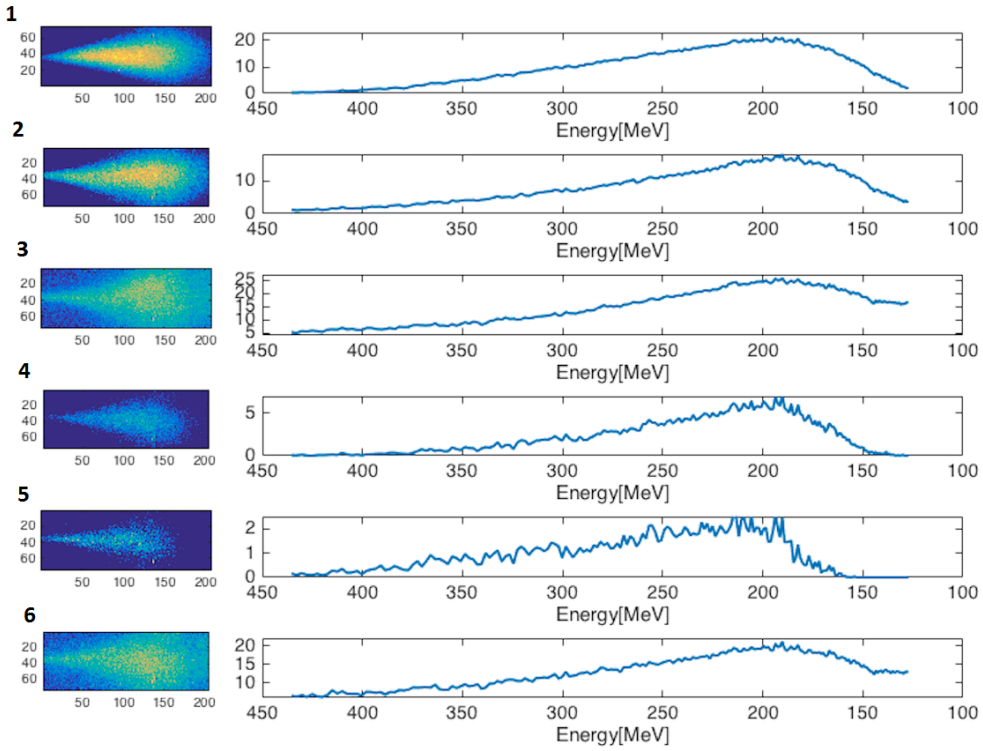

Figure 6.18. Electron energy measurements with magnetic spectrometer. On the left, image of LANEX foil impressed by the bent electrons. On the right, the corresponding integrated line profiles.

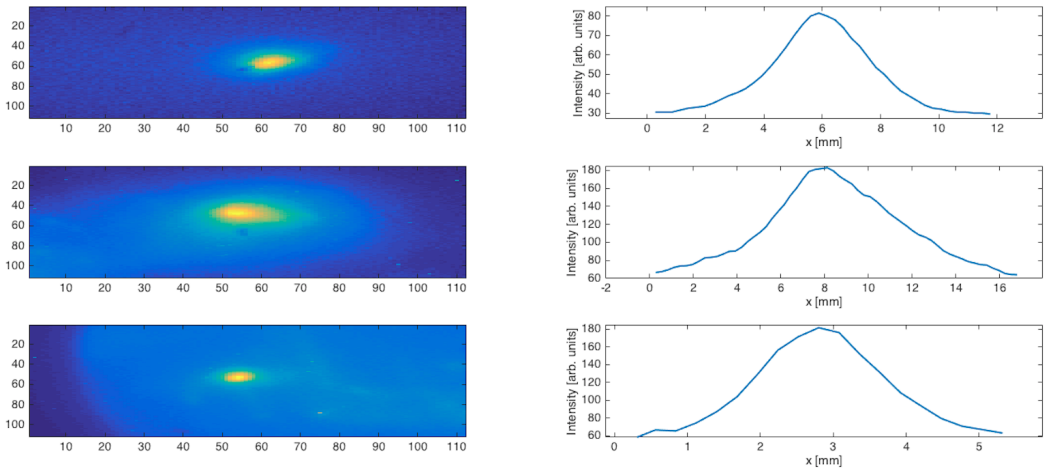

Figure 6.19. Transverse spatial profile measurements in working conditions. The diagnostics was composed by a LANEX screen, placed outside the experimental chamber, and a CCD camera Basler Scout scA640-70gm with a 35mm objective. The calibration has been found equal to 0.28mm per pixel.

	σ [mm]	θ [mrad]
1	1.7	3.4
2	2.6	5.2
3	1.1	2.2

Table 6.3. Electron transverse spatial profile measurement results related to Fig. 6.19.

$50cm$, the relative electron divergence has been measured in the range $3-5mrad$. These preliminary results, although not yet optimized, are really promising. Indeed, in such a small accelerating cavity ($\approx 2.5mm$), we are able to reach high energy electron beams with an acceptable divergence of few mrad that, in principle, can be managed with some magnetic quadrupoles.

6.2.1 FLAME final focus optimization

For LWFA experiments, it is essential to have a good quality focal spot and longitudinal profile of the laser. Therefore, an optimization of optical compressor and final focus stage of the FLAME laser has been done in order to improve the beam quality.

First of all, the whole optical line starting from the compressor up to the interaction point, where the OAP mirror focus takes place, has been reproduced with Zemax to understand the critical points of such a system. The optical compressor is

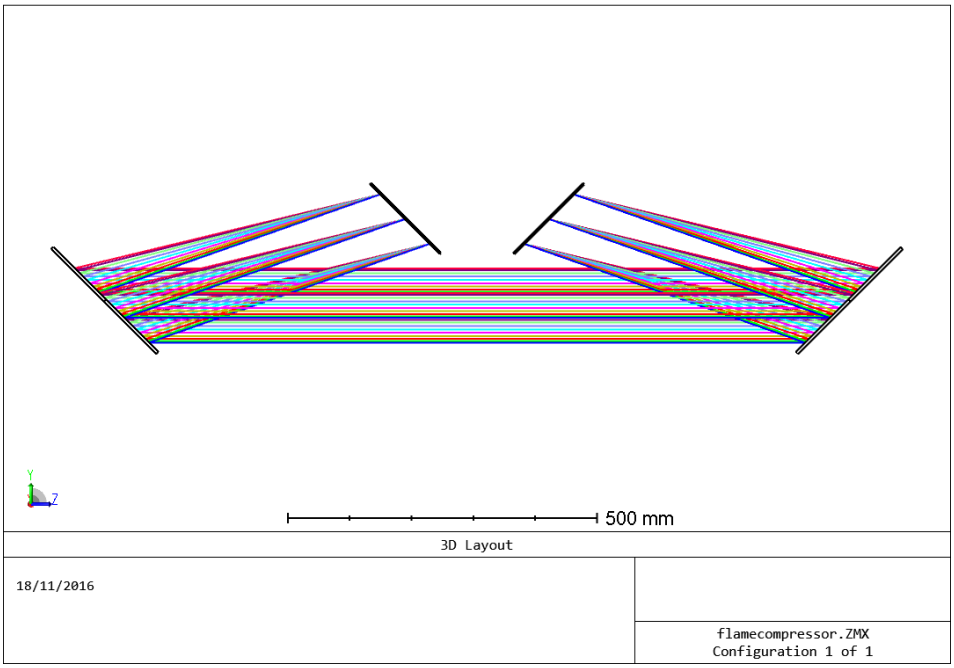

Figure 6.20. Ray-tracing of pulse compressor optical setup realized with Zemax for different wavelengths.

composed by four rectangular diffraction gratings (1600 grooves/mm). Figure 6.20 shows the set-up reproduced in Zemax. The laser pulse makes four passes before exiting: in the first two the spectrum is spread and then recombined and the pulse

compressed exploiting the different path of each wavelength; in the last two passes, the resulting spatial chirp is correct. The compression is perfect with no spatial chirp when the four gratings are parallel one with each other, otherwise the focal spot will have an elliptical shape. In Fig. 6.21 some examples of compressor misalignment are shown, looking at the focal plane of a lens. In detail, an example of focal spot

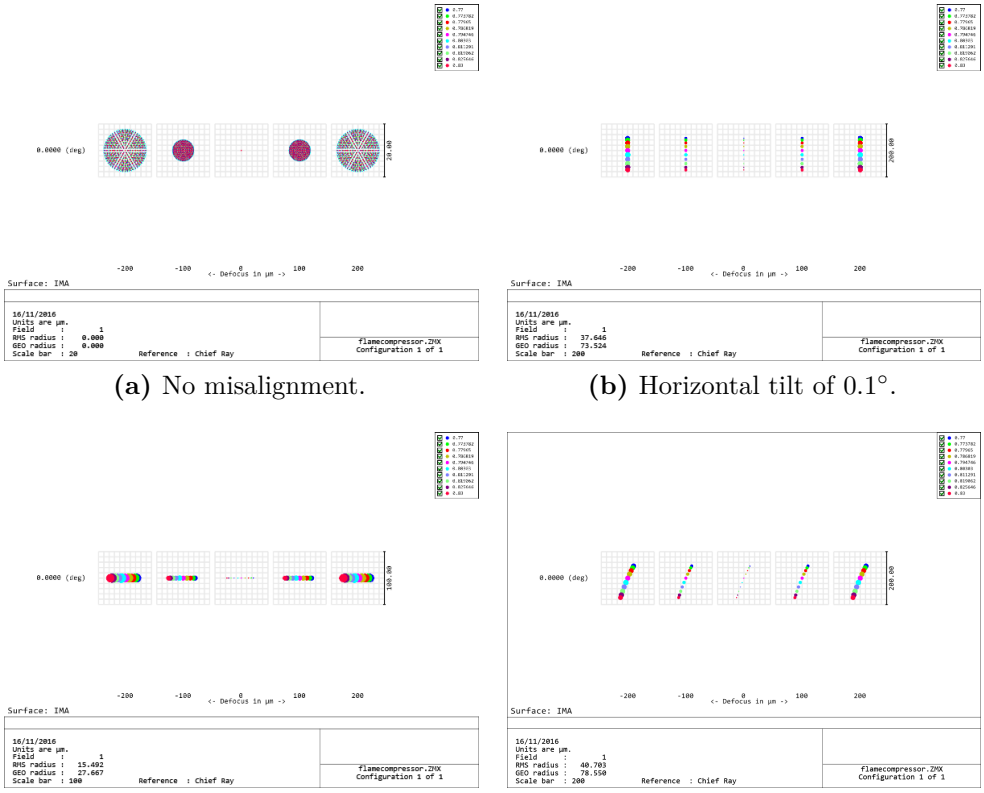

(a) No misalignment. **(b)** Horizontal tilt of 0.1°.

(c) Vertical tilt of 0.1°. **(d)** Horizontal and vertical tilt of 0.1°.

Figure 6.21. Example of focal spot with an OAP misalignment due to a tilt along both the horizontal and vertical axis.

with misalignment due to a tilt along the horizontal and vertical axis of one grating is shown. In detail, an offset equals to 0.1° has been considered. This example well models a typical experimental condition where the gratings are not perfectly parallel and, as a consequence, the spatial chirp is not completely removed. The FLAME compressor mounts allow to tune the tilt of single grating as well as the one of a couple of gratings. These knobs are enough in order to remove any residual spatial chirp.

The final focus in the target area is realized by means of an OAP mirror, with a $1m$ focal length, golden coated, and a reflective angle equals to 15°. The beam from the compressor is sent to the OAP trough two mirrors (Fig. 6.22). Figure 6.23 shows an example of focal spot with misalignment due to a tilt along the horizontal and vertical axis. In detail, an offset equals to 0.1° has been considered. This example represents a typical experimental condition where the OAP and the previous mirror have a different angle with respect to the nominal one (in this case

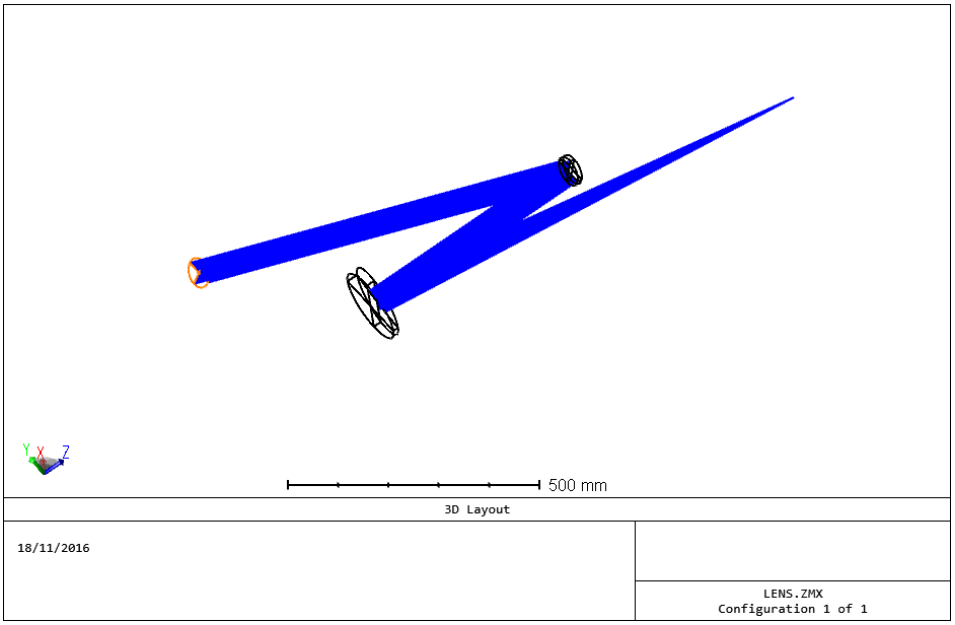

Figure 6.22. Zemax ray-tracing of optical setup for final focus by means of an OAP mirror. The beam coming from compressor is sent to the focusing element by means of two mirrors.

15°). By moving these two optical elements, it is possible to obtain a circular focal spot with diffraction limit size.

The optimization of the final focus has required two stages. In the first one, checking with a CCD camera the focus made with a spherical lens, the alignment of the optical compressor has been performed, making all four gratings parallel. Then, once a circular focal spot has been obtained, as second step the final focus in the vacuum chamber has been optimized by tuning the tilt angles of the OAP and of the mirror immediately before it. The experimental result is shown in Fig. 7.4, where a diffraction limit focal spot is presented.

6.3 Future outlook

The preliminary results on LWFA at FLAME, although not yet optimized, are really promising. Indeed, in such a small accelerating cavity ($\approx 2.5mm$ corresponding to plasma channel length), we are able to reach high energy electron beams ($\approx 300MeV$) with a quite acceptable divergence of few mrad. Certainly, as future upgrade, it will be designed a beam transport line based on permanent quadrupoles in order to obtain a more collimated electron beam. On the other hand, a better optimization of acceleration scheme will be done. First of all, a study with gas-jet of different diameters, such that the dephasing length is approximately equal to the acceleration length, reducing the energy spread, will be done in the near future. On the other hand, also a different approach, based on the employee of gas-filled tubes (gas-cell or dielectric capillary) will be investigate. In particular, this latter should give more control on the gas parameters with respect to the gas-jet.

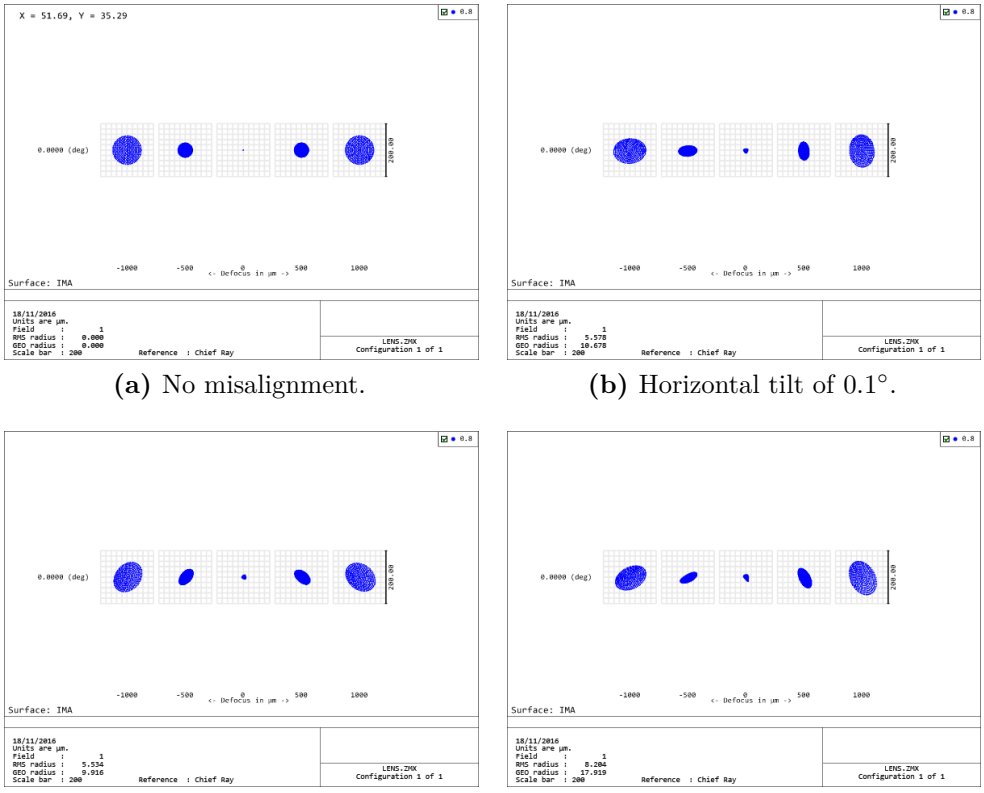

(a) No misalignment. **(b)** Horizontal tilt of 0.1°.

(c) Vertical tilt of 0.1°. **(d)** Horizontal and vertical tilt of 0.1°.

Figure 6.23. Example of focal spot with an OAP misalignment due to a tilt along both the horizontal and vertical axis.

Chapter 7

The EXIN Project at SPARC_LAB

Introduction

The external injection scheme represents a good compromise in plasma acceleration: by accelerating a preexisting electron bunch, coming from a RF linac, exploiting the plasma wakefield stimulated by an intense laser in a gas, it is possible to obtain a high energy boost at the exit of the plasma channel, keeping the initial electron beam quality (emittance and energy spread) almost unchanged. Nevertheless, this scheme is conditioned by the performances of existing RF technologies: the current limits in producing ultra-short bunches set the maximum value of the plasma wavelength λ_p that can be exploited to accelerate the electrons. Indeed, if the bunch length σ_z is longer than a significant fraction of λ_p, the accelerated bunch could suffer from an excessive amount of energy spread, leading to an unacceptable emittance dilution at the end of plasma stage [103]. Since the peak accelerating electric field inside the plasma E is proportional to λ_p^{-1} and $\lambda_p^{-1} \propto n_e^{1/2}$, then $\sigma_z << \lambda_p$ is also a constraint on the maximum accelerating gradient inside the plasma. Simulations show [90] that a safe plasma wavelength value is in the order of $100\mu m$, setting the plasma density to $n_e \approx 10^{17} cm^{-3}$ and the peak accelerating field $E_0 \approx 30 GV/m$, which however would be attained only in the highly non-linear bubble regime. Certainly, Increasing the plasma density could be an option, since the prescribed value assumes a working point for the linac which is far from the limit; however, with increasing values of E_0 and decreasing values of λ_p, the whole process becomes more sensitive to jitters of whatever nature.

Plasma wave regimes can range from linear to highly non-linear: the first are more stable but yield less intense accelerating fields which are non-linear functions of the radial and longitudinal coordinates, contributing in increasing beam emittance; the former are more unstable but produce higher fields. Despite stronger fields mean a greater final energy, this condition is more sensitive to any kind of jitter and on bunch mismatching. Therefore, a good choice seems then to be right in the middle, exploiting a quasi non-linear wave, which corresponds to a condition on the laser parameter $a_0 \approx 1$ [90]. Given a typical laser energy of a few Joules and a length of tens of fs, the condition $a_0 \geq 1$ is met with a laser spot size w_0 of few tens of

microns. For gaussian pulses, such a value implies a Rayleigh length at most of few centimeters, which is surely not enough to produce a significant increase of the electrons energy [90]. This problem can be solved by guiding the laser pulse over lengths which are usually much larger than the natural Rayleigh length. As previously discussed, the use of a dielectric capillary as laser waveguide can overcome this problem [92].

The EXIN (External-Injection) project [90], under development within the SPARC_LAB facility of the National Laboratory of Frascati (LNF-INFN), is dedicated to exploit the wakefield acceleration with particular care to the quality of the accelerated bunches. In this scheme, the wakefield will be created by the FLAME laser pulse propagating in a hydrogen gas filled capillary and it will be used to accelerate the electron bunches produced by the high brightness SPARC photoinjector. The main advantages of this scheme are twofold: first of all the electron bunch characteristics (emittance, energy spread, charge, etc.) are already well defined prior the wakefield acceleration stage and then, since the bunch generation is decoupled by the acceleration process, it might be possible to have more control on the injection mechanism i.e. the injection of the electron bunches into the accelerating field. Mastering this process is of crucial importance to preserve the initial quality of the bunches during the acceleration.

In this chapter, the experimental parameters of the project will be given. In detail, after a brief introduction about the dielectric capillary, numerical simulations in order to optimize energy coupling between FLAME laser and a dielectric capillary will be presented. Moreover, some preliminary results on laser-capillary alignment will be shown.

7.1 Experimental parameters

The experimental layout is shown in Fig.7.1. The electron bunches are generated by the SPARC photo injector with an energy of about $80MeV$, a normalized emittance of $1mm - mrad$, a charge $Q \sim 10pC$ and a repetition rate $1 - 10Hz$. The chosen acceleration regime is the "quasi non linear" with normalized laser intensity $a_0 \sim 1.1$ and a plasma density corresponding to a wavelength $\lambda_{plasma} \sim 100\mu m$. These values determine the range of the laser parameters (energy, temporal length, focal spot) and capillary dimensions to be employed: $(3-4)J$, $(30-40)fs$, $\sim 100\mu m$ and $(120-200)\mu m$ respectively. In particular, we are studying the possibility to use a $120\mu m$ diameter dielectric capillary where injecting first the high intense laser beam to stimulate the plasma wakefield and then the electron bunches to be accelerated. The main aim of this experiment is to demonstrate that a high brightness electron beam can be accelerated by a plasma wave without any significant degradation of its quality. Simulations show that the theoretical final energy achievable is around $630MeV$ [90].

Following the discussion in the previous section, for the best coupling condition of the FLAME laser beam a focusing element with $f = 5m$ (for a capillary diameter of $120\mu\ m$) is required. In detail, it would be preferably to employ an off axis parabolic (OAP) mirror in order to avoid any optical aberration and distorsion of the laser temporal and spatial profile. In order to measure the focal spot at each

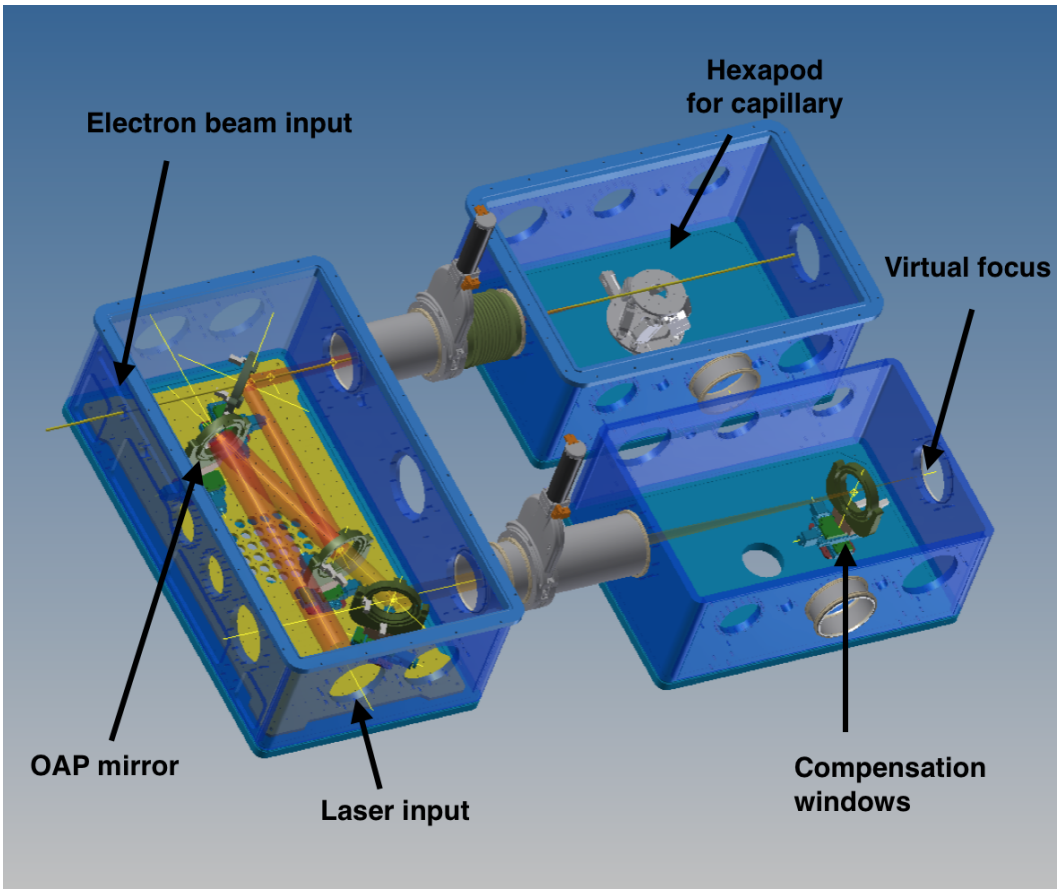

Figure 7.1. Layout of EXIN experimental chamber: laser beam will be focused by OAP mirror, while two mirrors are required for the alignment; dielectric capillary will be placed on a PI (*Physik Instrumente*) hexapod in order to properly align it; a diagnostic chamber will be installed to measure on-line the virtual focus, the laser spectral profile, the plasma spectral emission and other parameters that can characterize the acceleration process.[105]

shot, a virtual focus will be provided by focusing a beam loss (called diagnostic beam "DB") taken from the first mirror after OAP. Since this DB, will go through a thick tilt optic while focusing, it will be affected by optical distortion (astigmastism and coma) at the focus point, as simulated with ZEMAX (Fig.7.2b). In order to compensate for these distortions and to measure the effective focal spot, a system of compensating windows has been studied Fig.7.2a. By placing two windows as thick as the mirror substrate and tilted with the same angle, it's possible to remove any distortion if they are tilted around the longitudinal axis. From simulations the right tilting angles required to remove the astigmatism and coma are equal to 120° and 240° (Fig.7.2c).

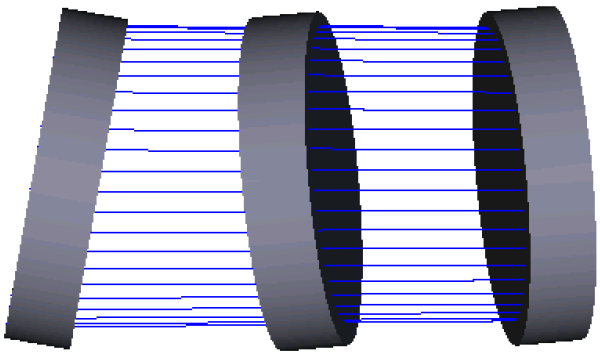

(a) *Compensating window system.*

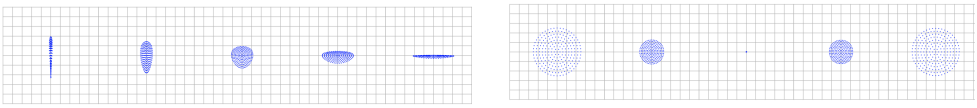

(b) *Virtual focus not compensated.* **(c)** *Virtual focus compensated.*

Figure 7.2. a. Layout of compensating windows system: part of beam goes through the first mirror after OAP and two windows compensate for aberrations. **c, b.** Virtual focus with and without compensating windows simulated by ZEMAX.[105]

7.2 Dielectric capillary waveguide: mathematical description

A dielectric capillary is an hollow fiber characterized by an empty internal core and an external glass wall, commonly made in borosilicate. This kind of waveguide is different from an optical fiber, where the core has a greater refractive index than the cladding. For this reason it exploits total internal reflection to guide a laser beam. Since the capillary does not have this characteristic, a laser beam will experience more losses during the propagation. Therefore, even though this kind of structure allows to keep the laser focused over several Rayleigh lengths, the transmission efficiency is no 100% and it has to be taken into account. Solving Maxwell's equations in cylindrical geometry, with boundary conditions for dielectric surfaces at the capillary tube inner wall, gives hybrid mode solutions, with quasi-transverse electromagnetic modes [104]. An incident linearly polarized Gaussian laser beam can be efficiently coupled to the linearly polarized family of hybrid modes, namely the EH_{1m} modes. The transverse electric components of the EH_{1m} modes at zero order can be found in [104]. For the EH_{1m} modes, the transverse electric field amplitude inside the capillary tube can be written as

$$E_{1m}(r,z,t) = J_0(k_{\perp m}r)exp(-k_m^l z)cos(\omega_0 t - k_{zm}z) \tag{7.1}$$

where $k_{\perp m} = (k_0^2 - k_{zm}^2)^{1/2}$ is the transverse wavenumber of the mode with order m and is given by $k_{\perp m} = u_m/R_{cap}$, R_{cap} is the capillary tube inner radius, u_m is the $m-th$ root of $J_0(x) = 0$, and J_0 is the Bessel function of integer order.

The exponential decay term in Eq. 7.1 indicates that the electric field is damped along the direction of propagation, z: each reflection at the dielectric capillary wall is associated with a refracted fraction of the laser beam inside the dielectric wall. This refracted fraction is minimal for the smallest perpendicular wavenumber, corresponding to the grazing incidence. The characteristic damping coefficient k_m^l is given by

$$k_m^l = \frac{u_m^2}{2k_{z0}^2 R_{cap}^3} \frac{1+\epsilon_r}{\sqrt{\epsilon_r 1}}, \tag{7.2}$$

where ϵ_r is the dielectric constant of the wall. This shows that k_{ml} strongly depends on the capillary radius, the wavelength of the incident laser beam, and the mode order, through u_m. Laser damping is usually described by the attenuation length $L_m^l = (k_m^l)^{-1}$. After a propagation distance of L_m^l, the field magnitude decreases by a factor $1/e$ and the beam energy by a factor $1/e^2$, owing to refraction losses.

7.2.1 Mode coupling efficiency

In order to optimize the laser injection into the capillary for LWFA, the key point is to maximize the amount of energy coupled to the first EH_{11} mode [104]. The energy coupling efficiency between the fundamental mode EH_{11} and the laser, focused at the capillary entrance, can be computed [105] as

$$\begin{aligned} \eta_m &= \frac{\int |EH_{11} \cdot E_{laser}|^2 dr}{\int |EH_{11}|^2 dr \int |E_{laser}|^2 dr} \\ &= \frac{\int |J_0(u_m \frac{r}{a}) \cdot \mathcal{F}(\rho(r) \cdot e^{(-\frac{r}{w_0})^{2n}})|^2 dr}{\int |J_0(u_m \frac{r}{a})|^2 dr \int |\mathcal{F}(\rho(r) \cdot e^{(-\frac{r}{w_0})^{2n}})|^2 dr}. \end{aligned} \tag{7.3}$$

In Eq. 7.5, $E_{laser}(r) \propto \mathcal{F}(\rho(r) \cdot e^{(-\frac{r}{w_i})^{2n}})$ is the electric field of the laser in the focus, where $\mathcal{F}$ identifies the Fourier transform operator, $\rho(r)$ is the lens pupil function that describes the lens aperture and w_i the initial beam radius at $1/e$. The laser transverse profile is assumed supergaussian of order n. In particular, for $n = 1$ Eq. 7.5 refers to a gaussian transverse profile. In this case, it can be seen that the maximum coupling of the laser in the fundamental mode occurs for $\omega_0/R_{cap} \simeq 0.65$, where ω_0 is the laser beam waist. Here, the 98% of the energy is coupled with the EH_{11} mode.

Numerical simulations for FLAME

Nevertheless, the FLAME high power lasers is characterized by a super-Gaussian, rather than Gaussian, transverse profile. To find the best energy coupling condition for a super-Gaussian laser profile, numerical simulations have been performed. The characterization of the FLAME laser intensity (Fig. 7.3) reveals a super-Gaussian spatial profile of order $n = 8$ and a diameter of $FWHM = 8cm$. The beam intensity at focal plane (Fig. 7.4) presents two secondary lobes, whose peak intensity is about 1.6% of the principal one. Since they will hit the cladding wall, with intensities of the order of $10^{16} W/cm^2$, these peaks can significantly damage the capillary. To overcome this problem, the use of a tapered capillary [106] or the possibility to

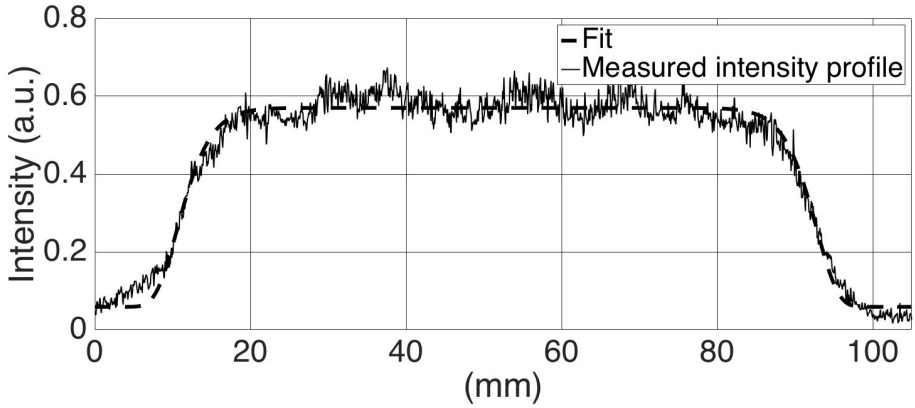

Figure 7.3. FLAME measured intensity profile. From a super-Gaussian fit, it figured out n1/48 and FWHM1/48cm.[105]

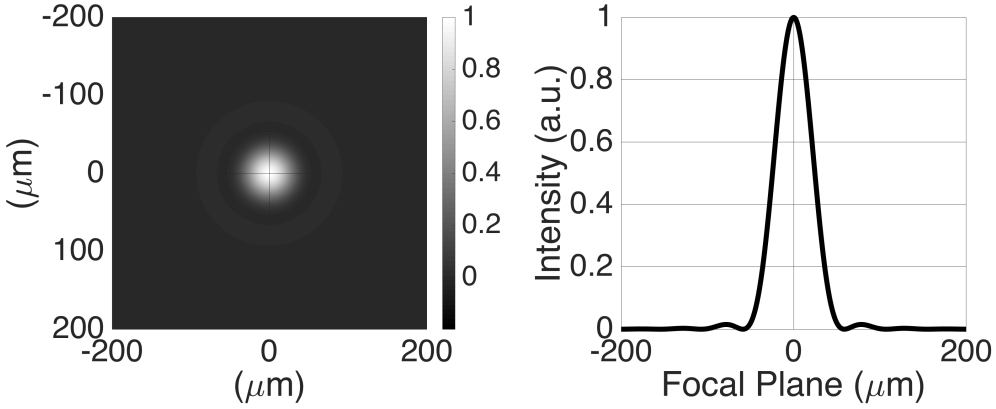

Figure 7.4. Intensity profile at focal plane of a lens with focal length $f = 5m$ and aperture radius $R = 76.2mm$. [105]

introduce a ceramic diaphragm, to spatially filter out the secondary lobes, is under study. Simulations have been performed for the first three hybrid modes. As shown in Fig. 7.5, the best coupling condition equals to 89.80% is fulfilled for $w/a = 0.70$, where w is the radius at $1/e^2$ of the first lobe of the intensity profile, or equivalently $r_0/a = 0.98$, where r_0 is the first zero.

7.3 Preliminary experimental results

Some preliminary tests have been performed in order to study how the laser-capillary coupling can be affected by misalignments, in particular by an offset in the transverse plane (Fig. 7.7) and by a tilt in the longitudinal plane (Fig. 7.8). Those effects have been measured by moving the PI (Physik Instrumente) hexapod where the capillary was placed. Hexapod platforms are used for precision positioning and alignment of loads in all six degrees of freedom, i.e. three linear axes and three rotational axes.

The experimental setup is shown in Fig. 7.6. A CW $800nm$, $80mW$ power, p-polarized, TEM_{00} mode diode laser has been focused on the capillary entrance

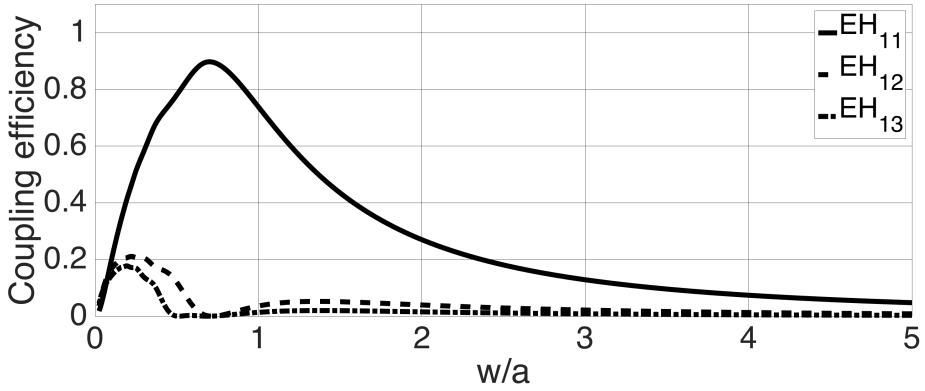

Figure 7.5. Energy coupling efficiency between the focused super-Gaussian laser beam and e.m. modes in a dielectric capillary. The best coupling value is equals to 89.80% for $w/a = 0.70$, where w is the radius at $1/e^2$ of first lobe of intensity profile. The simulation has been performed for the first three modes EH_{11} (solid line), EH_{12} (dashed line), and EH_{13} (dash-dot line).[105]

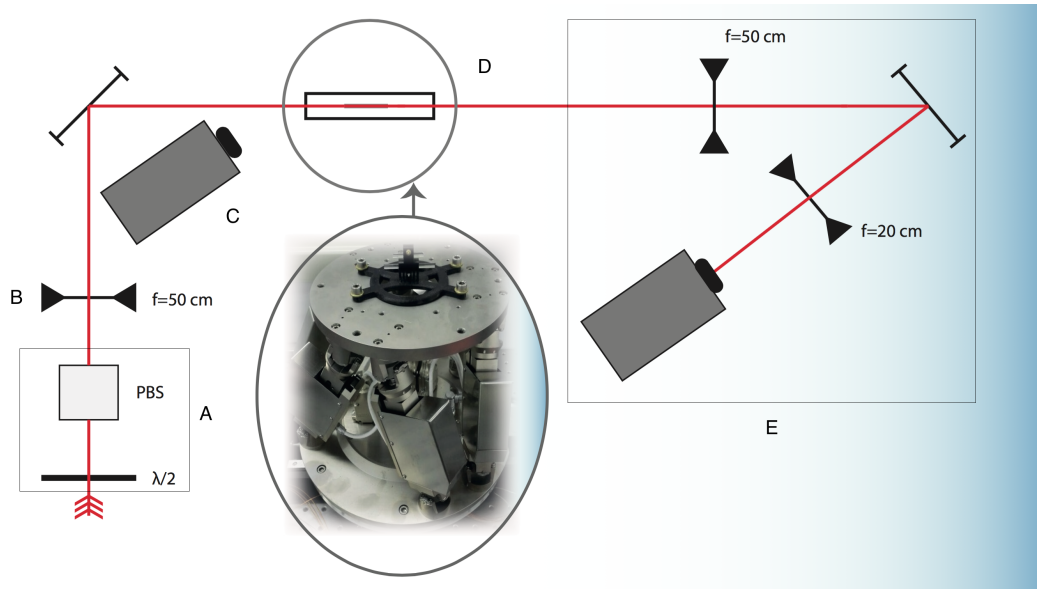

Figure 7.6. Experimental setup for alignment test. (A) Input energy control; (B) focusing lens; (C) CCD camera to check the alignment at the capillary entrance; (D) dielectric capillary holder sitting on hexapod; (E) imaging system to measure the spot size at the exit of capillary. [105]

and the alignment has been controlled by a CCD camera on the side. The capillary is made in borosilicate with a refractive index for this wavelength equals to $n = 1.45$. A two-lenses imaging system has been used to analyse the laser spot at the exit of the capillary. The coupling with the EH_{11} mode is significantly maintained for a maximal offset of about $20\mu m$ (Fig. 7.7d) and a maximal tilt of about $5mrad$ (Fig. 7.8c).

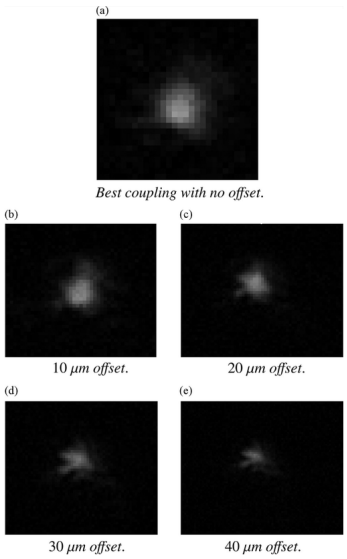

Figure 7.7. Results of misalignment test with an offset in the transverse plane. (a) Best coupling with no offset, (b) $10\mu m$ offset, (c) $20\mu m$ offset, (d) $30\mu m$ offset, and (e) $40\mu m$ offset.[105]

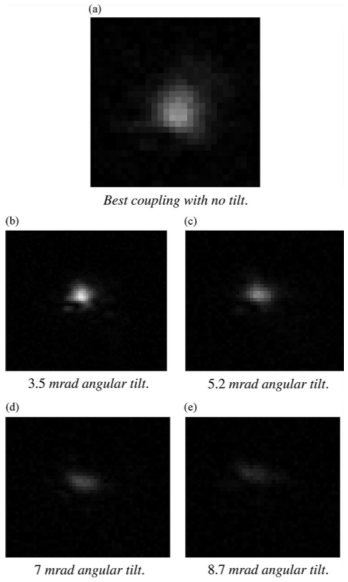

Figure 7.8. Results of misalignment test with a tilt in the longitudinal plane. (a) Best coupling with no tilt, (b) $3.5mrad$ angular tilt, (c) $5.2mrad$ angular tilt, (d) $7mrad$ angular tilt, and (e) $8.7mrad$ angular tilt.[105]

Chapter 8

Novel transverse diagnostics tool for plasma accelerated electron beams

Plasma based accelerators have demonstrated the ability of delivering high energy beams in a very compact dimensions. There are several challenges related with these new techniques and one among the other is the possibility to produce high brightness beams. We focus our attention only on the plasma accelerated beams.

In order to measure the longitudinal and transverse properties of such beams new diagnostics techniques must be used, adapting existing methods or inventing new ones. We concentrate only on transverse measurements and in particular on emittance measurements. The main issues for this diagnostics are the shot to shot instabilities and the large energy spread characterizing the electron beams from plasma acceleration. Therefore only single shot measurements are eligible for such a task. In this chapter the development of a new diagnostics tool able to measure electron beam emittance in a single shot way will be presented, together with simulations and some preliminary results.

8.1 One Shot Emittance measurement

When the space charge contribution is negligible the quadrupole scan [108] is the most used technique to measure the emittance. It is based on the measurement of the beam transverse spot changing the current in one or more quadrupoles. But it is a multi shot measurement and because it uses magnetic lenses, it is very sensitive to energy spread [109]. Unfortunately up to now there are not reliable and well established single shot measurements of transverse emittance, while several experiments have been already carried out, as reported in [110].

Optical Transition Radiation (OTR) is emitted when a charged particle crosses the boundary between two media with different index of refraction. It is well known since many years [111], but only in the '90s received attention as powerful diagnostics tool. We focus here on the incoherent part of the radiation emitted at wavelength shorter than the bunch length. It happens often in the visible range.

While collecting and imaging the emitted radiation is a simple system to measure

the beam charge transverse distribution and also its dimensions, there are more information hidden in the angular distribution of the radiation: the energy and the angular spread of the beam that produced it.

A simple setup is shown in Fig.8.1 where the radiation, coming from a metallic screen (often a silicon aluminated plate) placed at 45° with respect to the beam line, is later split in two arms. In the first one the detector is placed in the image plane of an optical system, while in second one in the focal plane. With such a device in every single shot the beam image and the radiation angular distribution can be recorded. In Fig.8.2 there is an example of a central line profile of the angular distribution of

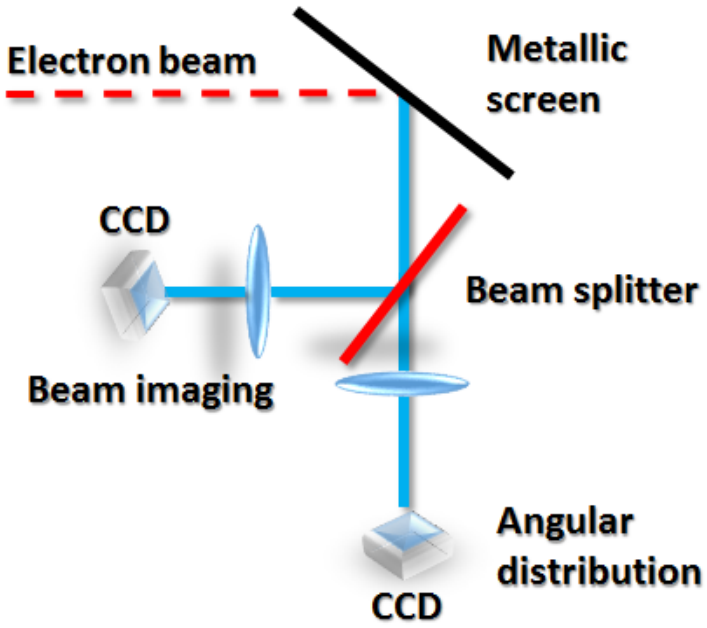

Figure 8.1. Simple setup to measure in the same shot both beam size than beam divergence.

the OTR for a beam at $125MeV$, in two different conditions: a parallel beam, i.e. without angular spread, and with $1mrad$ divergence. The most relevant effect is the reduced visibility of the central minimum. In both cases the beam is supposed to be

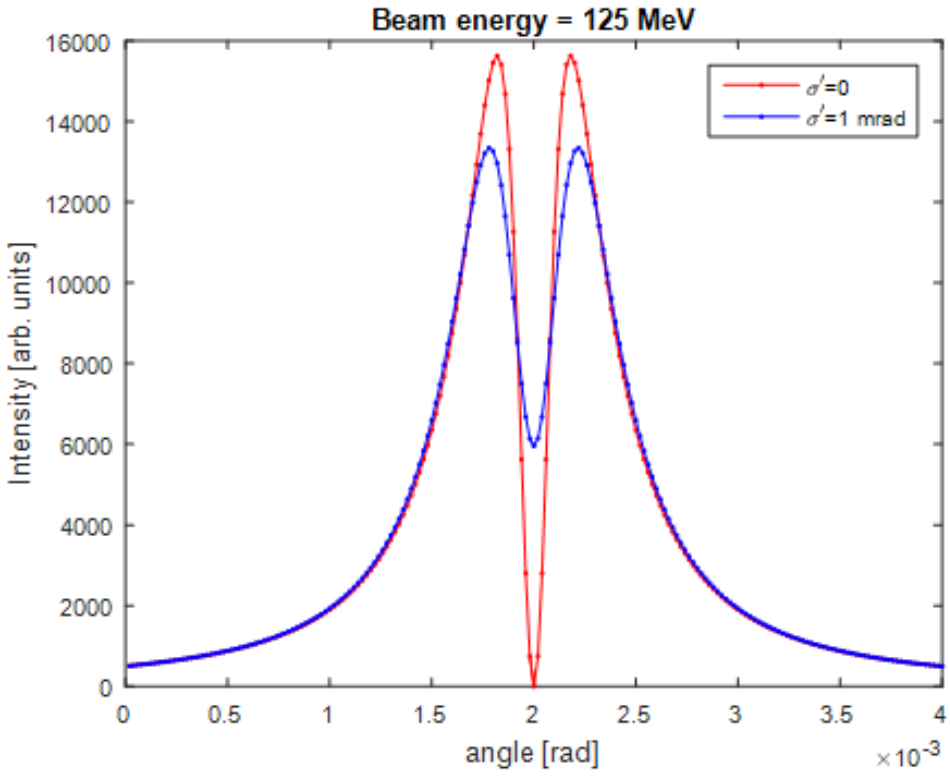

Figure 8.2. Line profile of the OTR angular distribution for $125 MeV$ electron beam with different angular spreads.

monochromatic. The effect of the energy spread is indeed very weak and becomes appreciable only with values higher than several tens of percents.

Using the conventional formula for the angular distribution of the OTR [111], neglecting constants, and making the ultra relativistic approximation we get:

$$I \propto \frac{\sin^2\theta}{\left(1-\beta^2\cos^2\theta\right)^2} \simeq \frac{\theta^2}{\left(\frac{1}{\gamma^2}+\theta^2\right)^2} \tag{8.1}$$

where β and γ are the usual relativistic factor, while θ is the angle of a ray with respect to the specular reflection on the screen. Convoluting the previous formula with a Gaussian distribution in angle, being σ' the rms beam divergence, we have:

$$I \propto \frac{1}{\sqrt{2\pi}\sigma'} \int_{-\infty}^{\infty} \frac{(\theta-\xi)^2}{\left[\frac{1}{\gamma^2}+(\theta-\xi)^2\right]^2} e^{-\frac{\xi^2}{2\sigma'^2}} \tag{8.2}$$

By solving the former equation we obtain [112]:

$$I \propto \frac{\mu}{\nu}\mathrm{Re}\left[\Phi(z)\left(\frac{1}{2}+\mu\nu z\right)\right]-\mu^2 \tag{8.3}$$

where $\nu = 1/\gamma$

$$\mu = \frac{1}{\sqrt{2\pi}\sigma'}$$

$$\Phi(z) = \frac{1-erf(z)}{e^{-z^2}}$$

$$z = \mu\left(\nu + i\theta\right)$$

and $erf(z)$ is the complex error function. So there is an analytic formula describing this behavior and it gives the possibility to easily fit the experimental data in order to retrieve the value of the σ'. Using the information coming from the beam image and the radiation angular divergence, both values of beam dimension and beam divergence can be obtained in a single shot. However the correlation term is not measured in this way.

Using a Gaussian for the distribution of the particle transverse momentum is reasonable for most of the cases, especially in the linacs. However where there are strong correlations between position and angle, or mixing of horizontal and vertical planes, or in general when the distribution is not anymore Gaussian this treatment cannot be apply and a reasonable guess of such a distribution must be considered.

With a setup similar of Fig.8.1 it was already possible ([113], [114]) to measure the emittance in a beam waist, where the correlation term is zero. The authors used a two foils setup, instead of a single one, a configuration sometimes called Wartski interferometer [115]. In such a configuration the radiation emitted from the first foil interferes with the emission from second foil, leading to an interference pattern. It has the advantage of increasing sensitivity of the effect coming from the beam divergence, but the setup is strongly dependent on the relative distance between the foils, where the best setup is related to the ratio between the foils distance and the formation length. When the beam energy changes also the radiation formation

length is modified, with a scale law going as γ^2, and so the foils distance should be accommodate every time in order to have the best resolution. Moreover the first interface scatters the beam spoiling the value of the emittance for high brightness beams, if the energy is not in the GeV range.

The sensitivity to the beam divergence is a critical issue for such a diagnostics. If we call visibility

$$V = \frac{I_{MAX} - I_{MIN}}{I_{MAX} + I_{MIN}} \tag{8.4}$$

where I_{MAX} and I_{MIN} are the maximum and minimum of the intensity distribution. We have the maximum visibility equal to 1 only in the case of a perfect parallel beam, i.e. when the intensity of the central minimum is exactly zero. In optical system usually the visibility is measured through the contrast via the modulated transfer function. It is quite standard to assume as a threshold value for the resolution the 10% of the visibility. In our case we have to consider that the minimum could be also spoiled by some noise, especially in the parallel beam condition, where its value is exactly zero. So this definition fits consistently with our experimental condition.

If we consider to vary the energy and find the value of the σ' that corresponds to 10% visibility we obtain the plot of Fig.8.3 The described behavior has a simple

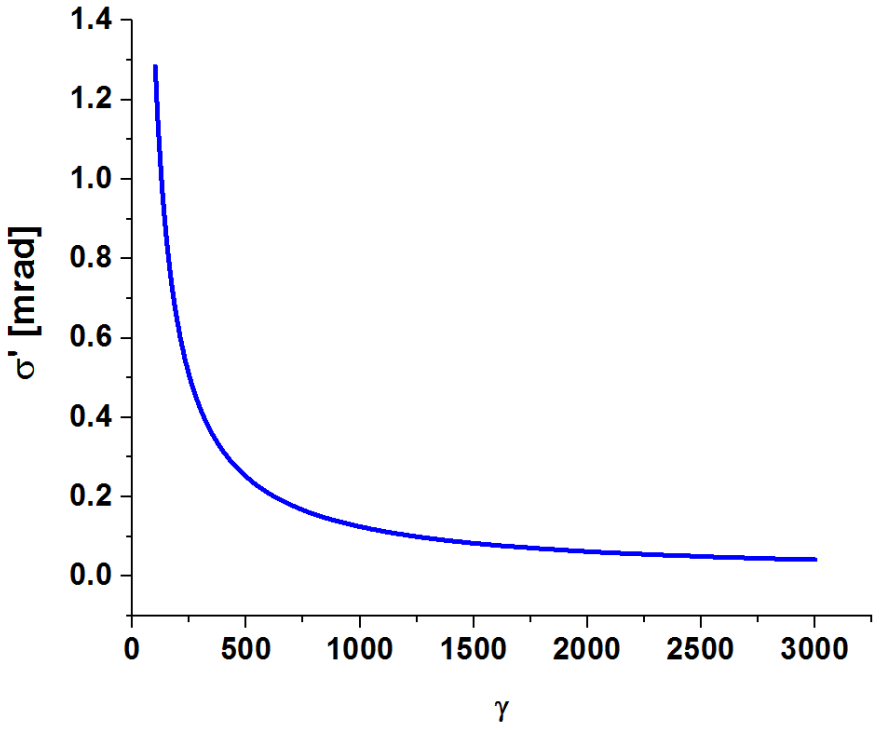

Figure 8.3. Resolution limit for the beam divergence vs beam energy.

physical interpretation. Electrons that arrive on the metallic target with a different angle with respect to the beam propagation produce a cone of radiation with a center not at $\theta = 0$, but at the angle of their direction with respect to this value.

The overlap of all the distributions resolves in the increasing value of the central minimum. At low energy the angular distribution is very wide. So even in presence

of angular spread the overlap of all distributions has not a big impact on the central minimum. However when the energy grows up the angular distribution narrows and even a small change in the angle of the emitted radiation has a big impact. This is the reason why this diagnostics is very appealing for laser plasma accelerated beam where the σ' is usually in the order of $mrad$, and it has the sensitivity to resolve the value even at $100MeV$. In the conventional accelerators it can be consider only if the energy is high enough to measure the divergence according to the curve in Fig.8.3.

8.2 Experimental setup

So far we described a technique already used but valid only in a beam waist. However for its own nature the plasma acceleration has strong shot to shot fluctuations and a beam waist cannot be guaranteed also because it implies the use of focusing optics. So the correlation term must be measured for every single shot.

A tentative has been made already in [116] several years ago. Instead of having directly the angular distribution, an image is produced in both arms of the setup in Fig.8.1, placing a mask to cut the peripheral part of the beam. Another lens makes the angular distribution of the emerging radiation. This is not a single single shot measurement because it was needed to remove the mask, but it gave for the first time the possibility to have two points where divergence and beam size were correlated.

In our setup the correlation term is measured in every single shot. Our experimental setup is shown in Fig.8.4. The light coming out from a silicon aluminated screen is divided but a 90:10 beam splitter. The 10% is then used to image the beam in a Hamamatsu Orca II camera, high quantum efficiency, equipped with a Nikon $f = 180mm$ focal length F/2.8. The other part arrives on a $f = 400mm$ focal length achromatic doublet. In the image plane of such a lens, with a magnification 1:1, is placed a Thorlabs mounted lens array. These are plano-convex lenses, with a pitch of $300\mu m$, and a focal length of $18.6mm$.

Extensive simulations have been performed in Zemax to understand the effect of possible aberration of such a lens system. A complete virtual measurement has been simulated, starting from the radiation produced by a bunch charge and propagating in the whole optical system. No significant effects of aberration in the microlenses have been found. The focal length of the microlens array is very small, just $18.6mm$, so for geometrical constrains it is impossible to place the detector directly on its focal plane. Instead we put another achromatic lens with focal $f = 5cm$ to image with 1:1 magnification this focal plane into our intensified camera, an Hamamatsu Orca IV.

8.3 Zemax simulations

Transition radiation [111] from charged particles is commonly used for diagnostics purposes in accelerator facilities and as THz source for spectroscopy applications. Therefore, the optical analysis of this radiation is crucial to properly retrieve its characteristics, starting from the generating charged particle beam. For this purpose,

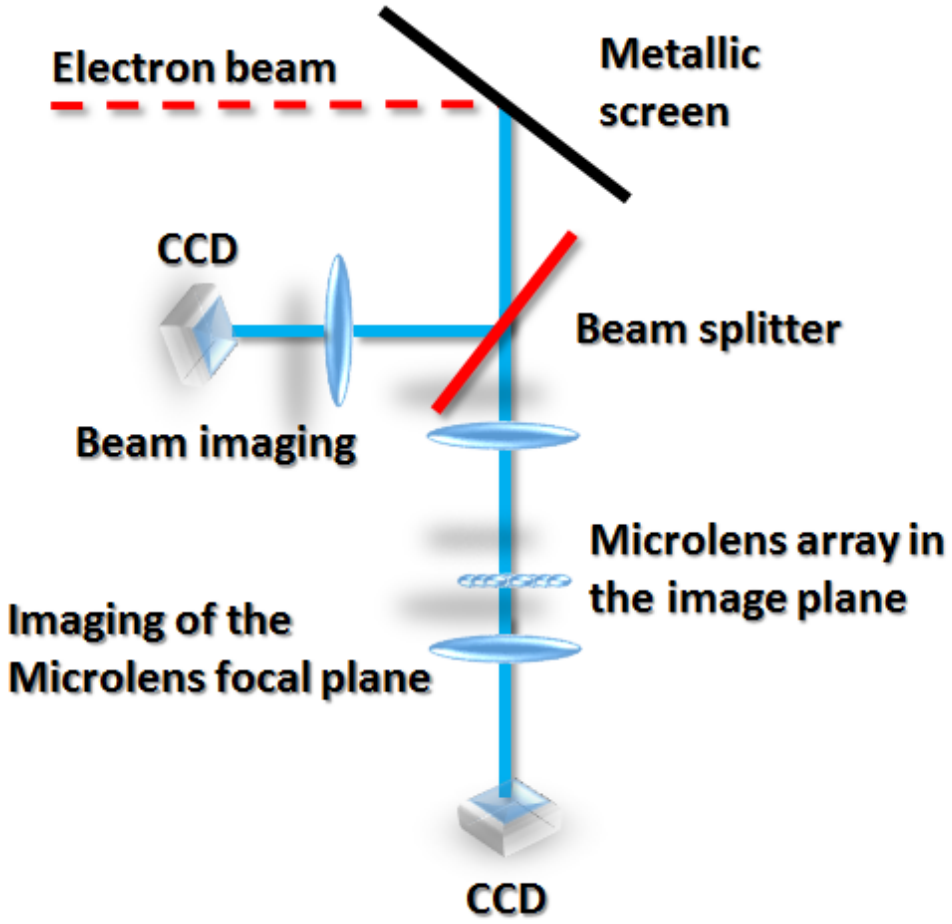

Figure 8.4. Experimental setup: a replica of the beam is produced in the two arms. In the second one in the image plane there is a microlens array. Their focal plane is imaged in a CCD detector.

an innovative code written in Zemax has been developed [117] in order to simulate and analyze both coherent and incoherent transition radiation as generated by relativistic electron bunches. In particular, the angular divergence has been implemented, necessary to study the behavior of this new emittance diagnostics. The simulations have been performed by means of Zemax optical design software. Although it is commonly used for illumination and lens design purposes, it allows to simulate many kinds of optical systems [118]. In detail, the software provides two different analysis modes: geometrical ray tracing and physical optical propagation (POP). Concerning the first one, it represents a good solution to simulate the behaviour of an optical system in the ray approximation, by neglecting any diffraction effects related to the wave nature of light. Therefore, in order to take into account any effects due to wave nature of radiation, e.g. polarization and diffraction, the use of POP mode is mandatory.

The beam is represented by an array of discretely sampled points, analogous to the discrete sampling using rays for a geometric optics analysis. The entire array is then propagated through the free space between optical surfaces. At each optical surface, a transfer function is computed which transfers the beam from one side of the optical surface to the other. In particular, the software can choose automatically the propagator to be used by checking the Fresnel number defined as $N_F = a^2/(\lambda L)$, where a is the radial size of the beam, λ is the wavelength and L the distance from the beam to the observation point. In general, for $N_F < 1$ the Fraunhofer diffraction is computed, while for $N_F > 1$ the Fresnel propagator is used.

In order to simulate the optical propagation of transition radiation, a DLL has been compiled to provide the right electric field to Zemax. The library contains the instructions for Zemax to build the input electric field. In detail, the real and imaginary parts of both the horizontal (h) and vertical (v) polarization components of the single electron TR electric field have been defined as follows [121] :

$$E_h^{real} = \Big[\alpha K_1(\alpha r) - J_0(kr)/r\Big]\cos(\phi),$$
$$E_v^{real} = \Big[\alpha K_1(\alpha r) - J_0(kr)/r\Big]\sin(\phi),$$
$$E_h^{img} = E_v^{img} = 0.$$

Here, $\alpha = 2\pi/(\gamma\lambda)$, γ is the Lorentz relativistic factor, λ the optical wavelength, $k = 2\pi/\lambda$, $r = [(x-x_0)^2+(y-y_0)]^{1/2}$, $\phi = \arctan[(y-y_0)/(x-x_0)]$ is the azimutal angle in the transverse plane, (x_0, y_0) are the coordinates of each electron, K_1 and J_0 are the first order modified Bessel function and the $0-th$ order Bessel function, respectively. The DLL allows to choose the wavelength and the gamma factor of single electron TR electric field. In Fig. 8.5 single electron TR electric 2D intensities and central line profiles are shown.

In order to take into account the finite size of the beam, a Zemax routine has been developed exploiting the Zemax Programming Language (ZPL) provided with the software suite. The ZPL is a macro language specifically designed for use with Zemax in order to offer the power of user-extensibility. ZPL is similar to the BASIC programming language, where capabilities and functions unique to ray tracing and physical optics have been added.

This specific routine has been designed in order to propagate individually TR

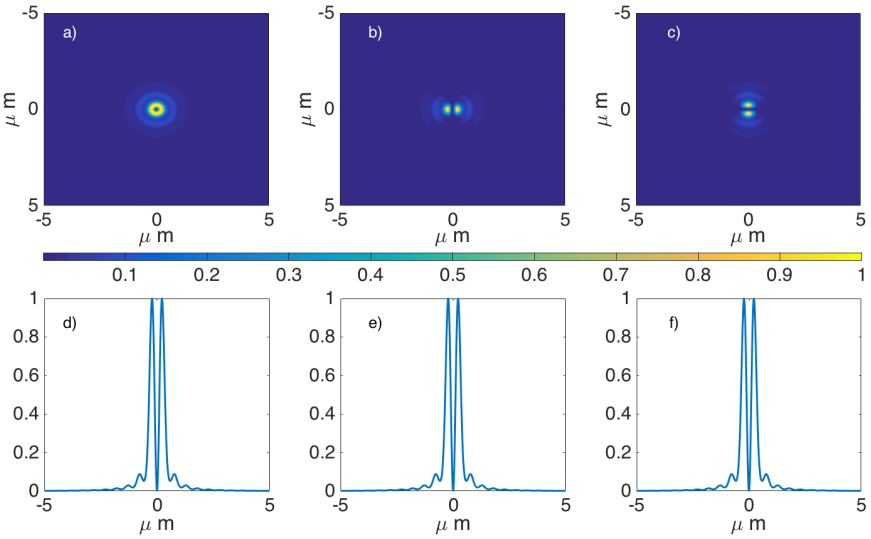

Figure 8.5. **a)** Single electron TR total intensity, **b)** Horizontal polarization and **c)** Vertical polarization. **d)**, **e)**, **f)**) corresponding central line profiles. These profiles are for $\gamma = 250$ and $\lambda = 500nm$ at the source.

fields of an electron bunch with gaussian transverse profile and sum all of them at the end, coherently or incoherently. The single terms of sum are weighted by gaussian spatial distribution. Furthermore, the possibility offered by Zemax to start with an angle with respect to the optical axis has been exploited in order to take into account the electron angular divergence.

The power of this routine is the possibility to use it with every optical system to be analysed. In fact, it acts on the layout of Zemax lens data editor and it is totally uncoupled from that: nothing has to be modified in the code in order to adapt it to a custom set up. Only electron beam characteristics, in terms of spatial and angular distributions, have to be setted in the routine to properly simulate the propagation.

In order to validate these simulations, for incoherent OTR angular distribution an analytical formula, taking into account electron beam transverse momentum distribution [120], has been used. In detail, by starting from single electron angular distribution and making convolution over gaussian angular divergence, for the radiation intensity distribution in the far field approximation it has been found [112]

$$\begin{aligned} I &= \frac{e^2\beta^2}{\hbar^2 c\sigma\sqrt{2\pi}} \int_{-\infty}^{+\infty} \frac{(\theta-\xi)^2}{[\gamma^{-2}+(\theta-\xi)^2]^2} e^{-\frac{\xi^2}{2\sigma^2}} d\xi = \\ &= \frac{e^2\beta^2}{\hbar^2 c} \Big\{ \frac{\sqrt{\pi}\mu}{\nu} Re\Big[\Phi(z)\Big(\frac{1}{2}+\mu\nu z\Big)\Big] - \mu^2 \Big\} \end{aligned} \tag{8.5}$$

where $\Phi(z) = (1 - erf(z))/(exp(-z^2))$, σ is the r.m.s. angular divergence, $\mu = \sigma^{-1/2}$, $\nu = \gamma^{-1}$ and $z = \mu(\nu + i\theta)$.

In next sections, simulations performed by means of Zemax will be shown and compared with the analytical formula given by Eq.8.5.

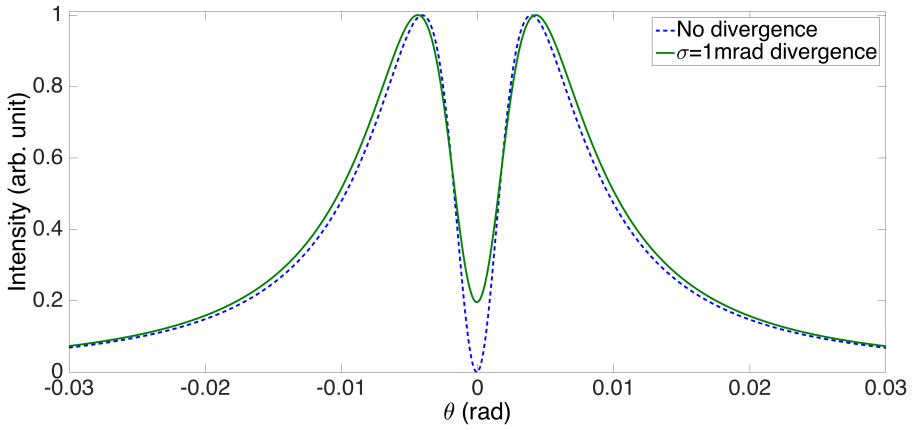

Figure 8.6. OTR angular distribution central line profiles with (solid line) and without (dashed line) beam divergence. With $\gamma = 250$ and $\sigma = 1mrad$ the difference in the central dip is equals to 0.2. By increasing energy, a raising of this effect can be evaluated. Both curves are normalized to 1.

8.3.1 Analysis on TR angular distribution

For sub-ps long electron beams, $F_{||}(\lambda) \sim 0$ in the visible spectrum and the TR can be considered fully incoherent. Therefore, the total intensity is the sum of the single electron contributions.

In Fig.8.6 incoherent OTR angular distribution profiles of an electron beam with and without transverse momentum are shown. By looking at the focal plane of a lens, any initial momentum is mapped in a position in the observation plane. In this way, taking into account the electron beam transverse momentum, the center of each angular distribution results spatially displaced, unlike the no divergence case. Therefore, for the incoherent radiation, the main difference from ideal case with zero divergence can be found in the central dip between the two lobes, is not equal to zero when divergence is taken into account. On the other hand, the beam transverse size does not affect the OTR angular distribution [120].

In order to test our code, simulations have been performed for two main cases: angular distribution in the focal plane of 1) ideal and 2) real lens. The wavelength chosen for both cases is $550nm$, for an electron beam with a gaussian divergence with $\sigma = 1mrad$ and $\gamma = 250$.

Angular distribution in ideal lens focal plane

Zemax provides different kinds of surfaces. One of them is the *paraxial*, corresponding to a surface working as an ideal lens, i.e. no aberrations are taken into account. The main parameter related to that is the paraxial focal length. In this case, the lens focal length has been chosen equal to $f = 10mm$. Indeed, since the optical propagator acts as a Fourier transform, the sampling spacing in the focal plane becomes $\Delta x_2 = \lambda f/(n_x \Delta x_1)$ [118], where n_x is the array size and x_1 corresponds to the initial spacing.

In order to avoid resolution loss, the initial field has been sampled with a

2048×2048 array in a square window $2.048mm$ large and, to keep the same spacing, the final field has been re-sampled in its original size. Indeed, to discriminate angle of $100\mu rad$ with a $10mm$ focal length, a minimum sampling spacing equals to $1\mu m$ is needed.

Angular distribution in real lens focal plane

Zemax gives the possibility to design any kind of lens, by choosing the material, the surface radii and other properties. For this simulations, the lens that has been simulated is a fused silica plane-convex singlet, since it is the simplest and most diffused one. The convex surface radius has been chosen in such a way the lens focal length was equal to $10mm$.

For the same argument discussed in the previous subsection, the initial field has been sampled with a 2048×2048 array in a square window $2.048mm$ large. Also for this case, the final field has been re-sampled in its original size to avoid resolution loss.

Analysis of beam divergence contribution

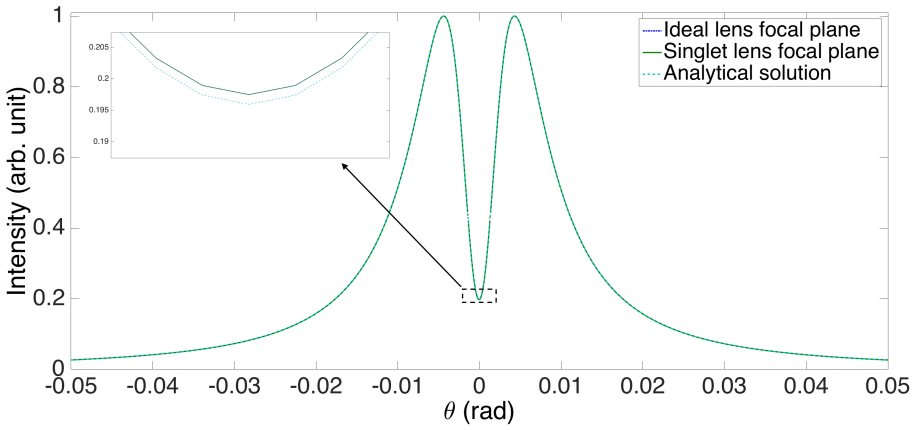

Figure 8.7. OTR angular distribution central line profile. In this picture, the different simulation results are compared also with the analytical solution. All of them are in agreement with this latter. In the upper left corner, a closer view of the OTR dip is shown: the difference between simulated and analytical distributions in the dip is less than 1%.

In Fig.8.7 the simulated angular distribution profiles have been shown and compared with the analytical solution Eq.8.5. Since they are all overlapped, there is no issue due to different optical set-up. Indeed, the flexibility represents the main characteristics of this routine. Looking closer the dip, angular distribution in ideal and real lens focal plane have exactly the same value, showing that, in this case, the aberrations do not affect the result. However, the difference with respect to the analytical solution is less than 1%. This difference could be decreased by increasing the angular spacing. It's important to stress that the effect of beam

transverse momentum is observable in the single electron TR case, but it only appears considering the radiation generated by the whole electron beam.

Behavior with microlens array

The previous results show that the code works properly in simulating the angular distribution of TR in the focal plane of a single lens. In order to optimize the experimental setup for the one shot emittance measurement in Fig. 8.4, some physical optical simulations have been performed, exploiting the code developed and tested for the single lens case. The implementation of the microlens used for the experiment has been quite simple: Zemax offers a model for such a kind of optics and the user just have to specify the glass substrate, the focal length the number of microlenses and the distance among them.

In Fig. 8.8 an example of simulation result is shown and compared with an experimental measurement. In particular, $\gamma = 250$, $\sigma = 0.360mm$, $\sigma'_x = 0.026mrad$ and $\lambda = 550nm$ has been considered.

8.4 Preliminary results at SPARC_LAB

The experiment has been performed at SPARC_LAB photoinjector [48], using $200pC$ bunch charge at $125MeV$. The maximum energy was limited by the use of only two of the three accelerating sections. The third one was not available due to a severe problem to its klystron. Looking at Fig.8.3 it is evident that in this energy range the minimum detectable beam divergence is in the order of $0.5mrad$. Even if we have tried to deteriorate the value of the emittance and focus the beam in one dimension in order to push the beam angular spread over this value we did not succeeded.

In Fig.8.8 is reported a qualitative comparison between a simulated pattern behavior and a real single shot measurement. Every illuminated lens produces its own radiation ring. Analyzing the single OTR angular distribution is possible to retrieve the value of the angular spread. The qualitative agreement between simulation and measure is excellent. We extract from every single ring the profile and we fit them. In Fig.8.9 there is an example of one of these fits. As expected the fit is very good but the value of the angular spread is about 500 μrad, totally dominated by the resolution limit at this energy. From a quadrupole scan measurement we found that the beam angular divergence, even in a waist, it should be around 250 μrad, a factor 2 less than our resolution limit. In Fig.8.10 the result of the angular distribution in a beam vertical waist. As expected just one line of the microlens array is illuminated by the radiation. Even if we did not measure the emittance, this preliminary result demonstrates that it is possible to produce the OTR angular distribution from different part of the beam image.

8.5 Future outlook

The optimization of LWFA process and a good quality for the accelerated electrons are crucial in order to test our new diagnostic tool concerning the measurement of electron beam emittance in a single shot way. Indeed, particular attention has to

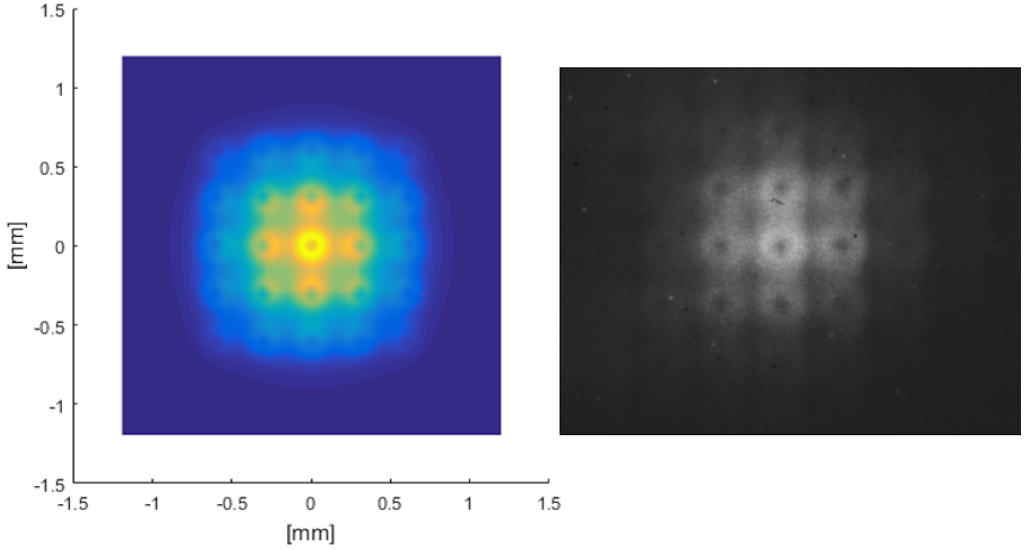

Figure 8.8. Comparison between a simulation (left) and a first measurement (right)

be given to the angular divergence that should be $1mrad$ at maximum with these energies. In this sense, the realization of a simple magnetic transport line will help. On the other side, the experimental setup as shown in Fig. 8.4 is already placed in the FLAME target area. At the same time, a new experimental run is foreseen at SPARC_LAB when the new klystron will be installed. In fact, it will allow to reach an electron energy, around $180MeV$, high enough to have a good angular resolution for the emittance measurement (see Fig. 8.3).

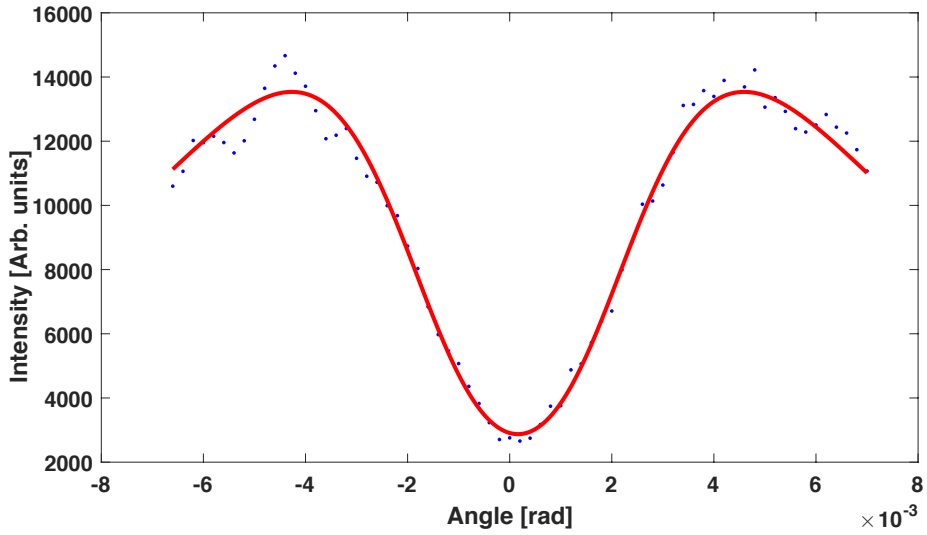

Figure 8.9. Comparison between experimental data and a fit for one of the OTR angular distribution.

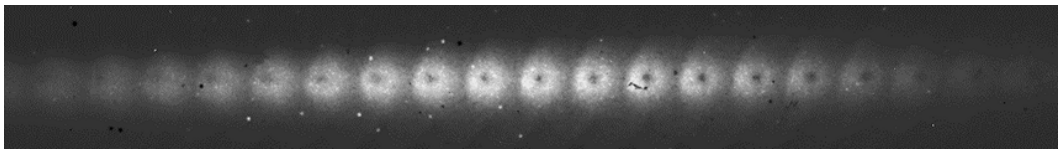

Figure 8.10. Image of the angular distribution of a beam in a vertical waist.

Chapter 9

Characterization of fast electrons emitted during laser-solid target interactions

Introduction

Recent advances in laser technology opened up new horizons in modest-scale experiments of sub-picosecond light-matter interactions, enabling new research areas like astrophysics in laboratory [122], high energy density experiments [123] and novel schemes for particle acceleration [124, 125]. Ion acceleration from thin foils irradiated by high-intensity short-pulse lasers, in particular, has attracted high attention during the past decade since the emitted ion and proton pulses contain a large amount of particles with energies in multi-MeV range [126, 127, 128] and are tightly confined in time (picosecond-scale) and space (source radius is few microns). These outstanding characteristics provide possibilities for a wide range of applications in nuclear and medical physics [129].

The physical picture of the process is the following (see Fig. 9.1). Electron jets are produced at the early stages of the interaction [131]. Some electrons are energetic enough to escape the target while others remain at the vicinity of the surface, re-hitting it and ejecting secondary electrons [132]. After the escaping of the first ones, a positive unbalanced charge is left on target, leading to the formation of the electrostatic potential that in turn governs the ion acceleration [133, 134]. The typical timescale of such phenomena is on the sub-picosecond level. During this process the electronic cloud locked near the target is thermalized and there are energetic electrons (on the 'hot' tails of the overall energy distribution) that can still escape from the target. This process however comes to an end when their energy can not overcome the electrostatic potential induced near the target surface, whereas a second slower expansion-relaxation process takes over [135]. Although the plasma density generated away from the target drops by orders of magnitude, the majority of electrons is confined within a distance of the order of the Debye length [136].The escaping energetic electrons constitute the electric current charging positively the target [137] and leading to the generation of a potential barrier. Its lifetime is dictated mainly by the return currents, cloud dynamics and thermalization rates at

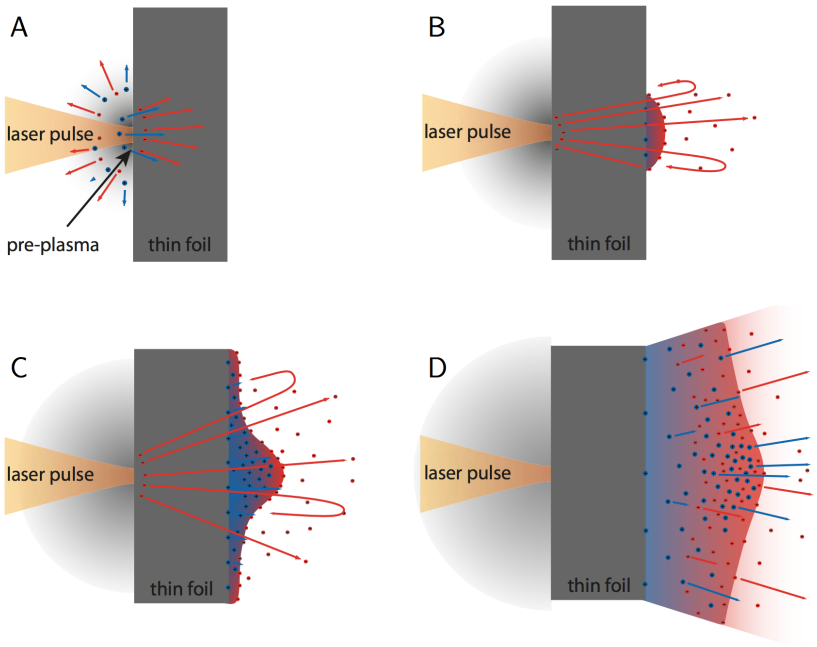

Figure 9.1. Acceleration by electric charge-separation fields at the rear side of a thin foil. **A** - Ionization and pre-plasma creation by the weak precursor of the main laser pulse (ASE or pre-pulse). **B** - Interaction of the main pulse with pre-plasma: absorption of laser energy and acceleration of hot electrons. **C** - The resulting positive charge of the foil forces some electrons to turn around and reenter the target, leading to the formation of a strong charge-separation field. The atoms on the surface are ionized and accelerated. **D** - Ion expansion into vacuum following the escaping electrons.[130]

the target surface. The intensity and time duration of this barrier eventually sets the limit on the late-time processes e.g. acceleration of the positively charged ions [138]. For sub-picosecond laser pulse irradiation, one can neglect the charge neutralization of the positively charged ions by the electrons coming from outer darkened sections of the target and assume that the number of escaped energetic electrons defines the net positive charge left on the target surface [135]. The subsequent cooling process, including multiple collisions with the surrounding ions, sets the maximal time of the target charging, i.e. the effective lifetime of the potential barrier. A direct experimental evidence of these processes requires sub-picosecond measurements of charge density near the surface or alternatively tracing down the escaping electrons. So far this task remained elusive and only indirect time integrated measurement of radiated electromagnetic pulses [139, 140] or magnetic fields [141] were reported.

In this chapter, a meaningful experimented conducted at FLAME concerning the interaction between a high intensity laser with a solid target will be discussed. In detail, it has been measure for the first time the temporal profile of the electric field carried by electrons escaping from the rear surface of the target. The study of this field is crucial to understand the acceleration of ions and protons realized with this kind of phenomena. Moreover, testing targets with different shape, a significant increase in the charge and energy of the escaping electrons, when the geometrical

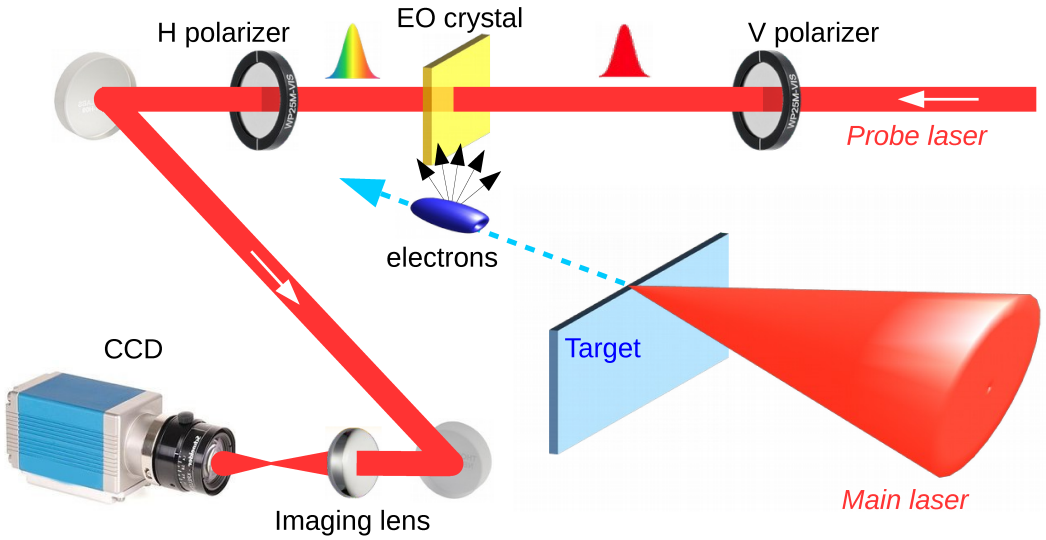

Figure 9.2. Sketch of the experiment. An f/10 parabola focuses the main laser on a metallic target ejecting a cloud of energetic electrons. An electro-optic crystal (ZnTe) is located $1mm$ downstream the target. The Coulomb fields of the moving electrons optically modify the crystal, making it birefringent. This changing is temporally encoded by a linearly polarized probe laser. By measuring the polarization modulation of the probe laser, the main properties of the emitted electrons (charge, energy, temporal profile) are retrieved.

target curvature is increased, has been measured. This point represents a direct evidence of the growth of the electrostatic potential induced near the target surface and thus an enhancement of the accelerating gradient for the emitted ions [142]. This kind of measurements have been performed thanks to the electro-optical sampling method, related to the birefringence induced in a crystal by an external electric field [143]. My role in this experiment has concerned the realization of the whole setup, included the EOS diagnostic and the synchronization lines. In addiction, I played the laser system during all the experimental campaign, taking care of its optimization following the desired parameters.

9.1 Experimental setup

The experiment, whose set-up is shown in Fig. 9.3, has been performed with the FLAME laser at the SPARC LAB test-facility [48] by focusing its high-intensity ultra-short-pulses (up to $4J$ energy and $35fs$ pulse duration) on solid targets of different thicknesses and shapes. Snapshots of the emitted electrons are provided by an Electro-Optical Sampling (EOS) device [143] making use of a $500\mu m$ thick ZnTe crystal installed $1mm$ downstream the target. Being this distance much larger than the Debye length (less than $1\mu m$ in our experimental conditions), only the highly energetic ejected electrons that escaped the potential barrier are able to reach that location. A secondary laser beam ($35fs$ duration), directly split from the main laser, has been used as probe going through the crystal while simultaneously the

electron cloud is moving below it. Its temporal profile is imprinted along the probe by crossing the crystal with an incidence angle of 28°. This allows to achieve a total time window of about $10ps$ and to provide less than $100fs$ temporal resolution. The high resolution EOS diagnostic technique allows to operate on the same time scale of the process, determined by the duration of the driving laser pulse [**?**]. Previous reports on ion acceleration by exploiting high intensity short pulse lasers have demonstrated a significant energy enhancement of the accelerated ion when structured targets [144, 145, 146] were used instead of the conventional planar target in the Target Normal Sheath Acceleration (TNSA) scheme. The underlying interpretation of these results is that, during the interaction of the laser pulse with sharp structured targets, higher quantity of electrons escape the target leaving behind a stronger potential well, which in turn can accelerate the ions to higher energies. In order to prove this conjecture a direct time-resolved measurement of the escaping electrons is required. We therefore employed our method and investigated the influence of target shape on the amount and energy of the escaping electrons by using a $10\mu m$ thick aluminum foil, a wedge shape of stainless steel razor blade and a tip shape of a needle. Measuring the charge quantity and energy of the escaping electrons by means of the EOS detector provides the required evidence for the field-enhancement conjecture.

9.2 Electro-Optical Sampling measurement method

In order to retrieve the main properties of the emitted electrons (charge, energy and duration) from the measured EOS signals, a numerical simulation code has been developed in MATLAB environment. It starts calculating the transverse electric field $E_V(t)$ of a gaussian electron bunch travelling at energy E in vacuum at distance r from the ZnTe crystal. The simulation then takes into account the dispersive propagation of such field in the ZnTe crystal, with thickness d. Being $n(\omega)$ and $\kappa(\omega)$ the ZnTe refractive and absorption indices in the Fourier domain, the propagating field is given by

$$E_o(\omega) = A_{tr}(\omega)E_v(\omega)exp\Big(i\frac{\omega}{c}(n(\omega) + i\kappa(\omega))d\Big), \tag{9.1}$$

where $A_{tr}(\omega) = 2/(n(\omega) + i\kappa(\omega) + 1)$ is the amplitude transmission coefficient. The sampling is performed by a co-propagating probe laser pulse whose initial linear polarization gradually becomes elliptical due to the electro-optic effect induced by the propagating field. Being λ_L the laser central wavelength, the overall phase delay accumulated by the probe laser at the end of the crystal is given by the convolution

$$\Gamma(t) = \frac{2\pi d}{\lambda_L} n_0^3(\lambda_L) r_{41} E_p(t) * \tilde{E}_L(t), \tag{9.2}$$

where n_0 and r_{41} are the ZnTe optical refractive index calculated in λ_L and its electro-optic coefficient, respectively. $\tilde{E}_L(t)$ represents the normalized (dimensionless) laser electric field, also assumed to be gaussian. The process terminates by simulating the signal output ($\propto sin2(\Gamma(t)/2)$) on the CCD camera. Figure 9.5 shows the resulting encoding process as detected by the CCD camera. e probe laser laterally

enters into the crystal while the bunch, moving normally and near to it, induces a local birefringence. The bunch electric fields gradually penetrate the crystal and the localized birefringence moves vertically with a speed c/n_0. This leads to an overlap of the probe and the birefringence along a curved path and thus a circular shape in the EOS output signals. Since the shape and strength of the detected signals depends on the bunch parameters used to calculate $E_v(t)$, by comparing the experimental data with the simulated one it is possible to extrapolate such information.

9.3 Experimental results

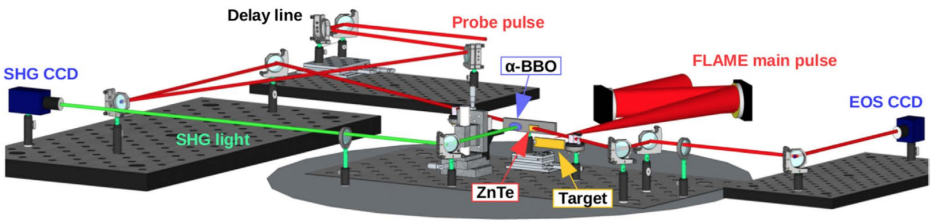

Figure 9.3. Layout of the experiment setup for EOS measurements at FLAME. An f/10 parabola focuses the main laser on a metallic target ejecting a cloud of energetic electrons. An electro-optic crystal (ZnTe) is located $1mm$ downstream the target. The Coulomb fields of the moving electrons optically modify the crystal, making it birefringent. This changing is temporally encoded by a linearly polarized probe laser. By measuring the polarization modulation of the probe laser, the main properties of the emitted electrons (charge, energy, temporal profile) are retrieved.

A more detailed experimental layout of the target area is shown in Fig. **??**. The laser beam is focused by means of f/10 off-axis parabolic mirror with focal length $f = 1m$. The focal spot is optimized using a deformable mirror. This allows reaching focal spots on target of the order of $25\mu m$. The probe laser used in the EOS diagnostics is split before the last multi-pass amplifier and re-compressed to 35 fs duration by its own optical compressor. The laser-target interaction occurs in a high vacuum environment ($10^{-6}mbar$).

The main and the probe beams have been synchronized in correspondence of the EOS crystal using the autocorrelation technique. In detail, by spatially overlapping the two beams on a BBO crystal, the temporal syncronization at femtosecond level has been retrieved thanks to a time scanning by means of a delay-line with 3 fs resolution, maximizing the sum frequency generation non-linear effect. A specific imaging system placed inside the vacuum chamber has been designed in order to check the laser-on-target alignment during the experiment (see Fig.9.4). More in detail, Since the FLAME EOS system exploits a probe laser directly split from the main laser, it ensures a jitter-free synchronization, and implements the spatial encoding technique [147] in which the bunch longitudinal profile is encoded along the probe transverse profile (6 mm diameter). The encoding is obtained by passing through the crystal with an angle ($\theta = 28°$ in our case): being ti (xi) the bunch (laser) longitudinal (transverse) coordinate, it follows that $t_i = x_i \tan\theta/c$ and the resulting time window is about $10ps$. Finally, the induced modulation in the probe

polarization is converted in a modulation in its intensity (readable by a CCD camera) by means of a linear polarizer downstream the EOS crystal. Fig. 9.5 shows the resulting encoding process as detected by the CCD camera. The probe laser laterally enters into the crystal while the bunch, moving normally and near to it, induces a local birefringence. The bunch electric fields gradually penetrate the crystal and the localized birefringence moves vertically with a speed c/n_0. This leads to an overlap of the probe and the birefringence along a curved path and thus a circular shape in the EOS output signals.

The use of a $500\mu m$ thick ZnTe crystal fixes the final EOS resolution to less than $100fs$. Since the resulting signal detected by the CCD is $I_{CCD} \sim I_{probe} \sin(2\Gamma)$, by measuring its amplitude we can estimate the overall bunch charge (proportional to the E_b term). The error associated with the retrieved charge is thus given by the laser energy instability (about 1%). The EOS can also be used in order to estimate the mean electron energy by measuring its time of flight (TOF) [148] Δt_{TOF} . Indeed, the knowledge of Δt_{TOF} allows to estimate the bunch velocity as $v = d/\Delta t_{TOF}$ and its energy as $E = \gamma m_e$, where $\gamma = 1/1 - (v/c)^2$ is the relativistic Lorentz factor, c is the speed of light and m_e is the electron rest mass. Unlike conventional time-integrated spectrometric techniques, this method is able to provide energy measurements resolved in time. The calibration of the EOS system been performed by focusing the FLAME laser with an intensity of about $5 \times 10^{18} Wcm^{-2}$) on the edge (about $1\mu m$ thick) of a wedge target. The resulting time-resolved signals, recorded at different delays of the probe laser, are showed in Fig. 9.6 (a-c). The signal corresponds to a total charge of $2.1nC$ of energetic electrons that have been ejected from target and traveled up to the EOS crystal in the form of 'bunch' with $1ps$ duration. Moreover, an estimated mean energy of $15MeV$ has been retrieved. The reproducibility of the results is proved by looking at the three frames of Fig. 9.6 (a-c), obtained by delaying the probe with respect to the main pulse: the signal structure remains unaltered while it moves in time (from the up-right to the down-left corner). This is confirmed in Fig. 9.6 (d-f) where a numerical simulation of the EOS output is provided for such electron bunches. The results, summarized in Fig. 9.7 have been obtained by focusing the FLAME laser on different target shapes. The geometry of FLAME EOS setup (where the bunch is moving below the crystal and normally to it while the probe laser propagates laterally from right to left) determines the curved shape of the retrieved signals. The snapshots show that the escaping energetic electrons from the planar and blade targets present a secondary, broadened temporal structure (see Fig. 9.7 (d) and (b), respectively). The duration and energy of the electron bunch is derived by measuring the bunch time of flight up to the EOS detector and by fitting it with numerical EOS simulations. In the case of the planar foil target, the resulting snapshot in Fig. 9.7 (a) shows the presence of a first emitted bunch with approximately 1.2 nC charge and 7 MeV energy followed by a second broadened structure carrying a larger amount of particles (about 3 nC). If we assume that the delay (about 1.5 ps, see Fig. 9.7 (d)) is due to different bunch velocities, the latter one has about 1 MeV energy. For the wedged target, the snapshot in Fig. 9.7 (b) shows a similar structure. The first bunch now carries a larger amount of electrons (2 nC) at the same energy (7 MeV) while the charge in the second bunch is strongly reduced to 0.3 nC. The temporal delay in this case is about 2 ps, as reported in Fig. 9.7 (e). Electron bunches coming from the tip

target are showed in Fig. 9.7 (c). In this case the interaction with laser produced a much larger number of released electrons (about 7 nC) at higher energies (about 12 MeV). Due to the large amount of charge, the birefringence induced in the ZnTe crystal leads to a rotation of the probe laser polarization larger than $\pi/2$ and the EOS signal in Fig. 9.7 (f) is consequently distorted. The overlaying red line shows the retrieved charge profile. These results provide a direct evidence of charge and energy boost when using sharp tips. Another feature, possibly attributed to this target shape, consists in the presence of a second smaller bunch (B2), carrying about 3 nC charge. The difference in the slope of the two signals in Fig. 9.7 (c) may be due to the fact that B2 is emitted along a different path, rotated by about 50° with respect to B1. It follows that B2 traveled a longer distance (about $600\mu m$) in order to reach the EOS crystal and its signal is delayed by about 2 ps, as reported in Fig. 9.7 (f). The experimental results showed in Fig. 9.7 are in agreement with Particle-In-Cell (PIC) simulations.

9.4 Particle-In-Cell simulations

A numerical study has been conducted in order to reproduce the interaction of a high-intensity short-pulse laser with wedged targets by using the 2D particle-in-cell (PIC) code TURBOWAVE [149]. Numerical simulations include detailed description of the interaction near the surface and reveal the formation of the electron cloud and ejection of the fast energetic electrons. The simulations consist a surface with micron-scale target local perturbations (in order to mimic the experiment) interacting with laser intensity of $10^{18}W/cm^{-2}$, a spot diameter of $10\mu m$ and an overall 30 fs duration. Fig 9.8 demonstrates the electron spectrum as function of energy for two different time delays, 100 fs and 350 fs after the laser hits the surface. The majority of the electrons after 350 fs are slow (below $3MeV$). In agreement to the experimental results there are trapped electrons up to $\sim 4MeV$ while electrons with higher energy escaped and moved towards the detector.

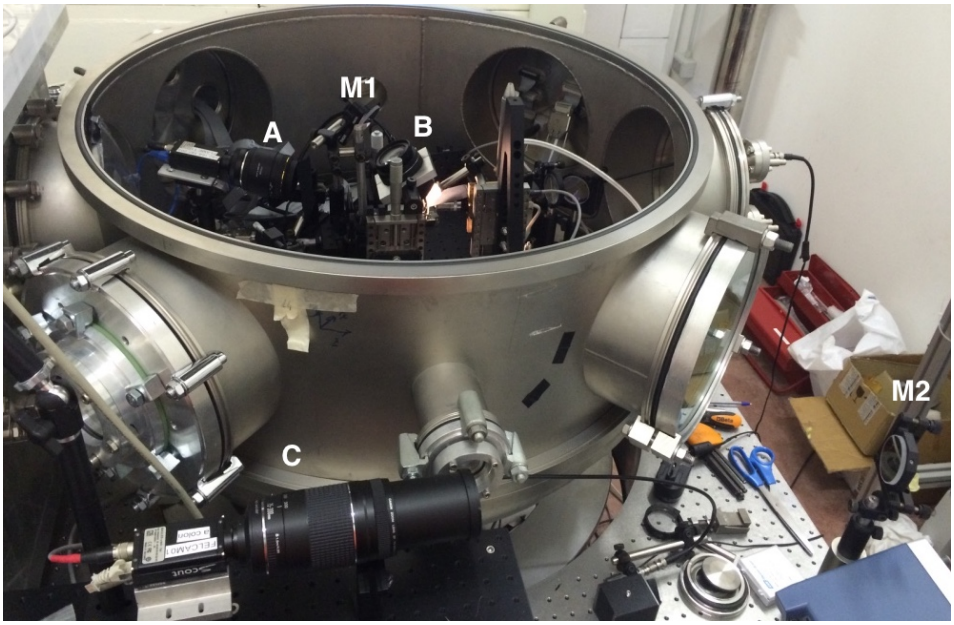

(a) View on the experimental chamber and the ancillary side breadboard hosting part of the imaging system.

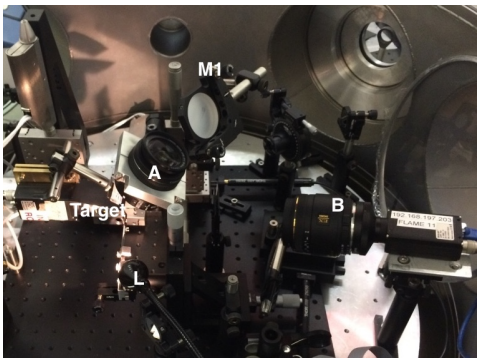

(b) Side view of the interaction point.

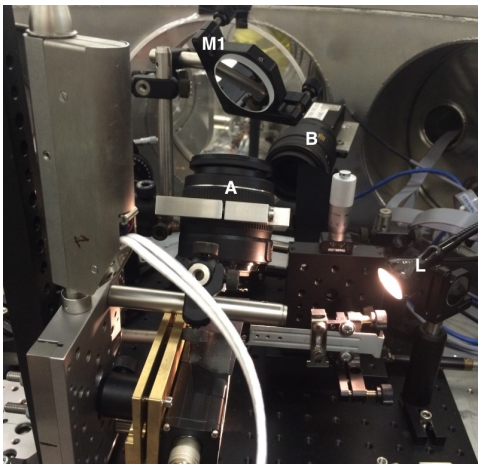

(c) Front view of the interaction point.

Figure 9.4. Real pictures of the experimental setup realized at FLAME target area for EOS measurements. **A**: CCD camera equipped with wide angle objective to look at the whole interaction point, both main on target and probe on EOS crystal; **B**: objective; **C**: CCD camera equipped with an objective used in combination with **B** to get a magnified image of the main laser on the target; **M1,M2**: mirrors sending the image outside the vacuum chamber; **L**: commercial led lamp, remotely controlled.

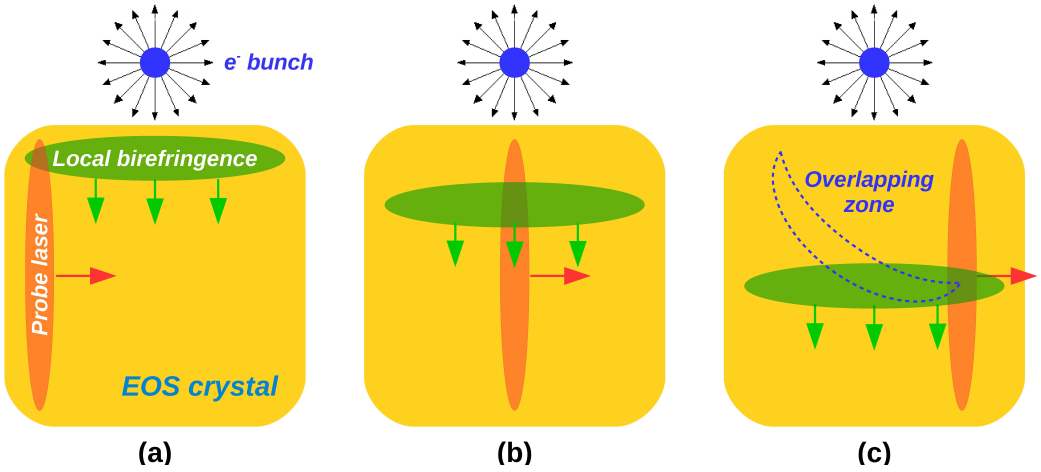

Figure 9.5. Working principle of the EOS diagnostics. (a) The electron bunch is moving normally to the figure and its Coulomb field induces a localized birefringence in the electro-optic crystal. (b) While the bunch electric field penetrates through the crystal, the birefringence locally moves downwards. Simultaneously the probe laser crosses sideways the crystal and its polarization is rotated according to the probed birefringence. (c) The resulting output signal is emitted by the blue region, where the local birefringence and the probe laser are temporally overlapped.

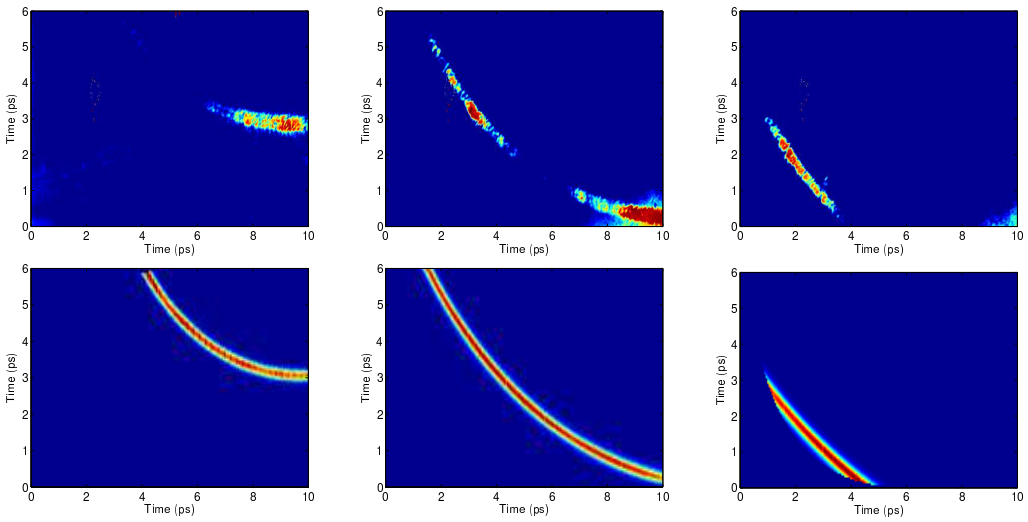

Figure 9.6. Snapshots with the wedge target. (a-c) Experimental measurements obtained by focusing the main laser on the edge of a wedged target at different probe laser delays (Δt). The electron bunch is moving above the upper side and perpendicularly to the crystal. By measuring its time of flight we found a mean energy of 15 MeV. The signal amplitude corresponds to 2.1 nC charge and the resulting bunch duration is 1 ps (rms). (d-f) Expected EOS signals assuming such bunch parameters. The lack of uniformity in the experimental signals, if compared with the simulated ones, is due to inhomogeneities in both the ZnTe crystal and probe laser spot.

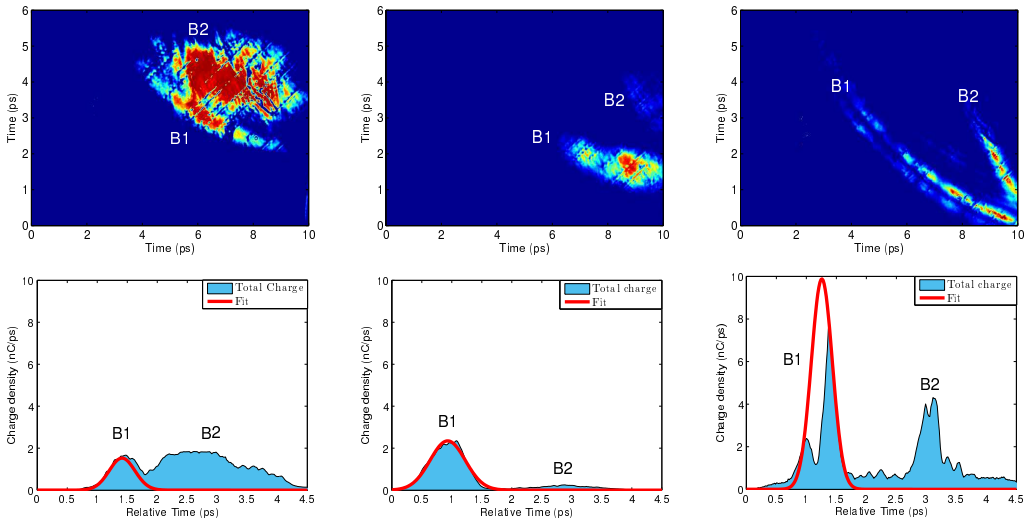

Figure 9.7. Snapshots with different target shapes. Signatures of the escaping electrons from (a) planar, (b) wedged and (c) tipped targets. The emitted charges are, respectively, (a) 1.2 nC (B1) and 3 nC (B2); (b) 2 nC (B1) and 0.3 nC (B2); (c) 7 nC (B1) and 3 nC (B2). The gaussian envelopes represent the extrapolated charge profiles of each bunch. (d-f) Corresponding longitudinal charge profiles. A 10^2 neutral density filter has been used in (b) and (c) in order to avoid saturation of the CCD camera.

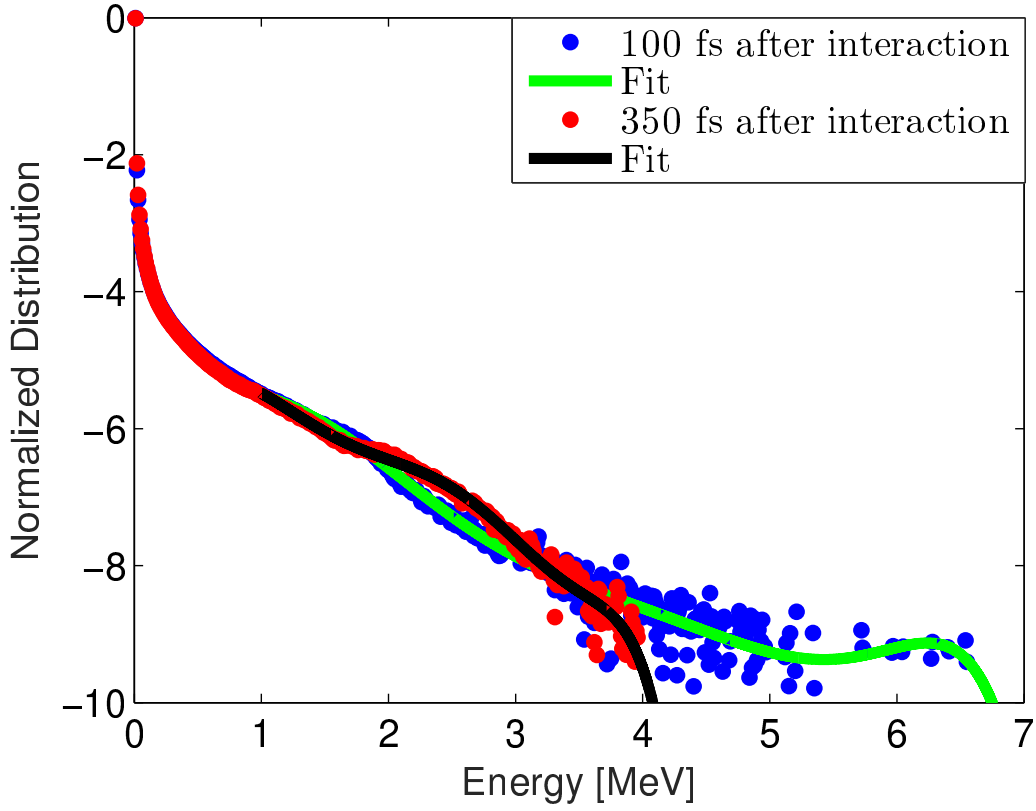

Figure 9.8. Energy spectrum of the emitted electrons The blue (red) points have been obtained 100 fs (350 fs) after the interaction with the laser. The solid lines represent the computed fit on such distributions. The y-axis is in logarithmic scale.

Part III

Conclusions and bibliography

Conclusions and perspectives

In this thesis the employee of high power lasers both in Thomson back-scattering and in laser wakefield acceleration has been studied. In detail, the results obtained at SPARC_LAB with the FLAME laser has been discussed.

Thomson source at SPARC_LAB has been started in 2013. As very first commissioning results X-rays were obtained with an average energy of $60keV$, 19% bandwidth FWHM and a flux equal to 6.7×10^3 photons per shot. Unfortunately, a problem related to the focusing solenoid cooling system has been detected and it caused a premature end of the experimental run. Moreover, a misalignment of the interaction chamber seemed to be the source of the low measured flux, about two orders of magnitude less than what theoretically expected. At the same time, also the electron beam dumping needed to be changed and located upstream the parabolic mirror vacuum chamber, in order to remove the high background signal due to electrons hitting the interaction chamber originating Bremsstrahlung photons.

In the second commissioning run, a $30MeV$ electron beam energy working point, delivering a maximum X-ray energy of $20keV$, has been addressed as foreseen for the first planned imaging experiment. With the available hardware (only phase shifters on the 3 S-band sections) the applied acceleration/deceleration scheme worked well enough to produce a low energy spread electron beam at $30MeV$, even though resulting in a strong sensitivity for the electron beam to the machine imperfections/stability. The measured flux was almost the same of the previous run ($\approx 10^4$) and was two orders of magnitude less than the theoretical one as well. This time has been possible to install a X-ray CCD and make an image of the interaction chamber exit window and a clear misalignment has been detected. Following the experimental results of the two runs, the optimization plan foresees a better control of the electron trajectory at the IP to avoid unrecoverable off-axis emission of the Thomson radiation and too high background contribution to the X-ray detectors signal. An interaction setup upgrade is also under study, coming to a non-zero angle collision in order to make it easier the electron and laser pulse trajectory control removing the on axis counter propagation that limit the room availability for both beams diagnostic.

The STAR project is in an advanced phase and first electron-photon collisions are foreseen within the end of 2017. The generated X-ray beam will be provided to the UNICAL user for tomography experiment, whose setup has been already installed in the STAR bunker. The installation of the remaining parts is still on going. The LINAC components (gun, S-band accelarating structure, quadrupoles and electron beam pipes) have been positioned and optically aligned with high precision by the mechanical division of LNF. In particular, the gun is ready to be

tested once its klystron will be commissioned by the providing company together with the INFN staff collaborating to this project. Concerning the laser systems, although the interaction laser delivery has been postponed by Amplitude Systemes because of issues in the production line, the system providing the pulses for the electron extraction from a copper cathode has been installed and commissioned. The transverse beam shaping of the photocathode laser will be provided by a flexible optical system (see Fig. 3.4, with a dedicated diagnostics line, as described previously. The optical design has been fixed, but its experimental realization has been stopped since the laser transport line has not been positioned yet as well as for the interaction laser. In the far future, a possible LINAC upgrade providing electrons up to $350Mev$ is under study, in order to explore a more wide range of X-ray region.

The preliminary results on LWFA at FLAME, although not yet optimized, are really promising. Indeed, in such a small accelerating cavity ($\approx 2.5mm$ corresponding to plasma channel length), we are able to reach high energy electron beams ($\approx 300MeV$) with a quite acceptable divergence of few mrad. Certainly, as future upgrade, it will be designed a beam transport line based on permanent quadrupoles in order to obtain a more collimated electron beam. On the other hand, a better optimization of acceleration scheme will be done. First of all, a study with gas-jet of different diameters, such that the dephasing length is approximately equal to the acceleration length, reducing the energy spread, will be done in the near future. On the other hand, also a different approach, based on the employee of gas-filled tubes (gas-cell or dielectric capillary) will be investigate. In particular, this latter should give more control on the gas parameters with respect to the gas-jet.

The optimization of LWFA process and a good quality for the accelerated electrons are crucial in order to test our new diagnostic tool concerning the measurement of electron beam emittance in a single shot way. Indeed, particular attention has to be given to the angular divergence that should be $1mrad$ at maximum with these energies. In this sense, the realization of a simple magnetic transport line will help. On the other side, the experimental setup as shown in Fig. 8.4 is already placed in the FLAME target area. At the same time, a new experimental run is foreseen at SPARC_LAB when the new klystron will be installed. In fact, it will allow to reach an electron energy, around $180MeV$, high enough to have a good angular resolution for the emittance measurement (see Fig. 8.3).

Despite the self-injection scheme allows to realize a linear accelerator in a really short length ($\approx 2mm$ in our case), the combination of a plasma channel, stimulated by an intense laser propagating in a gas medium, and a pre-existing high quality electron beam, coming with extremely low emittance and energy spread from an high brightness photo-injector like at SPARC_LAB, represents a really good compromise. Indeed, as discussed in Chapter 7, simulations for EXIN project show that, working in linear regime with lower accelerating gradients (around $30GV/m$) but longer acceleration lengths, it is possible to reach a final energy of $630MeV$ starting with an electron energy equals to $80MeV$. The key point of this scheme is that it allows to exploit the high accelerating gradients of plasma wakefield keeping the initial electron beam quality almost intact. In this sense, a study of laser propagation in a dielectric capillary has been conducted and some preliminary tests have been performed. However, it will be mandatory a dedicated experimental session regarding fundamental capillary mode coupling efficiency and laser propagation inside

a long capillary ($10cm$ as required for EXIN). On the other hand, the realization of experimental chamber and laser transport line is ongoing and the setup should be ready by the end of next year.

An other activity addressed to laser-plasma interaction has regarded the temporal profile measurement of the electric field carried by fast electrons coming out from the interaction on an intense laser with solid targets. Since this electrons are considered as the driver of ions and protons, the possibility to control their electric field seems to be crucial. By means of EOS technique, already used at SPARC_LAB for temporal measurements on electron bunches accelerated by the RF linac, it has been possible to obtain the longitudinal profile of this electric field. Moreover, using this tool also as time of flight diagnostics, it has been measured the electron charge as well, necessary to fit the electric field data. The crucial point that has been pointed out in this work concerns the field enhancement obtained by changing the target shape. Indeed, performing measurements on plane, wedge and tipped targets it has been shown the electric field carried by fast electrons was higher passing from one kind of target to another. With this experiment, it has been measured a significant increase in the charge and energy of the escaping electrons (corresponding to the increase in the potential barrier) for sharp structured targets. These results demonstrate the field enhancement conjecture previously predicted and can be used as a guideline in order to achieve higher energies for positively charged ions with respect to what is currently obtained through conventional laser acceleration schemes, mainly aiming to more and more powerful laser systems.

In the next future, a new experiment is under design. The geometry of the EOS diagnostics will be changed in order to have the electric field lines perpendicular to the EO crystal. In this way, the expected signal will be cleaner than the previous one. Moreover, also a magnetic spectrometer will be installed to measure directly the electron energy.

Bibliography

[1] D. Attwood, *Soft X-rays and Extreme Ultraviolet Radiation: Principles and Applications*, Cambridge University Press, Cambridge, (1999).

[2] D. Attwood, K. Halbach, and K. Kim, Science **228**, 1265, (1985).

[3] R. W. Schoenlein, H. H. W. Chong, T. E. Glover, P. A. Heimann, W. P. Leemans, H. A. Padmore, C. V. Shank, A. A. Zholents, M. S. Zolotorev, and J. S. Corlett, Acad. Sci. Paris **IV**, 1378, (2001).

[4] R. W. Schoenlein, W. P. Leemans, A. H. Chin, P. Volfbeyn, T. E. Glover, P. Balling, M. Zolotorev, K.-J. Kim, S. Chattopadhyay, and C. V. Shank, Science **274**, 236, (1996).

[5] F. Arutyunyan and V. Tumanyan, Sov. J. Exp. Theor. Phys. **17**, 1417, (1963).

[6] F. Arutyunyan and V. Tumanyan, Physics-Uspekhi **339**, (1964).

[7] R. Milburn, Phys. Rev. Lett. **10**, 1, (1963).

[8] O. Kulikov, Y. Telnov, E. Filippov, and M. Yakimenko, Phys. Lett. **13** 344, (1964).

[9] P. Sprangle, A. Ting, E. Esarey, and A. Fisher, J. Appl. Phys. **72**, 5032 (1992).

[10] E. Esarey, S. K. Ride, and P. Sprangle, Phys. Rev. E **48** (1993).

[11] H. Ohgaki, T. Noguchi, and S. Sugiyama, Nucl. Instruments Methods Phys. Res. Sect. A Accel. Spectrometers, Detect. Assoc. Equip. **353**, 384 (1994).

[12] A. Ting, R. Fischer, A. Fisher, K. Evans, R. Burris, J. Krall, E. Esarey, and P. Sprangle, J. Appl. Phys. **78**, 575 (1995).

[13] R. Schoenlein, W. Leemans, A. H. Chin, P. Volfbeyn, T. Glover, P. Balling, M. Zolotorev, K.-J. Kim, S. Chattopadhyay, and C. Shank, Science (80-.). **274**, 236 (1996).

[14] W. Leemans, R. Schoenlein, P. Volfbeyn, A. Chin, T. Glover, P. Balling, M. Zolotorev, K. Kim, S. Chattopadhyay, and C. Shank, Phys. Rev. Lett. **77**, 4182 (1996).

[15] F. Carroll, J. Waters, R. Traeger, M. Mendenhall, W. Clark, and C. Brau, SPIE Conf. Free. Laser Challenges II **3614**, 139 (1999).

[16] I. Pogorelsky, I. Ben-Zvi, X. Wang, and T. Hirose, Nucl. Instruments Methods Phys. Res. Sect. A Accel. Spectrometers, Detect. Assoc. Equip. **455**, 176 (2000).

[17] N. Pietralla, Z. Berant, V. Litvinenko, S. Hartman, F. Mikhailov, I. Pinayev, G. Swift, M. Ahmed, J. Kelley, S. Nelson, R. Prior, K. Sabourov, A. Tonchev, and H. Weller, Phys. Rev. Lett. **88**, 012502 (2001).

[18] P. Catravas, E. Esarey, and W. Leemans, Meas. Sci. Technol. **1828** (2001).

[19] T. Nakano et al. , Phys. Rev. Lett. **91**, 012002 (2003).

[20] V. G. Nedorezov, A. A. Turinge, and Y. M. Shatunov, Physics-Uspekhi **47**, 341 (2004).

[21] W. P. Leemans, E. Esarey, J. van Tilborg, P. A. Michel, C. B. Schroeder, C. Toth, C. G. Geddes, and B. A. Shadwick, IEEE Trans. Plasma Sci. **33**, 8 (2005).

[22] V. G. Nedorezov, Phys. Part. Nucl. **43**, 326 (2012).

[23] K. Achterhold, M. Bech, S. Schleede, G. Potdevin, R. Ruth, R. Loewen, and F. Pfeiffer, Sci. Rep. **3**, 1313 (2013).

[24] S.G. Rykovanov et al., arxiv:1406.1832v1, (2014).

[25] W. B. Colson, "Free Electron Laser Theory", Ph.D. Thesis, Stanford University, 1977.

[26] S. K. Ride and W. B. Colson, Stanford University High Energy Physics Lab Report 858 (1979).

[27] W. B. Colson, IEEE J. Quantum Electron **QE-17**, 1417 (1981).

[28] W. B. Colson, G. Dattoli and F. Ciocci, Phys. Rev. A **31**, 828 (1985).

[29] R. Barbini, F. Ciocci, G. Dattoli and L. Giannessi, Nuovo Cimento **13**, 1 (1990).

[30] R. Hajima, N. Kikuzawa, N. Nishimori, T. Hayakawa, T. Shizuma, K. Kawase, M. Kando, E. Minehara, H. Toyokawa, and H. Ohgaki, Nucl. Instruments Methods Phys. Res. Sect. A Accel. Spectrometers, Detect. Assoc. Equip. **608**, S57 (2009).

[31] E. Esarey, C. Schroeder, and W. Leemans, Rev. Mod. Phys. **81**, 1229 (2009).

[32] W. P. Leemans, B. Nagler, A. J. Gonsalves, C. Toth, K. Nakamura, C. G. R. Geddes, E. Esarey, C. B. Schroeder, and S. M. Hooker, Nat. Phys. **2**, 696 (2006).

[33] P. Schmueser, M. Dohlus, and J. Rossbach, Ultraviolet and Soft X-Ray Free-Electron Lasers: Introduction to Physical Principles, Experimental Results, Technological Challenges (Springer Tracts in Modern Physics) (Springer, 2008).

[34] E. Sarachik and G. Schappert, Phys. Rev. D **1** (1970).

[35] V. Litvinenko and J. Madey, Nucl. Instruments Methods Phys. Res. Sect. A Accel. Spectrometers, Detect. Assoc. Equip. **375**, 580 (1996).

[36] V. Berestetskii, E. Lifshitz and L. Pitaevskii, Quantum Electrodynamics. Landau and Lifshitz, Course of Theoretical Physics, Vol. 4, Pergamon Press (1982)

[37] K. Yokoya, http://www-acc-theory.kek.jp/members/cainS (1985)

[38] K. Yokoya, User manual of CAIN, version 2.40, http://lcdev.kek.jp/yokoya/CAIN/Cain242/CainMan242.pdf (2009)

[39] O.KleinandY.Nishina,Uber die Streuung von Strahlung durch freie Elektronen nach der neuen relativistischen Quantendynamik von Dirac, Z. Phys. 52 (1929) 11-12

[40] C. Curatolo, *"High brilliance photon pulses interacting with relativistic electron and proton beams"*, PhD Thesis (2016).

[41] R. Malvano et al., *Some considerations on the possibility of obtaining a quasi-monochromatic polarized photon beam from Laser-electron scattering in the storage ring Adone.*, LNF-67/48, (1967).

[42] D. Babusci et al., *Polarised and tagged gamma-ray Ladon beams*, LNF-95/058, (1995).

[43] L. Federici, et al., Nuovo Cimento **B 59**, 47, (1980).

[44] L. Casano et al., Laser and Unconventional Optics Journal **55**, 3, (1975).

[45] G. Matone et al., Lecture Notes in Physics 62, 149, (1977): Photonuclear Reactions II, S.Costa and C.Schaerf eds. Springer-Verlag, Berlin. Invited contribution to the Europhysics Study Conf. on High Energy Laser and Scientific Applications, Oxford (1975).

[46] A. M. Sandorfi, et al., IEEE Trans. Nucl. Sci. **NS-30**, 3083, (1983).

[47] T. Russew, PhD Dissertation Grenoble University, (1995).

[48] M. Ferrario et al., Nucl. Instruments Methods Phys. Res. Sect. B: Beam Interactions with Materials and Atoms **309**,183–188, (2013).

[49] M. Ferrario et al., Proceedings of IPAC'10, Kyoto, Japan.

[50] A. Giribono, Il Nuovo Cimento **38 C**, 83, (2015).

[51] P. Oliva et al., Nucl. Instr. Meth. A **615** (2010) 93–99.

[52] A. Bacci et al., Nucl. Instr. Meth. A 608 (2009) S90–S93.

[53] U. Bottigli et al., Il Nuovo Cimento 29C (N.2) (2006).

[54] L. Giannessi et al., Phys. Rev. Lett. **106** (2011) 144801.

[55] M. Labat et al., Phys. Rev. Lett. **107** (2011) 224801.

[56] L. Giannessi et al., Phys. Rev. Lett. 108 (2012) 164801.

[57] E. Chiadroni et al., J. Phys: Conf. Ser. 357 (2012) 012034.

[58] L.A. Gizzi et al., Europ. Phys. J. – Special Topics 175 (2009) 3.

[59] M. Ferrario et al., Nucl. Instr. Meth. A 637 (1) (May 2011) S43–S46.

[60] R. Pompili, *"Longitudinal diagnostics for comb-like electron beams by means of Electro-Optic Sampling"*, PhD Thesis, (2013).

[61] A. Mostacci, M. Bellaveglia et al., Phys. Rev. ST Accel. Beams, 15:082802, (2012).

[62] D.Filippetto,M.Bellaveglia et al., Phys. Rev. ST Accel. Beams, 14:092804, (2011).

[63] A. Cianchi, D. Alesini et al., Phys. Rev. ST Accel. Beams, 11:032801, (2008).

[64] Martin Reiser. Theory and design of charged particle beams. John Wiley & Sons, (2008).

[65] M. Ferrario et al. Slac-pub-8400, (2000).

[66] D. Strickland and G. Mourou, Optics Communications **56**, 3, 219-221, (1985).

[67] C. Vaccarezza et al., Proceedings of IPAC2014, Dresden, Germany.

[68] Petrillo V. et al., Nucl. Instrum. Methods Phys. Res. A **693**, 109 (2012).

[69] C. Vaccarezza et al., Nucl. Instruments Methods Phys. Res. Sect. A Accel. Spectrometers, Detect. Assoc. Equip. **829**, (2016).

[70] P. Cardarelli, et al., Journal of Applied Physics **112** (074908).

[71] B. Golosio, et al., Applied Physics Letters **100** (164104).

[72] A. Bacci, et al., Journal of Applied Physics **113** (194508).

[73] A.Bacci et al., Proceedings of IPAC'14, Dresden, Germany.

[74] A.Bacci et al., Proceedings of IPAC'16, Busan, Korea.

[75] A. D'Alessandro, et al., Geophysical Research Abstracts **16**, EGU2014-15672, 2014, EGU General Assembly, (2014).

[76] L. Serafini, J.B. Rosenzweig . PRE **55**, 6, (1997).

[77] M. Ferrario et al., PRL **99**, 234801(2007).

[78] M. Ferrario et al.,PRL **104**, 054801(2010).

[79] F. Zhou et al., Phys. Rev. STAB **15**, 090701 (2012)

[80] P.Chen et al., Nucl. Instr. Meth. A **355** (1995) 107.

[81] B. Keil, et al., proceedings of IBIC2013, TUPC25, Oxford,UK.

[82] M. Svandrlik, et al., proceeding of IPAC2014, HPRO013, Dresden, Germany.

[83] J. M. Dawson, Phys. Rev., **133**, 383-387, (1959).

[84] A. I. Akhiezer and R. V. Polovin, Zh. Eksp. Teor. Fiz., **30**, 915-928, (1956); Sov. Phys. JETP , **3**, 696-705, (1956).

[85] T. Tajima and J. M. Dawson, Phys. Rev. Lett. **43**,4, (1979).

[86] T. Katsouleas and J. M. Dawson, Physical Review Letters, **51**:392-395, (1983).

[87] C. Joshi, W. B. Mori, et al., Nature,**311**:525-529, (1984).

[88] P. Chen, J. M. Dawson, et al., Phys. Rev. Lett., **54**:693-696,(1985).

[89] P. Chen et al., Phys. Rev. Lett., **56**, (1986).

[90] A.R. Rossi et al., Physics Procedia, **52**, 90 - 99, (2014)

[91] P. Gibbon, Proceedings of the CAS-CERN Accelerator School: Plasma Wake Acceleration, Geneva, Switzerland, 23–29 November 2014, (2016).

[92] B. Cros, Proceedings of the CAS-CERN Accelerator School: Plasma Wake Acceleration, Geneva, Switzerland, 23–29 November 2014, (2016).

[93] J. Vieira et al., Proceedings of the CAS-CERN Accelerator School: Plasma Wake Acceleration, Geneva, Switzerland, 23–29 November 2014, (2016).

[94] B. Bingham and R. Trines, Proceedings of the CAS-CERN Accelerator School: Plasma Wake Acceleration, Geneva, Switzerland, 23–29 November 2014, (2016).

[95] C. Aniculaesei, Ph.D. thesis, Strathclyde University

[96] M.P. Anania, *"Towards a free-electron laser driven by a laser wakefield accelerator"*, PhD Thesis, (2014).

[97] B.W. Miller, H. Bradford Barber, H.H. Barrett, D.W. Wilson, L. Chen, Nuclear Science Symposium Conference Record, **6**, 3540, (2006).

[98] M. William Yen, S. Shionoya, H. Yamamoto, "Practical Applications of Phosphors", CRC Press, (2006).

[99] A. Kuthy, Nuclear Instruments and Methods **180**, 1, (1981).

[100] F. Ingenito, Journal of Instrumentation, **11**, (2016).

[101] http://www.ape-berlin.de/

[102] F. Filippi, "Plasma source characterization for plasma-based acceleration experiments", PhD thesis.

[103] M. Migliorati et al., Phys. Rev. Spec. Top. Acc. Beams **16**, 011302 (2013).

[104] B. Cros et al., Phys. Rev. E **65**(2) (2002).

[105] F.G. Bisesto et al., Nucl. Instrum. Methods Phys. Res. A **829**, 309-313 (2016).

[106] A.R. Rossi et al., Nucl. Instrum. Methods Phys. Res. A **829**, 67-72 (2016).

[107] S. S. Harilal and M. S. Tillack, UCSD-ENG-114

[108] Minty, Michiko G and Zimmermann, Frank, Springer Science & Business Media, (2003).

[109] A. Mostacci et al., Physical Review Special Topics-Accelerators and Beams, **15**, 8, (2012).

[110] A. Cianchi et al., Nucl. Instrum. Methods Phys. Res. A **829**, (2016).

[111] M. L. Ter-Mikaelian, High energy electromagnetic processes in condensed media.

[112] V. Verzilov, *Private communication*, 1997

[113] C. Couillaud, A. Loulergue, G. Haouat, Elecron beam transverse emittance measurement using optical transition radiation interferometry, in: this Conference, 1996.

[114] R. Feldman, A. Lumpkin, D. Rule, R. Fiorito, Nuclear Instruments and Methods in Physics Research Section A: Accelerators, Spectrometers, Detectors and Associated Equipment **296** (1),193–198, (1990) .

[115] L. Wartski et al., Journal of Applied Physics **46** (8), 3644–3653, (1975).

[116] G. Le Sage et al., Physical Review Special Topics-Accelerators and Beams **2** (12), 122802, (1999).

[117] F.G. Bisesto et al., *in preparation*

[118] "Zemax 13, Optical Design Program, Users Manual", January 24, 2014.

[119] T. Aumeyr, M. G. Billing, L. M. Bobb, B. Bolzon, E. Bravin, P. Karataev, K. Kruchinin, T. Lefevre, and S. Mazzoni Phys.Rev.STAB, **18** 042801, (2015).

[120] Chiadroni, E and Castellano, M and Cianchi, A and Honkavaara, K and Kube, G, Nuclear Instruments and Methods in Physics Research Section A: Accelerators, Spectrometers, Detectors and Associated Equipment, **673**, 56–63, (2012).

[121] M.Castellano, A.Cianchi, G.Orlandi, V.A.Verzilov, NIM A, **435** (1999)

[122] Bruce A. Remington et al., Science, **284**, 5419, (1999).

[123] M. Roth et al., Physical Review Letters, **86**, 3, (2001).

[124] T. Bartal et al., Nat. Phys., **8**, 2, (2012).

[125] KWD Ledingham et al., New Journal of Physics, **12**, 4, (2010).

[126] EL Clark et al., Physical Review Letters, **85**, 8, (2000).

[127] RA Snavely et al., Physical Review Letters, **85**, 14, (2000).

[128] AJ Mackinnon et al., Physical review letters, **88**, 21, (2002).

[129] Ken WD Ledingham et al., Applied Sciences, **4**, 3, (2014).

[130] F. Abicht, "Ultrafast Field Dynamics in Laser Ion Acceleration", PhD Thesis, (2015).

[131] Prashant Kumar Singh et al., Physics of Plasmas (1994-present), **20**, 11, (2013).

[132] A.Poyé,S.Hulin,M.Bailly-Grandvaux,J.-L.Dubois,J.Ribolzi,D.Raffestin,M.Bardon,F.Lubrano-Lavaderci, E. D'Humières, J. J. Santos et al., Physical Review E **91**, 043106 (2015).

[133] AG Krygier et al., Physics of Plasmas (1994-present), **21**, 2, (2014).

[134] A. Macchi et al., Reviews of Modern Physics, **85**, 2, (2013).

[135] J.-L.Dubois,F.Lubrano-Lavaderci,D.Raffestin,J.Ribolzi,J.Gazave,A.C.LaFontaine,E.d'Humières,S.Hulin et al.,Physical Review E **89**,013102(2014).

[136] J. Badziak, S. G lowacz, S. Jablonski, P. Parys, J. Wolowski, H. Hora, J. Kràsa, L. Làska, and K. Rohlena, Plasma Physics and Controlled Fusion **46**, B541 (2004).

[137] A.Poyé,J.-L.Dubois,F.Lubrano-Lavaderci,E.D'Humières,M.Bardon,S.Hulin,M.Bailly-Grandvaux,J.Ribolzi, D. Raffestin, J. Santos, et al., Physical Review E **92**, 043107 (2015).

[138] L. Robson, P. Simpson, R. J. Clarke, K. W. Ledingham, F. Lindau, O. Lundh, T. McCanny, P. Mora, D. Neely, C.-G. Wahlstrom, et al., Nature physics **3**, 58 (2007).

[139] O. Jackel, J. Polz, S. Pfotenhauer, H. Schlenvoigt, H. Schwoerer, and M. Kaluza, New Journal of Physics **12**, 103027 (2010).

[140] P. Nilson, J. Davies, W. Theobald, P. Jaanimagi, C. Mileham, R. Jungquist, C. Stoeckl, I. Begishev, A. Solodov, J. Myatt, et al., Physical Review Letters **108**, 085002 (2012).

[141] A. Sandhu, A. Dharmadhikari, P. Rajeev, G. R. Kumar, S. Sengupta, A. Das, and P. Kaw, Physical Review Letters **89**, 225002 (2002).

[142] R. Pompili, M.P. Anania, F. Bisesto, M. Botton, M. Castellano, E. Chiadroni, A. Cianchi, A. Curcio, M. Ferrario, M. Galletti, Z.Henis, M. Petrarca, E. Schleifer, and A. Zigler, Nature Scientific Reports 6:35000, (2016).

[143] I. Wilke, A. M. MacLeod, W. Gillespie, G. Berden, G. Knippels, and A. Van Der Meer, Physical Review Letters **88**, 124801 (2002).

[144] A. Zigler, S. Eisenman, M. Botton, E. Nahum, E. Schleifer, A. Baspaly, I. Pomerantz, F. Abicht, J. Branzel, G. Priebe, et al., Physical Review Letters **110**, 215004 (2013).

[145] A. Zigler, T. Palchan, N. Bruner, E. Schleifer, S. Eisenmann, M. Botton, Z. Henis, S. Pikuz, A. Faenov Jr, D. Gordon, et al., Physical Review Letters **106**, 134801 (2011).

[146] D. Margarone, O. Klimo, I. Kim, J. Prokupek, J. Limpouch, T. Jeong, T. Mocek, J. Psikal, H. Kim, J. Proska, et al., Physical Review Letters **109**, 234801 (2012).

[147] R. Pompili, A. Cianchi, D. Alesini, M. Anania, A. Bacci, M. Bellaveglia, M. Castellano, E. Chiadroni, D. Di Giovenale, G. Di Pirro, et al., Nuclear Instruments and Methods in Physics Research Section A: Accelerators, Spectrometers, Detectors and Associated Equipment, **740**, (2014).

[148] A. L. Cavalieri, D. Fritz, S. Lee, P. Bucksbaum, D. Reis, J. Rudati, D. Mills, P. Fuoss, G. Stephenson, C. Kao, et al., Physical Review Letters **94**, 114801 (2005).

[149] D. F. Gordon, W. Mori, and T. M. Antonsen Jr, Plasma Science, IEEE Transactions on plasma science **28**, 1135 (2000).